UNIVERSIDADE FEDERAL DE SANTA CATARINA
PROGRAMA DE PÓS-GRADUAÇÃO EM ENGENHARIA MECÂNICA

Eduardo Lucas Konrad Burin

PLANTAS DE COGERAÇÃO DO SETOR SUCROALCOOLEIRO ASSISTIDAS POR CONCENTRADORES PARABÓLICOS

Florianópolis

2015

UNIVERSIDADE FEDERAL DE SANTA CATARINA
PROGRAMA DE PÓS-GRADUAÇÃO EM ENGENHARIA MECÂNICA

Eduardo Lucas Konrad Burin

PLANTAS DE COGERAÇÃO DO SETOR SUCROALCOOLEIRO ASSISTIDAS POR CONCENTRADORES PARABÓLICOS

Tese submetida ao Programa de Pós-Graduação em Engenharia Mecânica da Universidade Federal de Santa Catarina para a obtenção do grau de Doutor em Engenharia Mecânica.
Orientador: Prof. Dr. Edson Bazzo

Florianópolis

2015

Ficha de identificação da obra elaborada pelo autor,
através do Programa de Geração Automática da Biblioteca Universitária da UFSC.

Burin, Eduardo Lucas Konrad
Plantas de cogeração do setor sucroalcooleiro assistidas por concentradores parabólicos / Eduardo Lucas Konrad Burin ; orientador, Edson Bazzo - Florianópolis, SC, 2015.
157 p.

Tese (doutorado) - Universidade Federal de Santa Catarina, Centro Tecnológico. Programa de Pós-Graduação em Engenharia Mecânica.

Inclui referências

1. Engenharia Mecânica. 2. Bagaço de cana. 3. Cogeração. 4. Energia termossolar. 5. Hibridização. I. Bazzo, Edson. II. Universidade Federal de Santa Catarina. Programa de Pós-Graduação em Engenharia Mecânica. III. Título.

Eduardo Lucas Konrad Burin

PLANTAS DE COGERAÇÃO DO SETOR SUCROALCOOLEIRO ASSISTIDAS POR CONCENTRADORES PARABÓLICOS

Esta Tese foi julgada adequada para obtenção do Título de Doutor em Engenharia Mecânica e aprovada em sua forma final pelo Programa de Pós-Graduação em Engenharia Mecânica da Universidade Federal de Santa Catarina.
Florianópolis, 31/07/2015.

_____

Armando Albertazzi Gonçalves Jr., Dr.
Coordenador do Curso

Banca Examinadora:

_____

Edson Bazzo, Dr., Orientador

_____

Silvia Azucena Nebra de Pérez, Dra.

_____

Paulo Smith Schneider, Dr.

_____

Rogério Gomes de Oliveira, Dr.

_____

Samuel Luna de Abreu, Dr.

_____

Leonel Rincón Cancino, Dr.

Aos meus avós, Narciso e Amélia Burin, Ivo e Iloina Konrad.

Aos meus pais, Neivaldo e Mirian.

A vida é curta,
a arte é longa,
a oportunidade é fugaz,
a experiência enganosa,
o julgamento difícil.

Hipócrates

AGRADECIMENTOS

Ao professor Edson Bazzo, meu orientador, pela amizade, orientação e incentivo. Agradeço pela confiança depositada em mim durante esta etapa.

À minha mãe, Mirian, ao meu pai, Neivaldo e à minha irmã, Raquel, pelo carinho, dedicação, educação e apoio em cada passo da minha vida.

A toda minha família, pelo apoio ao meu projeto de vida.

À Glaucia Medeiros, pelo carinho, atenção, amizade e incentivo.

Ao Laboratório de Combustão e Engenharia de Sistemas Térmicos (LabCET) da Universidade Federal de Santa Catarina (UFSC) pela oportunidade e apoio fundamental em relação ao desenvolvimento desse trabalho e à minha formação.

Ao Programa de Pós-Graduação em Engenharia Mecânica (PósMEC) da UFSC, bem como a todos os professores, pela minha formação.

Aos todos os amigos do LabCET, em especial aos professores Edson Bazzo e Amir Oliveira, bem como aos colegas Amir De Toni, Raphael Miyake, Alvaro Restrepo, Fabio Kleveston, Renzo Figueroa, Nury Garzon, Marcos Oro, Marco Antônio, Rafael Zotto, Eduardo Hartmann, Ricardo Hartmann, Alexandre Schimidt, Leandro Alves e Julian Barrera pela amizade e momentos compartilhados.

Ao LUAT da Universidade de Duisburg-Essen pelo período de doutorado sanduíche. Agradeço ao professor Klaus Goerner, ao Dr. Oeljeklaus, à Sra. Hoffmann e aos colegas Tobias Vogel, Andre Thelen e Sven Multhaupt pela amizade, atenção e contribuição técnica.

Ao engenheiro Rodrigo Luis Mello Fonseca pela amizade desde a graduação e pelo importante auxílio técnico prestado durante o desenvolvimento deste trabalho. Agradeço também por me apresentar o setor sucroalcooleiro, o que foi de fundamental importância.

À TGM turbinas, em especial aos engenheiros Leonardo Buranello e Pedro Lo Giudice, bem como à Caldema, em especial ao engenheiro Afrânio Lopes, pelas contribuições técnicas.

Ao CNPq pelo auxílio por meio da linha de financiamento de bolsas de doutorado. À CAPES pelo financiamento da minha estadia na Alemanha em estágio de doutorado sanduíche. À CAPES, ao DAAD e ao GIZ pela viabilização do projeto iNOPA desenvolvido em parceria com a Universidade de Duisburg-Essen.

A todas as pessoas que contribuíram para o desenvolvimento desse trabalho.

RESUMO

Um importante aspecto relacionado à geração de energia elétrica por meio do uso de biomassa consiste na garantia da qualidade e da disponibilidade do combustível ao longo do ano. No setor sucroalcooleiro, como exemplo, bagaço encontra-se disponível principalmente durante o período da safra que na região Centro-Sul do Brasil acontece entre os meses de Abril e Dezembro. Nesse contexto, o objetivo deste trabalho consiste em avaliar a viabilidade técnica e econômica da integração de concentradores parabólicos com os ciclos de cogeração do setor sucroalcooleiro como forma de estender a operação destas plantas para o período da entressafra. O potencial foi previamente identificado em função do grande número de plantas de cogeração em região em que a incidência de irradiação direta normal é adequada para a geração termossolar. Em relação à abordagem adotada, o primeiro passo consistiu na definição de uma planta de cogeração base com leiaute e características operacionais identificadas em conjunto com fabricantes de equipamentos do setor sucroalcooleiro. A planta é equipada com dois geradores de vapor com capacidade de 170 t/h de vapor superaquecido com parâmetros de 67 bar e 525 ^{o}C. O vapor superaquecido é expandido paralelamente em duas turbinas, sendo uma de contrapressão (BPST) e outra de condensação (CEST). A moagem anual da usina é de três milhões de toneladas de cana por safra. Dois leiautes de integração foram propostos e avaliados, sendo: (a) aquecimento de água de alimentação com energia solar e (b) geração de vapor saturado com energia solar para posterior superaquecimento em gerador de vapor a biomassa. Como resultados importantes, foram identificadas as características da operação dos principais componentes da planta de cogeração em condição fora do ponto de projeto. Foi identificado o potencial de economia de bagaço para ambos os casos, bem como o custo nivelado da eletricidade gerada (LCOE) em função da operação híbrida.

Palavras-chave: Cana-de-açúcar, bagaço, cogeração, energia termossolar, concentradores parabólicos.

ABSTRACT

One important problem related to the biomass power plants operation consists on the fuel availability along the year. This is also true for the sugarcane bagasse power plants in Brazil that are operated mainly during the sugarcane harvest period that ranges from April to December in the Center-South region. In this regard, the objective of this work was to evaluate the technical and economic feasibility of integrating Concentrated Solar Power (CSP) with the conventional sugarcane bagasse cogeneration power plants in the sugarcane sector in Brazil in order to extend their operation to the off-season period and, as a consequence, to improve the electricity production. The potential for CSP hybridization with bagasse was identified once both energy sources matches regionally in their availability. Regarding the adopted approach, the first step consisted on the identification of a base case sugarcane bagasse cogeneration power plant, whereby layout and operational parameters were defined in cooperation with equipment suppliers. The cogeneration cycle has two 170 t/h capacity steam generators that provide steam at 67 bar and 525 ^{o}C. Main steam is expanded in parallel in a backpressure (BPST) and a condensing-extraction (CEST) steam turbine. Three million tons of sugarcane are processed per harvest. Two integration layouts of parabolic trough concentrators into cogeneration cycle were evaluated, namely: (a) solar feedwater heating; (b) saturated steam generation with solar energy and post superheating in biomass steam generators. As main results, the off-design operation of solar aided plant concepts was here identified considering minimal modifications on the existing infrastructure. The bagasse economy potential due to hybridization as well as the Levelized Cost of Electricity (LCOE) of additional electricity produced was identified and compared with the current commercial CSP plants.

Keywords: Sugarcane, bagasse, cogeneration, concentrated solar power, parabolic trough.

LIST OF FIGURES

LIST OF TABLES

LIST OF ABBREVIATIONS

BPST	Back-Pressure Steam Turbines
CAPES	Coordination for the Improvement of Higher Education Personnel
CAPEX	Capital Expenditures
CEST	Condensing-Extraction Steam Turbines
CF	Capacity Factor
CSP	Concentrated Solar Power
CT	Central Tower
DAAD	German Academic Exchange Service
DB	Dry Bulb
DMS	Direct Molten Salts
DNI	Direct Normal Irradiation
DSG	Direct Steam Generation
EES	Engineering Equation Solver®
HCE	Heat Collection Element
HHV	Higher Heat Value
HSG	Hybridized Steam Generators
HTF	Heat Transfer Fluid
IAM	Incidence Angle Modifier
iNOPA	New Partnerships Program
ISCC	Integrated Solar Combined Cycles
LabCET	Laboratory of Combustion and Thermal Systems Engineering
LCOE	Levelized Cost of Electricity
LF	Linear Fresnel
LHV	Lower Heat Value
LUAT	Chair of Environmental Process Engineering and Plant Design
MENA	Middle East and North Africa
NREL	National Renewable Energy Laboratory
PE1	Puerto Errado One
PT	Parabolic Trough
PV	Photovoltaics
SAFWH	Solar Aided Feedwater Heating
SAM	System Advisor Model
SCA	Solar Collector Assembly
SEGS	Solar Energy Generating Systems
SGT	Solar-Gas Turbines
SM	Solar Multiple

TMY	Typical Meteorological Year
UFSC	Federal University of Santa Catarina
WB	Wet Bulb

LIST OF SYMBOLS

A	Area	[m²]
AE	Additional electricity generated	[MWh]
A_{ij}	Interaction parameter of gas-mixture conductivity	[-]
ae	Air excess	[%]
C	Carbon mass fraction	[kg/kg]
CC	Capital cost	[U$]
c	Mass fraction	[kg/kg]
cp	Specific heat at constant pressure	[kJ/kg.K]
d	Spacing between rows; Diameter	[m; mm]
$\dot{E}$	Energy transfer rate	[kW]
EB	Economized Bagasse	[t]
ET	Equation of time	[min]
e	Energy transfer per kilogram of burned fuel	[kJ/kg]
f	Degradation factor	[-]
fl	Average focal length	[m]
G_{bn}	Direct normal irradiance	[W/m²]
H	Hydrogen mass fraction	[kg/kg]
h	Enthalpy	[kJ/kg]
h_{conv}	Convection heat transfer coefficient	[kW/m².K]
h_{rad}	Radiation heat transfer coefficient	[kW/m².K]
k	Thermal conductivity	[W/m.K]
$k_{\Delta p}$	Pressure drop constant	[bar.s²/m²]
L	Length	[m]
LC	Land cost	[U$]
lt	Life time	[years]
M	Mass	[kg]
m	Mass flow per kilogram of burned fual	[kg/kg]
$\dot{m}$	Mass flow rate	[kg/s]
N	Nitrogen mass fraction	[kg/kg]
Nu	Nusselt number	[-]
n	Day of the year	[-]
O	Oxygen mass fraction	[kg/kg]
$O\&M$	Operation and maintenance cost	[U$]
Pr	Prandtl number	[-]
p	Pressure	[bar]
$\dot{Q}$	Heat transfer rate	[W]
$\dot{Q}'$	Heat transfer rate per unit length	[W/m]
$\dot{Q}''$	Heat flux	[W/m²]
q_{pro}	Heat demand per ton of processed sugarcane	[kWh/t]
R	Mass of residue per kilogram of burned fuel	[kg/kg]
R_{cond}	Thermal resistance for conduction	[K/kW]

Re	Reynolds number	[-]
r	Interest rate	[%]
S	Sulfur mass fraction	[kg/kg]
s	Spacing of tubes	[mm]
t	Time; Thickness	[h; mm]
t_f	Thickness of flame	[m]
UA	Overall heat transfer coefficient-area product	[kW/K]
V	Velocity	[m/s]
$\dot{V}$	Volume flow rate	[m³/s]
v	Volume flow per kilogram of burned fuel	[Nm³/kg]
$\dot{W}$	Rate at which work is performed	[W]
w	Width	[m]
w_{pro}	Electricity demand per ton of processed sugarcane	[kWh/t]
x	Quality	[-]
y	Mole fraction	[kmol/kmol]

Greek letters

α	Absorptivity; Ash collection point	[-]
α_s	Solar altitude angle	[rad]
δ	Declination angle	[rad]
ε_∞	Emissivity of a very tick flame	[-]
ε_{fs}	Effective emissivity between flame and surface	[-]
η	Efficiency	[%]
θ	Incidence angle	[rad]
θ_z	Zenith angle	[rad]
μ	Dynamic viscosity	[Pa.s]
ν	Kinematic viscosity	[m²/s]
ρ	Reflectivity; Mass density	[-; kg/m³]
τ	Transmissivity	[-]
ϕ	Latitude angle	[deg]
ϕ_{ij}	Interaction parameter of gas-mixture viscosity	[-]
χ	Longitude angle	[deg]
ψ	Azimuth angle	[rad]
ω	Time angle	[rad]
ω_{air}	Air humidity ratio	[kg/kg]

Subscripts and superscripts

abs	Absorbed
ad	Adiabatic
add	Additional
amb	Ambient

av	Available
b	Bagasse
bc	Base case
bd	Blowdown
bs	Bleed-off steam
C	Carbon
cd	Condenser
$cred$	Credits
ct	Cooling tower
d	Dry; Diameter; Diagonal
dm	Direct method
e	Effective
eb	Energy balance
eco	Economizer
es	Exhaust steam
$evap$	Evaporator
ext	External
f	Flame
fe	Furnace exit
fg	Flue gas
fw	Feedwater
g	Gross
h	Hybrid
hd	Header pipes
hfw	High pressure feedwater heater
htf	Heat transfer fluid
if	Intercept factor
in	Inlet
int	Internal
l	Longitudinal; Loss
lfw	Low pressure feedwater heater
loc	Local
m	Mixture
max	Maximum
min	Minimum
out	Outlet
p	Pump
pro	Process
r	Residue
ref	Reference
sh	Shadowing; Superheated
sc	Sugarcane
se	Solar-to-electricity
sf	Solar field

st	Stoichiometric
t	Tank; Transversal; Turbine
trk	Tracking system
unb	Unburned
w	Wind; Wall

TABLE OF CONTENTS

1 INTRODUCTION

1.1 SCOPE OF PROPOSAL

Solar and biomass are both renewable energy resources which contribute to the electricity generation at low CO_2 emission levels. One important problem related to the biomass power plants operation, however, consists on its availability along the year. This is also true for the sugarcane bagasse power plants in Brazil that are operated mainly during the sugarcane harvest period. In this regard the Concentrated Solar Power (CSP) hybridization of biomass plants has been studied under different configurations. The central idea consists on displacing fuel consumption during sunny hours and providing power supply on a biomass only mode during hours of no solar irradiation incidence - the so-called fuel economy hybridization mode. Solar heat load can also be used to provide power boost during sunny hours - the so-called power boost hybridization mode. These approaches can be applied to new plants and also on existing ones by performing the retrofit of components. Sharing common infrastructure turns possible the reduction of solar energy implementation costs.

The installed capacity of sugarcane bagasse cogeneration plants in Brazil reached 9,930 MW in the first semester of 2015. This amount is produced by 387 units and represents 6.9 % of the Brazilian electricity installed capacity (ANEEL, 2015). In the last decade it has started the modernization cycle of these units aiming the increase of power exportation to the grid. This was motivated by the Brazilian electricity sector decentralization in 2000. Since then, academic works have also been developed to increase these indicators as electricity today consists on an additional product beyond sugar and alcohol (ALVES, 2011; SEABRA, 2008; NETO; RAMON, 2002). In 2013 a total of 15,067 GWh of electricity generated by the sugarcane bagasse cogeneration plants was exported to independent consumers supplying around 8 million homes. Since 2005, an average yearly growth in the electricity exportation of 34 % has been observed (SOUZA, 2014).

The cogeneration plants of sugarcane sector are fueled with bagasse which is a residue obtained after the juice extraction process out of sugarcane culms. The operation takes place during the sugarcane harvest that extends from April to December in the center-south region of Brazil (BNDES; CGEE, 2008). In the rest of the year, most plants remain out of operation and no electricity is produced. In this regard, it was identified in Brazil an opportu-

nity related to the integration of solar thermal energy with the cogeneration plants of sugarcane sector. The solar integration in a fuel economy mode during harvest might provide bagasse reserves which can be used to operate the power plants during off-season. This might minimize the seasonality effect inherent to this crop.

No preliminary works were identified in literature up to now related to the hybridization of cogeneration plants of sugarcane sector with CSP in order to increase electricity exportation to the grid. Thus, in this work this concept is presented and a case study is performed in order to evaluate the integration of a parabolic trough solar field with a typical sugarcane bagasse plant located in Campo Grande, in the State of Mato Grosso do Sul, under thermodynamic and economic aspects. Two integration concepts were evaluated, namely: (a) solar feedwater heating; (b) saturated steam generation with solar energy and post superheating in biomass steam generators. The scope was here limited to the retrofit of conventional cogeneration plants aiming minimal modifications on original installations.

1.2 GOALS

1.2.1 Main goal

The main goal of this work consists in improving the electricity exportation capacity of existing cogeneration power plants applied to the sugarcane sector by integrating them with parabolic trough collectors.

1.2.2 Specific goals

The specific goals are described below:

- Develop a simulation model to reproduce the operation and performance of a parabolic trough solar field;
- Develop a simulation model to reproduce the operation and performance of bagasse cogeneration cycles;
- Define a base case scenario cogeneration plant based on contacts performed with equipment suppliers and sugar and alcohol producers of the sugarcane sector;

- Design and evaluation of distinct integration layouts between the base case cogeneration plant and a parabolic trough solar field in a retrofit scenario;
- Define thermodynamic and economic performance indexes to evaluate the integration layouts;
- Propose an evaluation method to perform additional case studies of CSP hybridization with sugarcane bagasse cogeneration plants.

1.3 STRUCTURE OF DOCUMENT

The literature review on CSP electricity generation and on the Brazilian sugarcane sector is presented on Chapter 2 in order to provide the initial contextualization.

In Chapter 3 it is presented the proposed hybridization method of bagasse cogeneration cycles with CSP, the identified integration layouts and the thermodynamic and economic performance indexes.

The parabolic trough simulation models are presented in Chapter 4, while the implemented models to perform the simulation of bagasse cogeneration cycles are described in Chapter 5.

The base case cogeneration power plant description and simulation results are presented in Chapter 6.

The hybridized cogeneration power plant is described in Chapter 7. In this chapter the results related to the identified integration layouts of cogeneration plant with parabolic trough solar field are compared.

The conclusions are presented in Chapter 8.

2 BACKGROUND

A literature review on Concentrated Solar Power (CSP) electricity generation (Section 2.1) and on the Brazilian sugarcane sector (Section 2.2) is presented in this chapter. The presented information was considered in order to define precisely the scope of this work.

2.1 CONCENTRATED SOLAR POWER

2.1.1 Solar resources around the world

The operation of CSP plants depends on the incidence of Direct Normal Irradiation (DNI). The annual DNI incidence around the world is presented in Figure 1. The regions with the greatest DNI are the deserts of Middle East and North Africa (MENA), the South Africa, the North-Western India, the Southern of the United States, Mexico, Peru, Chile, Northeast of Brazil, Australia and Southern Spain. The accumulated DNI in the South of Spain can reach 2,100 kWh/m^2-year, while it can reach 3,600 kWh/m^2-year in North Chile. In South-West of United States, the DNI index of 2700 kWh/m^2-year is reached. In Brazil, the DNI can overcome 2100 kWh/m^2-year in the region of São Francisco river basin.

Figure 1: World map of DNI.

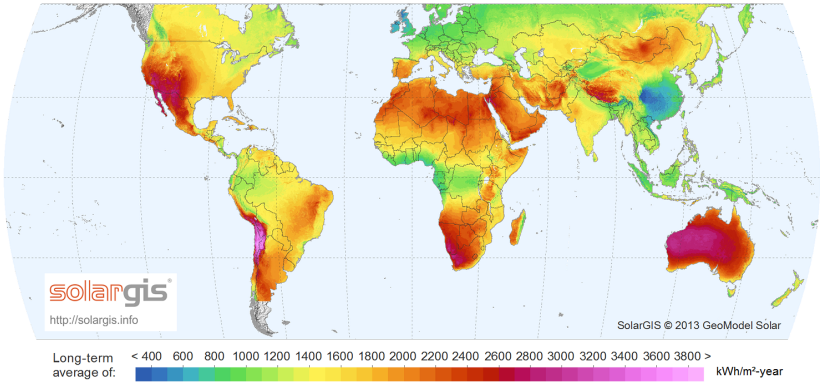

Source: (SOLARGIS, 2014).

The precise indication of required DNI in order a CSP plant to reach

economic feasibility depends on specific characteristics of the project under evaluation, like the following aspects: capital and O&M costs, capacity factor and efficiency of plant, the use of hybridization, electricity contract price, interest rate, among other.

2.1.2 CSP technologies

In general, the ways of concentrating solar energy can be divided into linear and point focusing. Parabolic trough and linear Fresnel belong to the linear focusing technologies, whereas the point focusing are namely central tower and parabolic dish reflectors - see Figure 2. The technical characteristics of the three main commercial CSP technologies are presented in Table 1 for comparison[1].

Figure 2: CSP technologies.

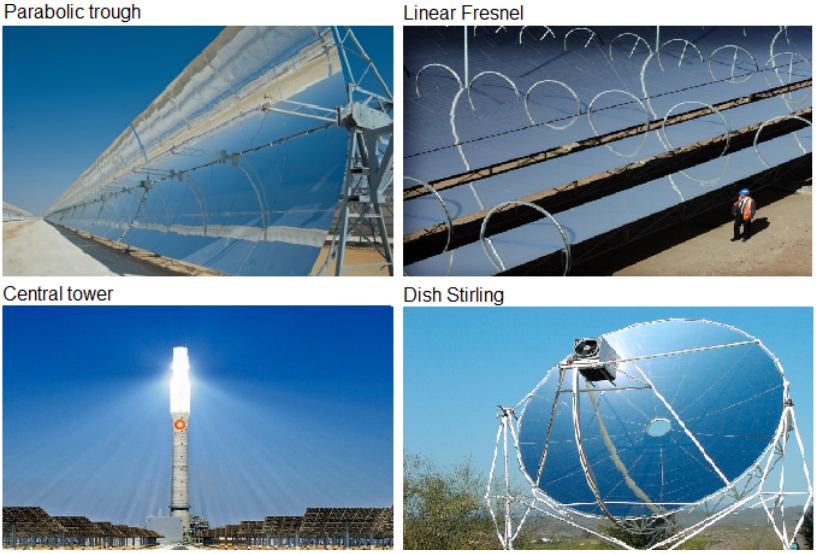

Sources: (SHAMS POWER COMPANY PJSC, 2015); (AREVA SOLAR, 2015); (TORRESOL ENERGY, 2015); (PLATAFORMA SOLAR DE ALMERIA (PSA), 2015)

Parabolic trough represents today the most mature CSP technology, with 88 % share in terms of installed capacity around the world. Typically,

[1]The parabolic dish system is out of scope here once its application is related to distributed generation on a small scale (on the order of some kW).

Table 1: Overview to the three main CSP technologies.

Parameter	Unity	Fresnel	Trough	Tower
Heat transfer fluid (HTF)	-	thermal oil water	thermal oil water molten salt	water molten salt air
Concentration ratio[a]	-	>60	70-80	>1,000
Temperature range[a]	^{o}C	250-500	350-550	565-1,000*
Output range[a]	MW	10-200	10-300	10-200
Peak η_{se}[a,b,**]	%	18	14-24	23-35
Annual η_{se}[a,**]	%	9-13	11-16	7-20
Capacity factor[a]	%	22-24	25-28 43 (7 h)	63 (15 h)
Capacity ratio[c]	%	1	88	11
Construction ratio[d]	%	6	75	18

*Gas turbine applications; **Solar-to-electricity efficiency; Sources: [a](IRENA, 2012); [b](GIOSTRI *et al.*, 2012); [c](SOLARPACES, 2015); [d](RENEWABLES..., 2013).

this system is operated with thermal oil as heat transfer fluid (HTF) with its temperature limited to around 400 ^{o}C. The use of molten salts and direct steam generation (DSG) in trough collectors is currently under development. The capacity factor (CF) of parabolic trough power plants without thermal storage ranges from 25 to 28 %, depending mainly on annual DNI incidence level. The storage of hot thermal oil during sunny hours, nevertheless, provide the improvement of CF to around 40 % - representing 7 h operation at turbine's design point full load. See Turchi (2010) for the description of a typical parabolic trough plant design with thermal storage system.

The linear Fresnel technology emulates the parabolic trough collectors by using a set parallel rows of flat, or slightly curved, glass mirrors to focus direct solar irradiation onto a linear receiver. Once receiver doesn't move as system tracks the sun position, it is suitable for high pressure DSG. An additional special characteristic of Fresnel collectors consists on the compactness of solar field in terms of land usage. The distance between rows in loops can be reduced from 12.5-18 m (trough collectors) up to around 4.5 m. Thermal storage in DSG systems is today in stage of development and typically limited to around 1 h operation at turbine's full load. Tests are being performed in Spain in the Direct Molten Salts (DMS) demonstration project at Puerto Errado One plant (PE1) to adapt Fresnel collectors to the use of molten salts in order to improve heat storage capacity (NOVATEC SOLAR, 2015). As a drawback, the optical efficiency of Fresnel collectors is lower in comparison with parabolic trough especially in the beginning and in the end of the days when

sun is close to horizon, as it is stated by Morin *et al.* (2012).

The central tower point focusing technology can provide the DNI concentration ratio to above 1,000 and thus it is feasible to reach as high as 1,000 ^{o}C operating temperatures. Central tower systems can be operated with DSG, molten salts or yet with air as HTF. The use of molten salts is normally associated with thermal storage. Due to the higher operating temperature in comparison with trough systems, the CF of central tower plants can reach up to 63 % - representing 15 h operation at turbine's full load. This is true once the higher the temperature difference in terms of hot and cold storage tanks, the smaller the necessary HTF volume to provide heat storage and, as a consequence, investment costs are reduced. Finally, due to the higher operating temperatures, the annual solar-to-electricity efficiency of tower systems tend to be higher in comparison with trough and Fresnel plants.

2.1.3 The current world scenario

The distribution of CSP electricity capacity around the world under the status of operational, under construction and under development is presented in Figure 3. Currently the installed capacity of CSP power plants is around 4 GW. Spain represents 58 % of CSP installed capacity, followed by USA that represents around 39 %.

Figure 3: CSP projects around the world.

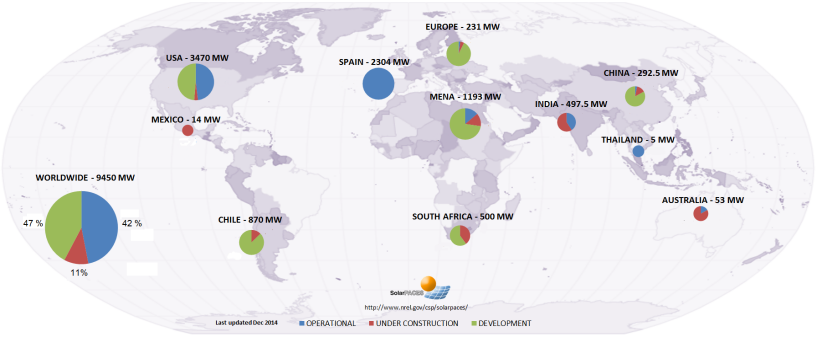

Source: (SOLARPACES, 2015).

In Spain, the improvement of the CSP installed capacity was reached due to governmental incentives which provided feasible and stable prices for renewable electricity commercialization. The Electricity Industry Act in 1997

created the Special Regime, in which it was grouped renewable power generation and cogeneration plants (except the hydropower unities). Incentives were fully guaranteed to CSP plants limited to 50 MW capacity: they consisted in a fixed charge for the participation in the controlled electricity market, or the market price added by a fixed supplement in case of participation in the open electricity market (BOE, 2011). Today, due to economic aspects, the incentives for CSP were ended. This is in agreement with the stagnation in terms of new projects in Spain.

The development of CSP market began in the eighties in USA with the Solar Energy Generating Systems (SEGS) parabolic trough power plants - 354 MW. After 20 years of absence of new projects due to the reduced oil prices, the improvement of CSP capacity started again in 2007 in Spain, later in USA (2012) and currently in Chile, MENA region, South Africa and China. Despite the recent growth, CSP market is yet in its infancy in comparison with other renewable electricity generation technologies. As an example, the installed capacity of photovoltaics today is around 139 GW, from which around 80 GW is installed in Europe (EPIA, 2014).

2.1.4 Technology costs

Ranges for CSP capital expenditure costs (CAPEX) under different solar field technologies and energy storage capacities are summarized in Figure 4. The CAPEX range for ground mounted photovoltaic plants (PV) is also presented for comparison. The linear Fresnel (LF) system has the purpose of presenting reduced investment costs due to the simpler solar field array. In both parabolic trough (PT) and central tower (CT) technologies, the use of energy storage is related to a significant increment in CAPEX. Nevertheless, note that the cost of a trough plant with 6 h storage is compatible with a central tower plant with 12-15 h storage capacity. As exposed in Section 2.1.2, the higher temperature difference in terms of hot and cold tanks turns possible a smaller HTF volume to provide heat storage and, as a consequence, the investment costs are reduced. Data related to photovoltaics are for the ground mounted higher capacity systems, which are more comparable with CSP plants. Note that these systems have lower CAPEX in comparison with any CSP configuration here presented.

Ranges of Levelized Cost of Electricity (LCOE) for parabolic trough[2]

[2]Linear Fresnel LCOE costs are not reported due to reduced references currently under operation.

Figure 4: Capital expenditures (CAPEX) of CSP and PV for comparison.

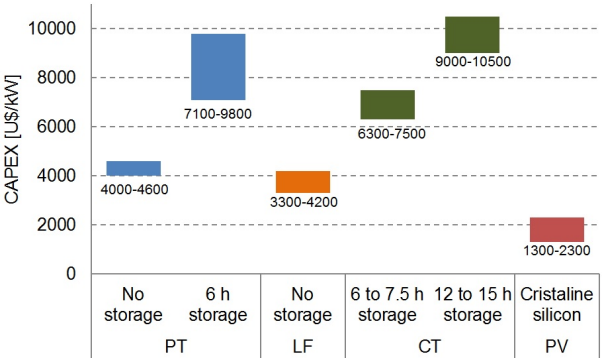

Sources: (IRENA, 2012); (KOST *et al.*, 2013).

and central tower technologies under different storage capacities and for ground mounted photovoltaic plants are summarized in Figure 5. The LCOE method allows the electricity generating costs comparisson of different power plants. The sum of all accumulated costs for building and operating a plant during its life time is compared with the sum of electricity power generation. This then yields the electricity cost necessary to break-even the investment. It is important to note that LCOE cannot be directly considered to define if an investment is feasible or not. For that, a detailed financing calculation must be completed (KOST *et al.*, 2013; IEA, 2010).

The LCOE depends primarily on capital costs, capacity factor (which is related to local DNI incidence and storage capacity) and interest rate. The CSP LCOE data reported by IRENA (2012) is based on a 10 % interest rate, while the photovoltaics LCOE data reported by Kost *et al.* (2013) is based on a range of 4-6 % interest rate values. The CSP energy projects are currently considered more risky by financiers due to their less mature technology status and limited amount of references around the world.

Despite the higher CAPEX of CSP systems equipped with energy storage, the LCOE tends to be reduced due to the improvement of capacity factor. Parabolic trough plants without storage have LCOE of 300-370 U$/MWh, while it can be reduced as low as 210 U$/MWh if a 6 h storage system is used. The LCOE related to central tower technology ranges from 170 to 240 U$/MWh if a 12-15 h storage system is used.

The LCOE of ground mounted photovoltaic utilities (80-182 U$/MWh) is lower in comparison with any CSP configuration here presented. Nevertheless, the main advantage of CSP is the possibility of energy storage. A storage

Figure 5: Levelized Cost of Electricity (LCOE) of CSP and PV for comparison.

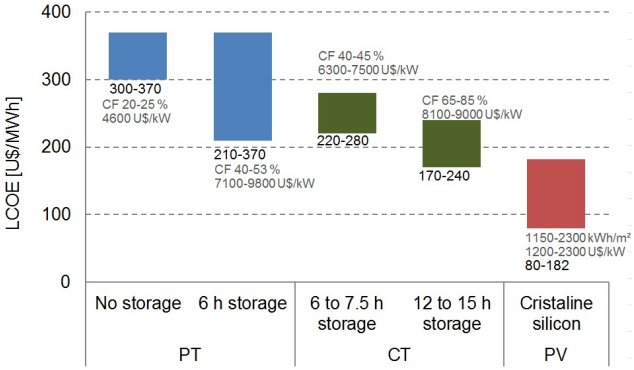

Sources: (IRENA, 2012); (KOST *et al.*, 2013).

system can be implemented in order to shift the generation of electricity for the early evening when there is a peak in demand. Today it is economically unfeasible to store electricity after its generation in photovoltaic panels. In addition, as it will be discussed in Section 2.1.5, CSP is an interesting option for hybridization with traditional fuels like, coal, natural gas or biomass due to similarity by using a water/steam cycle in order to transform the heat energy in electricity. This concept may provide the possibility of firm electricity generation independent on DNI incidence regularity.

Finally, according to IRENA (2012), significant cost reductions in CSP are expected. They might come from economies of scale, learning effects, advances in R&D, a more competitive supply chain and improvements in the performance of the solar field, solar-to-electric efficiency and thermal energy storage systems. Capital cost reductions of 28% to 40% are expected up to 2020, what will bring a direct improvement in LCOE.

2.1.5 CSP hybridization

The CSP hybridization can not only be applied to new plants but also to existing ones. Sharing common infrastructure turns possible the reduction of solar energy generation costs. Furthermore, if solar energy is used to displace fuel consumption during sunny hours, there is the possibility of base load power supply without the implementation of thermal storage systems.

Solar energy can be integrated into combined cycles - Integrated Solar Combined Cycles (ISCC). In ISCC, solar thermal load is used to produce

steam to displace fuel consumption or to generate additional power. Solar-to-electricity efficiency greater than for equivalent operating temperature solar-only plants can be achieved at reduced CAPEX despite the necessity of resized steam turbine in the bottoming cycle (ZHU *et al.*, 2015; MONTES *et al.*, 2011). Compressed air receivers represent a technology currently under development in order to run the so-called solar-gas turbines (SGT). Solar thermal energy is used to heat compressed air to around 1000 ^{o}C. Thus, natural gas consumption can be reduced. High solar-to-electricity efficiency levels are to be obtained due to high operating temperature of solar heat and intrinsic efficiency of combined cycles. In addition, water consumption can be significantly reduced once Bryton gas cycles are used (QUERO *et al.*, 2014).

Steam generators based on coal or biomass combustion can also be hybridized. This concept is here defined as hybridized steam generators (HSG). Peterseim *et al.* (2014a) and Nixon *et al.* (2012) evaluated the operation of CSP in parallel with conventional steam generators producing superheated steam with same parameters. Peterseim *et al.* (2014b) evaluated the efficiency gain due to post superheating of steam produced with a parabolic trough solar field with biomass firing as the concept implemented in SHAMS power plant in United Arab Emirates. Zhao (2012) proposed the production of saturated steam to partially displace the load of a coal fired boiler. Produced saturated steam in solar field was injected back into the conventional steam generator drum for post superheating.

The most explored scheme in literature related to CSP hybridization with Rankine cycles is the so-called solar aided feedwater heating concept (SAFWH). It can be accomplished by the substitution of turbine bleed-off steam extractions by solar heat. Several works demonstrated that the higher the temperature of feedwater heater displaced, the higher the efficiency in terms of power boost or fuel economy (YANG *et al.*, 2011; HOU *et al.*, 2011; POPOV, 2011; YAN *et al.*, 2010; SURESH *et al.*, 2010). As it is discussed by Zhao *et al.* (2014b) and Zhao *et al.* (2014a), solar-to-electricity efficiencies higher than the obtained on solar-only plants under similar operating temperature can be found as the exergy destruction associated to feedwater heating using bleed-off steam is avoided. As further related works, Bakos and Tsechelidou (2013) showed the economic advantages of using the existing infrastructure of a coal power plant to host a solar integration in a feedwater heating scheme in Greece. Hong-juan *et al.* (2013) studied the performance of a solar aided coal power plant under different loads and an optimization procedure was used to identify the most feasible solar multiple. Pierce *et al.* (2013) performed the comparison of a conventional solar-only parabolic trough plant with an

equivalent solar field size used for feedwater heating of a coal fired plant in South Africa. Finally, Peng *et al.* (2014) performed detailed analysis on off-design operation of a solar aided coal fired plant, pointing out the ways to improve system's efficiency.

Relevant results presented in literature are summarized in Table 2 in order to drive a comparison in terms of important performance parameters. In case of adding solar energy to a conventional power plant, the solar share will be limited by the physical restrictions in existing equipments. The annual solar share of 2.4 % was reached in the ISCC concept presented by Bakos and Parsa (2013). In this work, the steam turbine of combined cycle was designed to a higher capacity to improve solar participation in power output. In all SAFWH examples the annual solar share was limited to around 1 % of total electricity output. The improvement of this parameter requires a new project conceptually provided for hybrid operation. This was the case of power plant layout discussed by Peterseim *et al.* (2014a), where both solar field and biomass steam generators were designed to provide the same electricity output of 10 MW. In an annual basis, solar was able to contribute with 20.7 % of total electricity output. The commercial power plant Borges Termosolar located in Spain has the same conceptual design. Solar and biomass systems were balanced to obtain yearly 50 % solar participation on electricity output - see next section about commercial hybrid plants.

The peak solar-to-electricity efficiency of hybridized layouts ranged from 21 to 32 % depending on integration layout, solar field model, operation temperature and efficiency of components. Presented values were in most cases higher than the inherent peak efficiency of the conventional CSP systems exposed in Table 1 of Section 2.1.2. Specifically in SAFWH cases, the solar field temperature was reduced to below the typical level of 400 ^{o}C of parabolic trough plants. The higher the solar-to-electricity efficiency, the smaller the size of solar field (and CAPEX, as a consequence) to generate certain amount of electricity.

Regarding economics, the presented cases indicated levelized cost of solar electricity ranging from the very low value of 70 up to 210 U$/MWh. These values are well below the results indicated for conventional CSP plants in Figure 5. Nevertheless, the comparison should be made cautiously since the input economic parameters are not uniform among all references.

Table 2: Literature data related to CSP hybridization selected for cross-comparison.

Publication	CSP	Output [MW]	Layout	Temperature [^{o}C]‡	Solar share [%]$^{\diamond}$	Location	Peak η_{se} [%]	LCOE [U$/MWh]$^{\sharp}$
(BAKOS; PARSA, 2013)	Trough	50^{CC}-NA^{S}	ISCC	390	0.53-4.1	South Greece	-	-
(MONTES *et al.*, 2011)	Trough	220^{CC}-NA^{S}	ISCC	300	2.4	Las Vegas, USA	27.3	-
Peterseim *et al.* (2014a)	Tower	10^{B}-10^{S}	HSG	>540	20.7	Mildura, AUS	-	-
Peterseim *et al.* (2014b)	Trough	NA^{B}-50^{S}	HSG	390	-	Mildura, AUS	27.5	-
Yang *et al.* (2011)	Trough	200^{C}-19.5^{S}	SAFWH	260	-	-	25.6$^{\triangle}$	-
Hou *et al.* (2011)	Trough	12^{C}-0.4^{S}	SAFWH	230	1.0	Lhasa, China	22.6	77-170$^{\clubsuit}$
Popov (2011)	Fresnel	117^{O}-27^{S}	SAFWH	320	-	Cyprus	27.3$^{\triangle}$	-
Yan *et al.* (2010)	-	200^{C}-20^{S}	SAFWH	330	-	-	32.1$^{\triangle}$	-
Suresh *et al.* (2010)	Trough	660^{C}-25^{S}	SAFWH	280	-	India	23.0	-
Zhao *et al.* (2014a)	Trough	1000^{C}-NA^{S}	SAFWH	300	-	-	27.9	-
Zhao *et al.* (2014b)	Trough	200^{C}-20^{S}	SAFWH	267	-	Shizuishan, China	21.3	-
Bakos and Tsechelidou (2013)	Trough	278^{C}-24^{S}	SAFWH	400	-	Ptolemais, Greece	25.0	100$^{\square}$
Hong-juan *et al.* (2013)	Trough	307^{C}-50^{S}	SAFWH	285	-	Lhasa, China	26.2	71-152$^{\clubsuit}$
Pierce *et al.* (2013)	Trough	600^{C}-22^{S}	SAFWH	350	0.9	Lephalale, S. Africa	-	-
Peng *et al.* (2014)	Trough	330^{C}-16^{S}	SAFWH	300	-	Sinkiang, China	26.3	-
Schuhmacher *et al.* (2013)	Fresnel	12^{B}-0.5^{S}	SAFWH	220	0.63	Brazil, MS	22.2	100-210

S: solar; C: Coal; B: Biomass; O: Oil; CC: Combined cycle; GT: Gas Turbine; ‡Solar field maximum temperature; $^{\diamond}$Annual basis solar participation; $^{\sharp}$Marginal LCOE related to solar equivalent electricity; $^{\triangle}$Estimated based on 70 % peak solar field thermal efficiency; $^{\clubsuit}$1 Chinese yuan = 0.15 U$; $^{\square}$1 Euro = 1.30 U$.

2.1.6 Projects around the world

A list of hybrid CSP projects around the world is presented in Table 3. As it can be observed, most cases are related to the integration of solar energy into combined cycles - the so called ISCC power plants. All cases related to the integration of solar energy into coal fired power plants are based on SAFWH. Finally, the Borges power plant can be mentioned as the only one related to the hybridization of CSP with biomass. The parabolic trough solar field and biomass steam generators are operated in parallel to produce superheated steam with the same temperature and pressure parameters. The solar field was designed to operate the 22.5 MW steam turbine at 100 % load in design point DNI. Biomass system, on the other hand, was designed to operate the steam turbine at 50 % load. In an yearly basis, the equilibrium of 50 % solar share might be achieved according to the local weather conditions.

Table 3: Hybrid CSP projects around the world.

CSP	Plant name	Output [MW]	Location	Layout	Start
Fresnel	Liddell	2000^{C}-9^{S}	Australia	SAFWH	2008
Fresnel	Kogan Kreek	750^{C}-44^{S}	Australia	SAFWH	UC
Fresnel	Mejillones	150^{C}-5^{S}	Chile	SAFWH	PL
Trough	Cameo	49^{C}-1^{S}	USA	SAFWH	2010
Trough	ISCC Hassi	130^{CC}-25^{S}	Algeria	ISCC	2011
Trough	Medicine Hat	203^{CC}-1^{S}	Canada	ISCC	UC
Trough	ISCC Kuraymat	120^{CC}-20^{S}	Egypt	ISCC	2011
Trough	Yazd Solar	467^{CC}-17^{S}	Iran	ISCC	2009
Trough	Archimede	760^{CC}-5^{S}	Italy	ISCC	2010
Trough	Agua Prieta II	464^{CC}-14^{S}	Mexico	ISCC	UC
Trough	Beni Mathar	450^{CC}-20^{S}	Morocco	ISCC	2010
Trough	Martin next	1150^{CC}-75^{S}	USA	ISCC	2010
Trough	Palmdale	570^{CC}-50^{S}	USA	ISCC	PL
Tower	Karaman	450^{CC}-50^{S}	Turkey	ISCC	UC
Tower	Solugas	4.5^{GT}-NA^{S}	Spain	SGT	2012
Trough	Borges	12.0^{B}-22.5^{S}	Spain	HSG	2012

S: Solar; C: Coal; B: Biomass; CC: Combined cycle; GT: Gas Turbine;
UC: Under Construction; PL: Planned; Source: (SOLARPACES, 2015).

2.2 THE BRAZILIAN SUGARCANE SECTOR

2.2.1 Sugarcane sector figures

The land area used for sugarcane plantation in Brazil as well as the sugarcane crushed amount along the last nine harvest periods (plus estimation for the next 2014/15 harvest) are presented in Figure 6. Today the land area used for sugarcane plantation is around 9.0 Mha. It is the third crop in Brazil in terms of used land behind soybeans (28 Mha) and corn (16 Mha) plantations (COMPANHIA NACIONAL DE ABASTECIMENTO (CONAB), 2015). In Brazil, around 60 Mha are used for agricultural purposes, what corresponds to 7 % of national land area (REDEAGRO, 2010). The sugarcane plantations alone corresponds to 1.1 % of national land area.

Figure 6: Sugarcane plantation area in Brazil and annual crushing evolution.

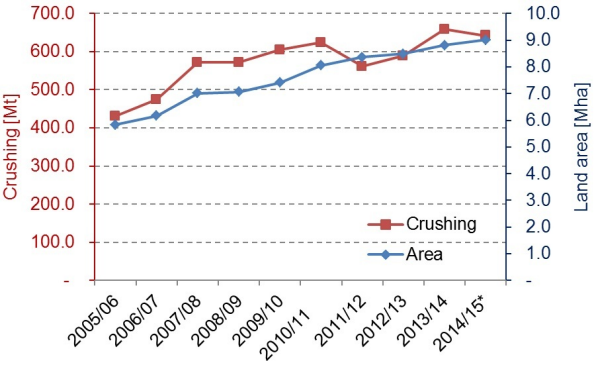

Source: (COMPANHIA NACIONAL DE ABASTECIMENTO (CONAB), 2015).

The sugar and alcohol production along the last nine harvest periods (plus estimation for the next 2014/15 harvest) are presented in Figure 7. Most mills are able to produce both sugar and alcohol and the share is defined according to sugar and alcohol prices. It can be observed that in seasons 2011/12 and 2012/13 the production of sugar was prioritized due to the low price of alcohol in the market.

The production of sugarcane in Brazil is concentrated in the Center-South and North-Northeast regions. The distribution of crushed sugarcane in these two regions is presented in Figure 8 according to the annual milling capacity of factories. The results are based on the 2010/11 harvest period, when 623.9 Mt of sugarcane was crushed. As it can be observed, the capacity

Figure 7: Evolution of sugar and alcohol (total) production in Brazil.

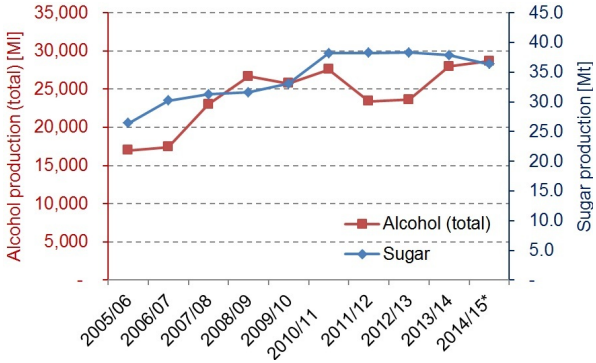

Source: (COMPANHIA NACIONAL DE ABASTECIMENTO (CONAB), 2015).

of industries in the North-Northeast region is concentrated in small unities of less then 1.0 and 1.0-1.5 Mt/harvest. Plants are significantly bigger in terms of annual crushing capacity in the Center-South region of Brazil. Most cases are 2.0-3.0 Mt/harvest. Another important aspect related to both regions consists on the harvest period in these locations. While the harvest period is concentrated between April to December in the Center-South region, in North-Northeast it occurs between August to April (BNDES; CGEE, 2008).

Figure 8: Crushed sugarcane according to industries capacity.

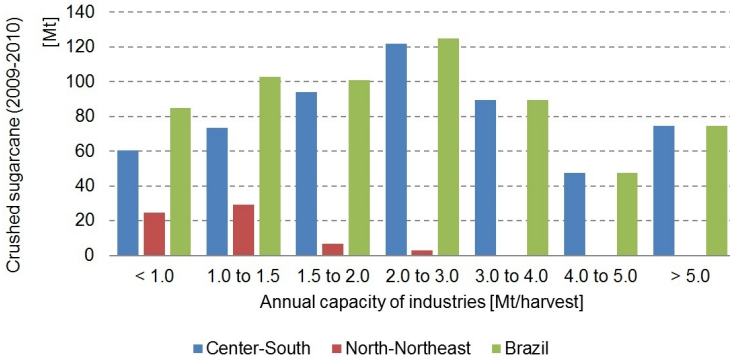

Source: (BRESSAN; ANDRADE, 2013).

2.2.2 Cogeneration cycles

The sugar and alcohol production demands thermal, mechanical and electrical energy. In this regard, the sugarcane mills are equipped with cogeneration power plants based on the combustion of bagasse - a residue obtained after the juice extraction process out of sugarcane culms. The elemental, proximate and calorimetric properties of bagasse are presented in Table 4. The properties of sugarcane straw are also presented once its use has been evaluated recently as a way to complement bagasse in steam generators operating under co-firing[3]. The reported values are typical in the sugarcane sector and represent the average of several evaluations (LAMôNICA; LINERO, 2013). The 50 % moisture content of bagasse consists on its humidity after the juice extraction process as it is feeded in steam generators - typically no drying process is implemented. The 15 % moisture content of straw consists on the average humidity of straw baled in the field (RODRIGUES, 2005).

Table 4: Elemental, proximate and calorimetric (heating value) analysis of sugarcane bagasse and straw.

Fuel type	Bagasse	Straw
Elemental analysis (dry, ash free [%])		
Carbon	45.6	47.9
Hydrogen	5.8	6.4
Nitrogen	0.4	0.6
Oxygen	48.2	44.7
Sulphur	0	0.1
Chlorine	0	0.2
Proximate analysis (as received [%])		
Ash	1.6	7.7
Fixed Carbon	6.9	13.6
Volatile matter	41.6	63.9
Moisture	50	15
Heating value (as received [kJ/kg])		
Higher Heat Value (HHV)	9000	14450
Lower Heat Value (LHV)	7162	12996

Source: (LAMôNICA; LINERO, 2013).

[3]Energetically, for each ton of sugarcane culms there are around 150 kg of sugar (2,400 MJ) and 130 kg of dry bagasse (2,300 MJ). Additional 140 kg of dry straw (2,500 MJ) is left on the field during harvest process (RODRIGUES, 2005). Today part of straw potential is used in some demonstration projects in order to complement bagasse in steam generators (LEAL *et al.*, 2013).

The thermal energy demand in sugarcane mills is related to the evaporation of sugarcane juice and alcohol distillation. In conventional factories able to produce both sugar and alcohol, it is typically demanded 500 tonnes of saturated steam (x=1; 2.5 bar) per ton of processed sugarcane culms. In new plants this index has been reduced to 300-350 tonnes of saturated process steam per ton of sugarcane culms due to optimized process thermal integration and minimization of thermal losses (ENSINAS, 2008). The mechanical energy necessary for sugarcane crushing and juice extraction is typically around 16 kWh per ton of sugarcane culms, while the electricity demand necessary for motors, pumps, illumination, among other services, is typically around 12 kWh per ton of sugarcane culms (SEABRA, 2008).

The four main layouts of cogeneration plants applied to the sugarcane sector are presented in Figure 9. The layouts and operational parameters were optimized along the years, as it is discussed below, in order to improve the electricity production efficiency.

Figure 9: Layouts of cogeneration cycles applied to the sugarcane sector.

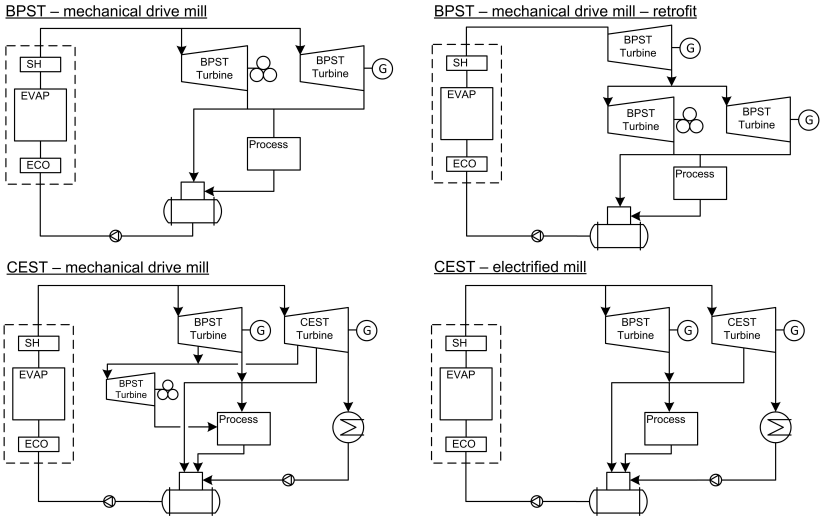

Sources: (SEABRA, 2008; NETO; RAMON, 2002).

Initially, the cogeneration plants were based on the use of back-pressure steam turbines (BPST) with exhaust steam pressure of 2.5 bar used to feed process thermal load. The superheated steam parameters of 22 bar and 300 ^{o}C, associated with the process thermal energy consumption of

500 tonnes of saturated steam (x=1; 2.5 bar) per ton of sugarcane culms, turned possible the self-production of mechanical and electricity demands while burning all the available bagasse produced in juice extraction process. The operation of these plants is dependent on the process operation. Thus, if process is off due to no sugarcane availability, power plant might also be turned off even if bagasse is stored. Furthermore, the reduction of process steam consumption implies bagasse surplus at the end of the harvesting period (NETO; RAMON, 2002).

Since 2000 the electricity exportation to the grid has been an important additional product to the sugarcane factories in Brazil and this was provided by the decentralization of national electricity sector. In this regard, the improvement of cogeneration plants efficiency has been performed in different ways. One option was the retrofit of conventional cogeneration plants based on BPST turbines by replacing existing boilers by new unities with higher steam parameters. The efficiency improvement was so provided by the higher enthalpy drop of steam up to exhaust condition of 2.5 bar (SEABRA, 2008).

The implementation of condensing-extraction steam turbines (CEST) turned possible the operation of cogeneration plants independently on the process operation. In addition, it became convenient to minimize the consumption of process steam (x=1; 2.5 bar) once part of produced steam in boilers can be expanded up to condenser pressure. The efficiency of cogeneration plants was further improved by the substitution of the mechanical drivers in sugarcane mills by the electrified systems. The steam mechanical drivers were single stage low efficiency turbines (SEABRA, 2008).

The evolution of superheated steam parameters (maximum levels available in local industry) of steam generators produced by the main suppliers to the sugarcane sector is presented in Figure 10. From the 70s to 2000 the most common configuration was based on 22 bar and 300 ^{o}C despite the availability of higher steam parameters in the market. Today the standard consists on steam generators able to produce steam at 67 bar and 520 ^{o}C, although 120 bar and 520 ^{o}C steam is also possible in new bubbling fluidized bed systems.

The installed capacity of sugarcane bagasse cogeneration plants in Brazil reached 9,933.6 MW in the first semester of 2015. This amount is produced by 387 units and represents 6.9 % of the Brazilian electricity installed capacity (ANEEL, 2015). In 2013, a total of 15,067 GWh of electricity generated by the sugarcane bagasse cogeneration plants was exported to independent consumers supplying around 8 million homes. Since 2005, an average yearly growth in the electricity exportation of 34 % was observed

Figure 10: Evolution of main steam parameters in the sugarcane sector.

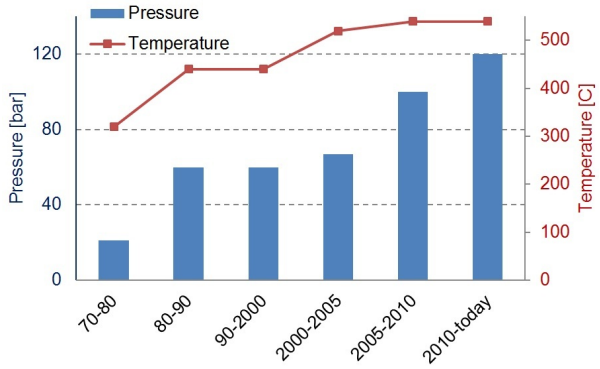

Sources: http://caldema.com.br/; http://www.equipalcool.com.br/; http://www.sermatec.com.br/; http://www.codistil.com.br/.

Figure 11: Evolution exported electricity to the grid.

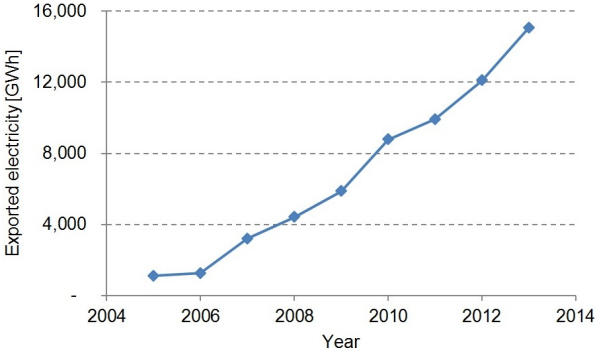

Source: (SOUZA, 2014).

(SOUZA, 2014) - see Figure 11.

2.2.3 The identified potential

The location of sugarcane cogeneration plants and the DNI incidence in Brazil is presented in Figure 12. As it can be observed, Brazil has a great potential regarding solar and biomass availability for electricity power generation. In addition, both energy sources matches regionally in their availability quite good. The DNI incidence can reach up to 2000 kWh/m^2-year in

the Center-South region where most sugarcane mills are located - what is similar to the 2100 kWh/m^2-year level found in South Spain. In this regard, it was identified in Brazil an opportunity related to the integration of solar thermal energy with the cogeneration plants of sugarcane sector. The solar boost might minimize the seasonality effect inherent to this crop extending the operation of the unities to the off-season period. As it is described in Chapter 3, the hybridization layouts evaluated in this work are based on the retrofit of a typical cogeneration power plant applied to the sugarcane sector with parabolic trough concentrators.

Figure 12: Identified potential of CSP hybridization in the sugarcane sector: a) bagasse power plants location; b) integrated annual DNI potential in Brazil.

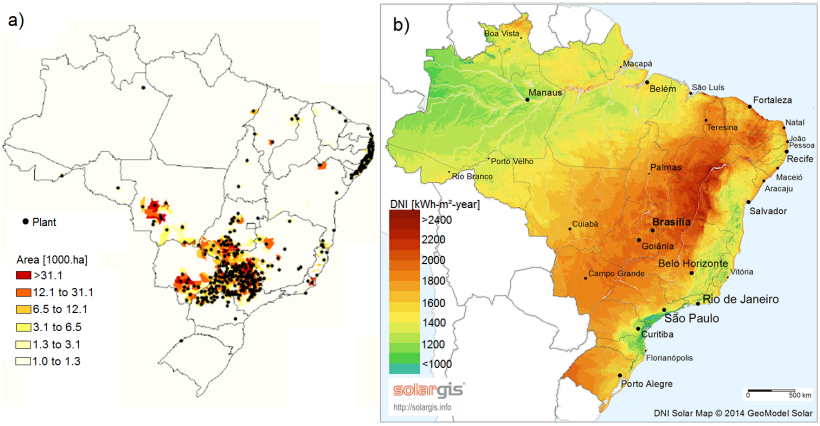

Sources: (JANK, 2011); (SOLARGIS, 2014).

3 HYBRID CONCEPT PROPOSAL

3.1 OPERATION STRATEGY

A schematic of a sugarcane processing industry assisted with solar thermal energy and the proposed operation strategy is presented in Figure 13. The cogeneration plant provides electricity and heat to the process where sugar and alcohol are produced. Surplus electricity is exported to the grid. The concept proposed in this work consists on operating the cogeneration power plant in a fuel economy mode during harvest periods. Thus, stored bagasse is used to run the power plant during off-season.

Figure 13: Schematic of the process and concept illustration.

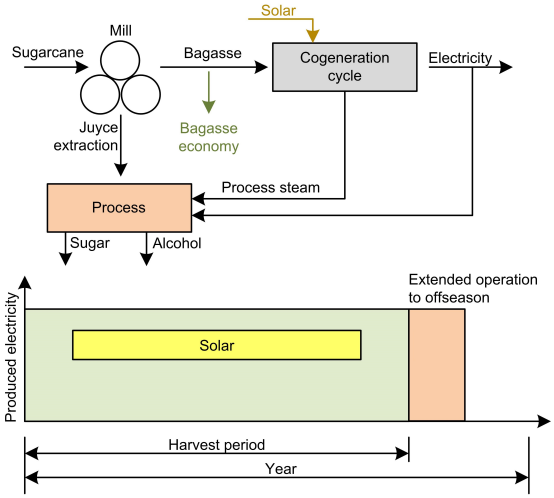

3.2 SELECTED INTEGRATION LAYOUTS

Several integration layouts based on distinct CSP technologies are possible when performing the hybridization of conventional sugarcane bagasse cogeneration plants. This work is focused on parabolic trough technology applied for feedwater pre-heating and also saturated steam generation once it represents the most mature technology in terms of installed capacity (SOLARPACES - SOLAR POWER AND CHEMICAL ENERGY SYSTEMS, 2014). Both the

cogeneration cycle and steam generator layouts as well as the operational parameters were identified in cooperation with equipment suppliers of the sugarcane sector in Brazil. The feasibility of CSP hybridization was studied aiming minimal modifications on original plant.

The layouts studied in this work as well as additional identified possibilities based on linear Fresnel and central tower are shown in Figure 14. All presented cases were evaluated in the research project New Partnerships (iNOPA) funded by the Coordination for the Improvement of Higher Education Personnel (CAPES) and by the German Academic Exchange Service (DAAD) and developed in cooperation between the Laboratory of Combustion and Thermal Systems Engineering (LabCET) of Federal University of Santa Catarina (UFSC) and the Chair of Environmental Process Engineering and Plant Design (LUAT) of University of Duisburg-Essen, Germany. Each CSP technology was applied according to the temperature level required by the integration layout. The results obtained with project execution are summarized in Appendix E and compared with results related to this work.

3.3 THERMOECONOMIC ANALYSIS

A set of performance indexes is described in this section in order to evaluate the integration of a base case cogeneration plant with a parabolic trough solar field. The annual thermal efficiency, η_{sf} [%], of the parabolic trough solar field was calculated based on Equation 3.1,

$$\eta_{sf} = 100 \frac{10^6 \sum_{year} \dot{Q}_{av}}{\sum_{year} A_{sf} \, G_{bn}} \tag{3.1}$$

where $\dot{Q}_{av}$ [MW] is the net heat delivered by solar field, G_{bn} [W/m^2] is the direct normal irradiance and A_{sf} [m^2] the solar field aperture area.

The economized amount of bagasse during harvest operating hours, EB [t], was calculated by Equation 3.2,

$$EB = \sum_{harvest} [\dot{m}_{b,bc} - \dot{m}_{b,h}] \tag{3.2}$$

where $\dot{m}_{b,bc}$ and $\dot{m}_{b,h}$ are the bagasse consumption for base and hybrid cases in tons per hour.

The additional power generated off-season, AE [MWh], due to the economized amount of bagasse was quantified by Equation 3.3,

$$AE = \sum_{off-season} \dot{W}_h \tag{3.3}$$

where $\dot{W}_h$ [MW] is the net power output during off-season for the hybrid plant.

Figure 14: Identified integration layouts of CSP and bagasse cogeneration cycles to be studied.

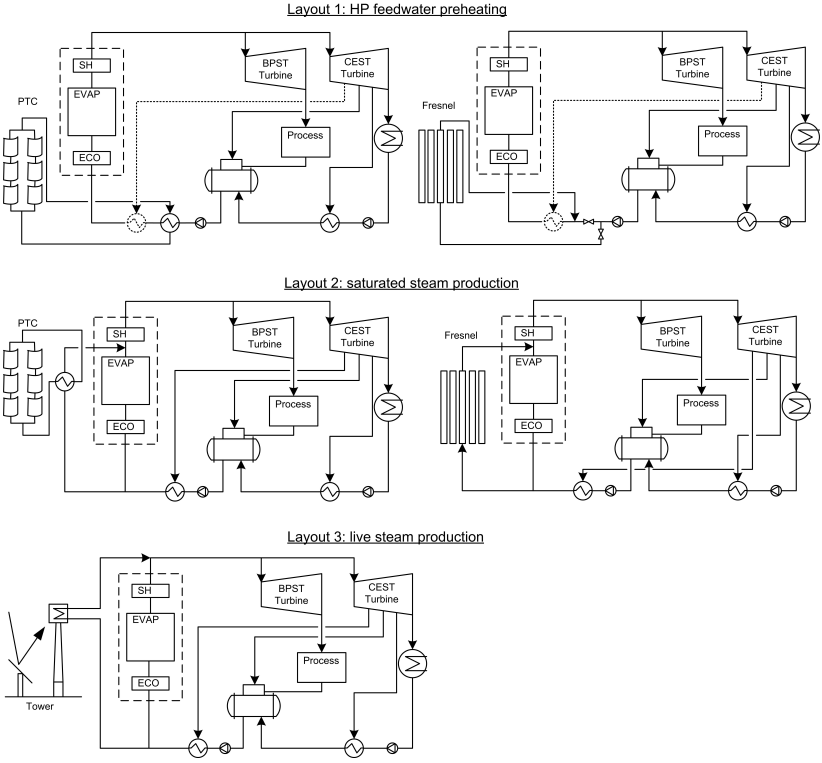

Taking additional power generated AE [MWh] into consideration, the annual solar-to-electricity efficiency was calculated by Equation 3.4.

$$\eta_{se} = 100 \frac{10^6\, AE}{\sum_{year} A_{sf}\, G_{bn}} \tag{3.4}$$

The economic feasibility of a thermal system can be performed under

different methods. Examples of thermoeconomic analysis are found in Esen *et al.* (2006), Bhattacharjee and Dey (2014), Buonomano *et al.* (2015). In this work it was considered the Levelized Cost of Electricity (LCOE) [U$/MWh] calculation according to the methodology proposed in IEA (2010). The LCOE was calculated for the additional power generated off-season, AE [MWh], by comparing it to the capital and annual costs due to solar integration,

$$LCOE = \frac{\sum_{t=0}^{lt}(CC + LC + O\&M)\ (1+r)^{-t}}{\sum_{t=0}^{lt} AE\ (1+r)^{-t}} \tag{3.5}$$

where CC, LC and $O\&M$ [U$] are the capital, land and annual operation and maintenance costs. The parameter r represents the interest rate and lt [years] is the lifetime of plant.

4 SOLAR FIELD MODELING

4.1 MAIN COMPONENTS

A parabolic trough solar field is based on a set of loops which are replicated to reach the required thermal capacity. Each loop consists in a group of Solar Collector Assemblies (SCA) connected in series where the temperature of the heat transfer fluid (HTF) is increased during operating hours. All loops are connected to main header pipes that supply the heat exchangers with hot HTF and sending back to the solar field the cooled HTF. A set of valves is used to provide recirculation at low solar radiation hours and at night time when the required HTF temperature is not reached. Recirculation is necessary during these periods to avoid thermal stress of solar field components. Yet, as HTF has considerable temperature changes, the volume increase due to its volumetric expansion is accommodated in an expansion tank and a set of overflow tanks. An example of a parabolic trough solar field of four loops, each one based on four SCA, is shown in Figure 15[1].

Figure 15: Schematic of a parabolic trough solar field.

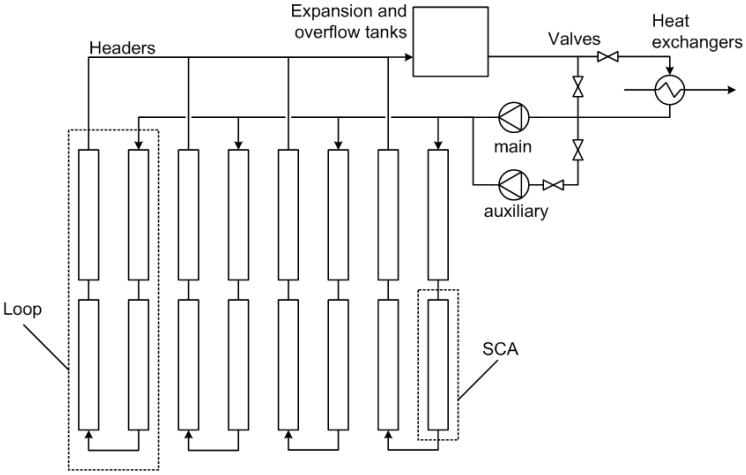

A schematic of one of the parabolic trough loops shown in Figure 15

[1]The number of loops and the number of SCAs per loop may change depending on the specific project characteristics and SCA model. See in Chapter 7 that the proposed solar field layouts differ to the example presented in Figure 15.

is presented in detail in Figure 16. As it can be observed, each SCA has independent tracking system and mirrors are rotated along its horizontal axis tracking the sun position. One SCA is composed by a set of Solar Collector Elements (SCE), which consists in a metallic structure that supports a parabolic shaped mirror and the Heat Collection Element (HCE) located in the focal line. The rows are spaced to minimize shadowing effects at the beginning and at the end of the days.

Figure 16: Schematic of a parabolic trough loop.

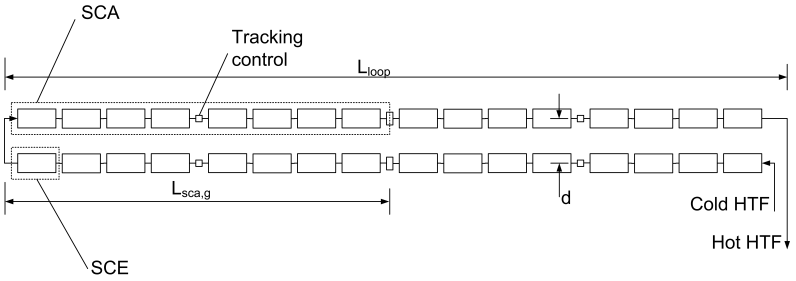

The HCE consists in a metallic tube coated on a selective surface with a high absorptivity for visible spectrum radiation and low emissivity for infrared radiation. A glass envelope with high transmissivity is used to form a vacuum region around the metal tube receiver, thus minimizing losses by convection. A schematic of a HCE is shown at Figure 17.

Figure 17: Schematic of a HCE (not shown in scale).

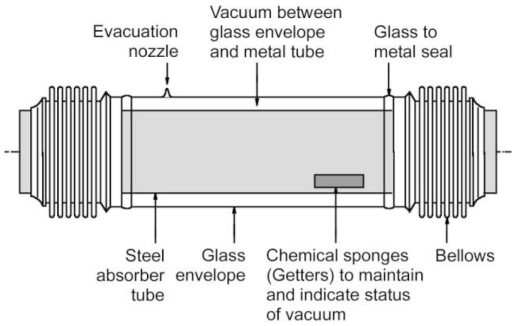

Source: (BURKHOLDER; KUTSCHER, 2009).

In Figure 18 it is shown a solar field equipped with SkyTrough parabolic solar collectors. It can be observed the SCE assemblies together with the HCE elements are positioned in the focal line. Each SCE has six meters

width, 13.9 m length and three HCEs of model SCHOTT PTR-80. One SCA has eight SCE assemblies, totalizing 115 m gross length, $L_{sca,g}$.

Figure 18: SkyTrough parabolic trough collectors.

Source: (SKYFUEL, 2011).

4.2 GEOGRAPHICAL AND METEOROLOGICAL DATA

The plant location might be defined considering the latitude angle ϕ [deg], the local longitude χ_{loc} [deg] and the reference meridian χ_{ref} [deg]. The latitude angle is negative to the south hemisphere and referenced to the equator. The local longitude is referenced to the Greenwich meridian and negative to west. Finally, the reference meridian is necessary to define the local time. There are in total 24 reference meridians of 15 degrees each. As an example, the state of Mato Grosso do Sul in Brazil is represented by -60^o.

When performing feasibility assessments of solar thermal systems by simulations it is necessary to consider representative meteorological data sets for the location of interest. A Typical Meteorological Year (TMY) summarizes a long time series of measurements (e.g. 30 years) in order the typical weather conditions can be represented whereas the average effects of the whole data base is preserved. It is important to note that TMY data is not indicated to simulate extreme operational conditions, but typical. TMY data for some locations of Brazil can be found in SWERA database (SWERA, 2015). Important variables are solar radiation, ambient temperature and wind velocity.

4.3 LOCAL AND SOLAR TIME

The local time t_{loc} is related to the reference Greenwich meridian χ_{ref}. In order to perform simulations of solar plants it is necessary, nevertheless, to consider apparent solar time t_{sun}. The conversion of t_{loc} to t_{sun}, both given in hours, was here performed in daily basis using Equation 4.1 (DUFFIE; BECKMAN, 1980),

$$t_{sun} = t_{loc} + (\chi_{ref} - \chi_{loc})/15 + ET/60 \tag{4.1}$$

where the correction term ET [min] was calculated according to Equation 4.2 proposed by Spencer (1971). The argument Γ was given by Equation 4.3, where n represents the day of the year ($n = 1$: 1st January).

$$\begin{aligned} ET = 229.18\ (&0.000075 + 0.001868\ cos\,\Gamma - \\ &0.032077\ sen\,\Gamma - 0.014615\ cos\,2\Gamma - 0.04089\ sen\,2\Gamma) \end{aligned} \tag{4.2}$$

$$\Gamma = 2\,\pi\,(n-1)/365 \tag{4.3}$$

4.4 INCIDENCE ANGLE

The incidence angle in a parabolic trough collector tracking the sun about a horizontal north-south axis is formed by the vector normal to the aperture area and direct normal irradiance G_{bn} [W/m^2] (Figure 19). Once G_{bn} [W/m^2] is related to the plane normal to its propagation it is necessary to apply the factor cos(θ) in order to calculate the total incident energy rate in solar collectors. The angle θ [rad] was here calculated by Equation 4.4, as described by Duffie and Beckman (1980),

$$\theta = acos\left(\sqrt{cos^2\,\theta_z + cos^2\,\gamma\,cos^2\,\omega}\right) \tag{4.4}$$

where ψ and α_s (both in radians) represent, respectively, the azimuth (Equation 4.5) and solar altitude (Equation 4.6) angles. The angle ψ is referenced to the south direction and it is positive in the morning, that is, to the east. The angle α_s is complementary to zenith, θ_z, and $\theta_z + \alpha_s = \pi/2$.

Figure 19: Incidence angle formed by the vector normal to collector's aperture area and direct irradiance.

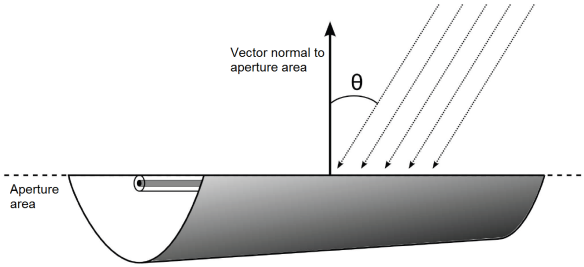

Source: (WAGNER; GILMAN, 2011).

$$\psi = acos\left(\frac{sen\,\alpha_s\,sin\,\phi\,\frac{\pi}{180} - sin\,\delta}{cos\,\alpha_s\,cos\,\phi\,\frac{\pi}{180}}\right) \tag{4.5}$$

$$\alpha_s = asin(sin\,\phi\,\frac{\pi}{180}\,sin\,\delta + cos\,\phi\,\frac{\pi}{180}\,cos\,\delta\,cos\,\omega) \tag{4.6}$$

Equations 4.5 and 4.6 presented previously are functions of latitude ϕ [deg], declination δ [rad] and time angle ω [rad]. The declination angle was calculated by Equation 4.7 proposed by Spencer (1971), where the argument Γ is represented by Equation 4.3 presented before. The time angle, finally, was calculated according to Equation 4.8 (DUFFIE; BECKMAN, 1980).

$$\begin{aligned}\delta = (&0.006918 - 0.399912\,cos\,\Gamma + 0.070257\,sen\,\Gamma - \\ &0.006758\,cos\,2\Gamma + 0.000907\,sen\,2\Gamma - \\ &0.002697\,cos\,3\Gamma + 0.00148\,sen\,3\Gamma)\end{aligned} \tag{4.7}$$

$$\omega = (12 - t_{sun})\,15\,\pi/180 \tag{4.8}$$

4.5 SOLAR IRRADIANCE ABSORPTION

The effective aperture area of solar field, A_{sf} [m^2], corresponds to the sum of each SCA's aperture area where there is the incidence of solar irradiance, G_{bn} [W/m^2]. Due to several factors that will be described in next sections, just part of $G_{bn} \cdot A_{sf} \cdot cos\,\theta$ energy rate is absorbed by HTF, as it is stated by Equation 4.9 (PATNODE, 2006),

$$\dot{Q}_{abs} = G_{bn}\, A_{sf}\, cos\,\theta\, \eta_{opt,0}\, IAM(\theta) \\ f_{sh}\, f_{end}\, f_{cl,sce}\, f_{cl,hce}\, f_{trk}\, f_{add} \tag{4.9}$$

where $\dot{Q}_{abs}$ [W] is the heat transfer rate to HTF, $\eta_{opt,0}$ [-] is the peak optical efficiency of solar field (Section 4.5.1), *IAM* [-] is the incidence angle modifier (Section 4.5.2) and f_{sh} and f_{end} [-] account for losses due to shadowing and end losses (Section 4.5.3). The terms $f_{cl,sca}$, $f_{cl,hce}$, f_{trk} and f_{add} [-] are degradation factors caused by soiling in mirrors, absorber tubes, tracking system and additional factors (Section 4.5.4).

4.5.1 Peak optical efficiency

The peak optical efficiency is observed when the incidence angle, θ, is equal to zero degrees, HTF temperature is equal to ambient temperature (no heat losses to ambient) and when mirrors and absorber tubes are clean. The efficiency $\eta_{opt,0}$ can be measured experimentally. In this work, Equation 4.10 was used to estimate this parameter (MANZOLINI *et al.*, 2011a),

$$\eta_{opt,0} = \rho\, \tau\, \alpha\, f_{if} \tag{4.10}$$

where ρ [-] represents the reflectivity of mirrors, τ [-] the transmissivity of glass envelope, α [-] the absorptivity of metal tube selective coating, f_{if} [-] is the intercept factor that account for geometric errors (mirrors alignment) and on the reduction of effective length of absorber tubes due to shadowing caused by supports and expansion bellows. The values of parameters used in Equation 4.10 for three different models of trough collectors are presented in Table 6 of Section 4.12. In this work the simulations were performed considering the LS-2 SCA.

In Figure 20 it is presented the result obtained by García-Cortés *et al.* (2012) where photogrammetry was applied to identify the geometric errors of a parabolic trough collector. The marked points correspond to the intercepts in the vertical plane passing through HCE. Notice that part of the simulated rays do not focus on the region in which the HCE is positioned due to the geometric imperfections in mirror.

Figure 20: Intercept factor calculation in a parabolic trough concentrator using photogrammetry.

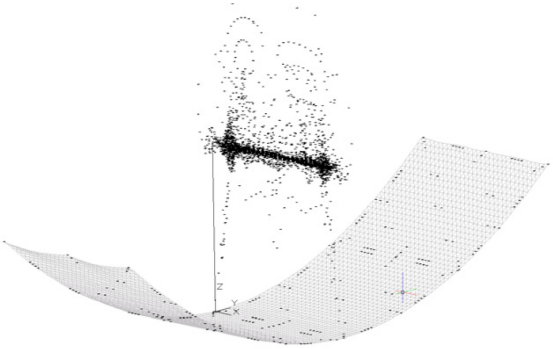

Source: (GARCíA-CORTéS *et al.*, 2012).

4.5.2 Incidence angle modifier

In addition to $cos\,\theta$, the incidence angle modifier (IAM) accounts for variations in optical efficiency of collectors due to intercept factor, reflectivity, transmissivity and absorptivity variations caused by the oblique incidence of irradiance. The index $\mathrm{IAM}(\theta)$ was measured experimentally and fitted by Equation 4.11, where θ is given in degrees (DUDLEY, 1994).

$$IAM(\theta) = 1 - C_0 \frac{\theta}{cos\,\theta} + C_1 \frac{\theta^2}{cos\,\theta} \tag{4.11}$$

In this work the fitting coefficients C_0 =3.5E-4 and C_1 =3.1E-5 presented by Dudley (1994) for the LS-2 SCA model equiped with the Luz Cermet evacuated HCE receiver were considered in simulations. Additional results for the IST-PT1 SCA model are reported by Dudley (1995).

4.5.3 Shadowing and end losses

In the beginning and in the end of the day when the sun is close to horizon, one line of collectors can shade the next line and the effective solar field aperture area, A_{sf} [m^2], is decreased. In this work this was calculated according to Equation 4.12 presented by Stuetzle (2002),

$$f_{sh} = max\left[0,\ min\left(1,\ \frac{d}{w}\frac{sin(\alpha_s)}{cos(\theta)}\right)\right] \tag{4.12}$$

where d [m] is the spacing between rows measured from center to center longitudinal axes of collectors and w [m] is the width of parabolic collectors.

End losses always occur if incidence angle is different from zero. As it is presented in Figure 21 part of HCE is not exposed to reflected irradiance. The f_{end} factor was here calculated according to Equation 4.13 presented by Dudley (1994),

$$f_{end} = 1 - \frac{fl\ tan(\theta)}{L_{sca}} \tag{4.13}$$

where fl [m] is the average focal length of parabola and L_{sca} [m] is the effective length of each SCA.

Figure 21: Representation of irradiation end losses.

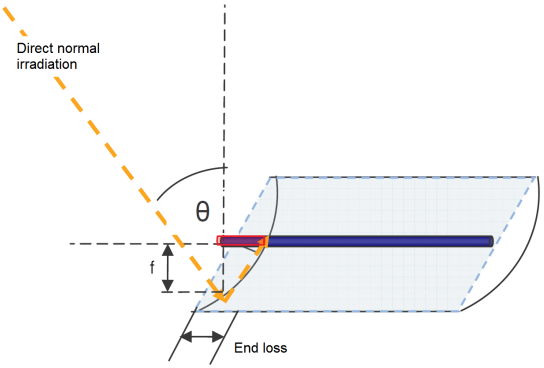

Source: (PATNODE, 2006).

4.5.4 Additional factors

The parameters $f_{cl,sce}$, $f_{cl,hce}$, f_{trk} and f_{add} are degradation factors that reduce the optical efficiency of solar collectors. The terms $f_{cl,sce}$ and $f_{cl,hce}$ are due to soiling in mirrors and evacuated tubes. Continuous cleaning cycles are implemented in CSP power plants in order to keep optical efficiency of collectors as high as possible. Normally the whole solar field is cleaned once or twice a week depending on ambient and soil conditions - field evaluations

for sites close to sugarcane processing industries are not yet available. The accuracy of sun tracking system is proportional to f_{trk}. Finally, effects not accounted are assigned to f_{add} in order to fit simulated performance to real system's performance.

The values of degradation parameters used to perform the simulation of SEGS VI power plant are reported in Forristall (2003). These values are listed in Table 14 of Chapter 7 of this work as they were used to perform the simulations in the sugarcane region and also in the solar field model verification process described in Appendix A.

4.6 HEAT LOSSES

4.6.1 Heat collector elements

Part of solar irradiance absorbed by HTF is lost to the ambient on heat collectors elements. In this work it was used the empirical model represented by Equation 4.14 proposed by Burkholder and Kutscher (2009). This model is also implemented in System Advisor Model (SAM) simulation tool developed by National Renewable Energy Laboratory (NREL) (WAGNER; GILMAN, 2011),

$$\begin{aligned}
\dot{Q}'_{l} &= \frac{\dot{Q}'_{l,1}+\dot{Q}'_{l,2}+\dot{Q}'_{l,3}+\dot{Q}'_{l,4}}{T_{out}-T_{in}} \\
\dot{Q}'_{l,1} &= (C_0+C_5\sqrt{V_w})(T_{out}-T_{in}) \\
\dot{Q}'_{l,2} &= (C_1+C_6\sqrt{V_w})\left(\frac{T_{out}^2-T_{in}^2}{2}-T_{amb}(T_{out}-T_{in})\right) \\
\dot{Q}'_{l,3} &= \frac{C_2+C_4\ G_{bn}\ IAM(\theta)\ cos(\theta)}{3}(T_{out}^3-T_{in}^3) \\
\dot{Q}'_{l,4} &= \frac{C_3}{4}(T_{out}^4-T_{in}^4)
\end{aligned} \tag{4.14}$$

where $\dot{Q}'_{l}$ [W/m] represents heat transfer rate per unit length of HCE, C_0 to C_6 are fitting parameters and V_w [m/s] is the wind velocity. The heat loss per square meter of solar field aperture area, $\dot{Q}''_{l}$ [W/m^2], was obtained by Equation 4.15.

$$\dot{Q}''_{l} = \dot{Q}'_{l}/w \tag{4.15}$$

where w [m] is the SCA width.

Part of the results reported by Burkholder and Kutscher (2009) for

Luz Cermet HCE used in LS-2 solar collectors are summarized in Table 5. In case of lost vacuum the glass envelope of HCE has a leak and air has leaked through it and resides in the annulus at atmospheric pressure. Additional results available in SAM database are related to SCHOTT PTR-70 and Solel UVAC models of HCE.

Table 5: Coeficients of heat loss model (Equation 4.14) fitted for Luz Cermet HCE.

Parameter	Luz Cermet, vacuum	Luz Cermet, lost vacuum
C_0	2.42	0.64
C_1	0.21	0.83
C_2	-0.0005	-0.00014
C_3	6.9E-6	6.0E-6
C_4	9.6E-8	4.2E-8
C_5	-2.25	-5.67
C_6	0.032	0.18

Source: (BURKHOLDER; KUTSCHER, 2009).

4.6.2 Header pipes

Heat loss also occurs in headers (see Figure 15). A detailed modeling approach is described in Kelly and Kearney (2004) report. In this work the empirical correlation derived by Patnode (2006) was implemented (Equation 4.16). Field data of SEGS VI power plant operation was considered to fit a polynomial model where heat loss per square meter of solar field aperture area, $\dot{Q}''_{hd}$ [W/m^2], was given as a function of average HTF temperature difference to the ambient,

$$\dot{Q}''_{hd} = 0.0169\,\Delta T - 1.683E-4\,\Delta T^2 + 6.780E-7\,\Delta T^3 \tag{4.16}$$

where ΔT [^{o}C] consists on the average HTF temperature difference to the ambient (Equation 4.17). The terms T_{in} and T_{out} are inlet and outlet temperatures of HTF in solar collectors and T_{amb} is the ambient dry bulb temperature.

$$\Delta T = \frac{T_{out} + T_{in}}{2} - T_{amb} \tag{4.17}$$

4.7 NET HEAT RATE AND TEMPERATURE OUTPUT

For steady state operation regime, the net heat rate delivered by solar field, $\dot{Q}_{av}$ [W], was found discounting from absorbed heat rate the terms related heat loss in HCE and in header pipes. This was calculated by Equation 4.18.

$$\dot{Q}_{av} = \left[\dot{Q}_{abs} - A_{sf}\left(\dot{Q}''_{l} + \dot{Q}''_{hd}\right)\right] / 10^6 \tag{4.18}$$

Once $\dot{Q}_{av}$ [MW] was found, the enthalpy gain of HTF was determined by Equation 4.19. The terms $\rho_{in} \cdot \dot{V}_{in}$ represent the HTF mass flow rate calculated in solar field inlet.

$$\Delta h = \frac{\dot{Q}_{av}\, 10^3}{\rho(T_{in})\, \dot{V}_{in}} \tag{4.19}$$

Finally, the output HTF enthalpy was found by Equation 4.20.

$$h_{out} = h_{in} + \Delta h \tag{4.20}$$

In Annex A the properties of thermal oil Therminol VP-1 by Solutia® (SOLUTIA, 2014) are presented.

4.8 THERMAL INERTIA

The models described in this section do not represent thermal capacitance of the heat transfer fluid in solar field and in expansion and overflow tanks. Thus, a fully-mixed adiabatic storage tank model was implemented as an artifice in order to account for thermal capacitance effects. This approach was tested by Stuetzle (2002) and Patnode (2006) to reproduce the operation of SEGS VI plant.

The storage tank was located between the solar field and the heat exchangers that connect solar field with water-steam cycle. The governing model that represents storage tank was given by Equation 4.21,

$$M_t\, cp_t\, \frac{dT}{dt} = \dot{m}_{htf}\left(h_{in} - h_{out}\right) \tag{4.21}$$

where M_t [kg] is the mass of HTF in the tank, cp_t [kJ/kg K] is the specific heat at constant pressure of HTF in the tank, $\dot{m}_{htf}$ [kg/s] mass flow rate of HTF

entering and leaving the tank, dT/dt [^{o}C/s] is the change of HTF temperature in the tank with time.

The mass of fluid in the fully-mixed adiabatic storage tank was constant and it was sized to provide an equivalent mass as the HTF residing in the solar field (evacuated tubes) and expansion and overflow vessels. The fully-mixed storage tank assumption consisted also that the temperature inside tank and in the exit flow were the same. The average temperature was changed over time as inlet temperature was changed.

The calculated mass of HTF for SEGS VI plant simulation was set as 313 tonnes by Stuetzle (2002) and Patnode (2006). In this work, the stored HTF mass on the fully-mixed storage tank of each evaluated solar field layout presented in Chapter 7 was considered proportional to the corresponding solar field aperture area. The proportionality factor was given by the stored HTF mass to solar field aperture area ratio of SEGS VI design.

4.9 HEAT TRANSFER FLUID PUMPING

The electricity consumption due to thermal oil pumping $\dot{W}_p$ [MW] was calculated by Equation 4.22,

$$\dot{W}_p = \frac{\dot{m}_{htf}\,\Delta p}{\eta_p\,\rho_{htf}\,10} \tag{4.22}$$

where η_p refers to pumping system efficiency, ρ_{htf} [kg/m^3] to the heat transfer fluid density and Δp [bar] to the pressure drop across the solar field and header pipes. The term Δp was updated at off-design part load heat transfer fluid mass flow rate according to Equations 4.23 and 4.24.

$$\Delta p = k_{\Delta p}\,\dot{m}_{htf}^2 \tag{4.23}$$

$$k_{\Delta p} = \frac{\Delta p_{ref}}{\dot{m}_{htf,ref}^2} \tag{4.24}$$

The heat transfer fluid pumping system efficiency was updated at part load once deep part load was achieved at the beginning and at the end of operation days. In this work, the procedure adopted by Lippke (1995) was implemented (Equation 4.25), where $\eta_{p,ref}$ corresponds to the design efficiency and η_p to its value at off-design. This model was built to fit the global part load efficiency of pumping system of SEGS VI plant which consists on

the operation of two variable speed HTF pumps positioned in series.

$$\frac{\eta_p}{\eta_{p,ref}} = -0.4 + 2.8\,\frac{\dot{m}_{htf}}{\dot{m}_{htf,ref}} - 1.4\left(\frac{\dot{m}_{htf}}{\dot{m}_{htf,ref}}\right)^2 \tag{4.25}$$

4.10 HEAT EXCHANGERS MODELING

Hot HTF from solar field is used in parabolic trough plants (e.g. SEGS plants in California) to generate superheated steam. The SEGS VI power plant layout is presented in Figure 43 of Appendix A as an example. As it can be observed, a set of heat exchangers are used: economizers, evaporators, superheaters and re-heaters. In the specific case of integration layouts studied in this work, only economizers and evaporators were used once no superheated steam generation and re-heat were performed (see Chapter 3).

4.10.1 Economizer

The economizer provides pre-heating of feedwater. It consisted here in a shell-and-tube counter flow heat exchanger with HTF in the shell side. The overall heat transfer coefficient-area product, UA_{eco} [kW/K], was dependent on mass flows of water and HTF, as represented by Equation 4.26 (PATNODE, 2006),

$$\frac{UA_{eco}}{UA_{eco,ref}} = \left(\frac{\dot{m}_{fw}^{0.8}\,\dot{m}_{htf}^{0.8}}{\dot{m}_{fw,ref}^{0.8}\,\dot{m}_{htf,ref}^{0.8}}\right)\left(\frac{\dot{m}_{fw,ref}^{0.8}+\dot{m}_{htf,ref}^{0.8}}{\dot{m}_{fw}^{0.8}+\dot{m}_{htf}^{0.8}}\right) \tag{4.26}$$

where the subscripts fw and htf refer to feedwater and heat transfer fluid, respectively, and ref refers to design point operational condition. The reference operational parameters $UA_{eco,ref}$ [kW/K], $\dot{m}_{fw,ref}$ and $\dot{m}_{htf,ref}$ [t/h] are those identified at design point operation.

4.10.2 Boiler

The evaporation process was performed in a boiler composed of two parts, as shown in Figure 22. The steam drum in the top is connected to

the evaporators positioned below with external downcomers and risers. The water circulation is natural caused by the difference in density between the saturated liquid and vapor/liquid mixture. The bundle of tubes in the evaporation section is exposed to a cross flow of boiling water. The HTF flows in the tubes side (AALBORG CSP, 2015).

Figure 22: Illustration of a boiler implemented in a parabolic trough plant.

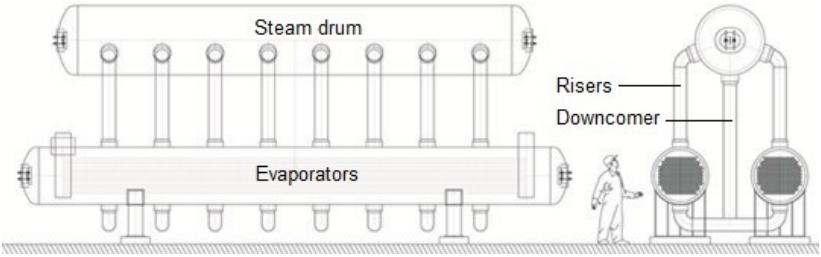

Source: (AALBORG CSP, 2015).

The performance of the CSP boiler was predicted by the ε-NTU method (BERGMAN *et al.*, 2008). The overall heat transfer coefficient-area product UA_{evap} [kW/K] of evaporation section in the bundle of tubes was updated regarding the ratio of actual HTF mass flow to its design reference value, as represented by Equation 4.27 (PATNODE, 2006). This equation considers that UA_{evap} is relatively less sensible to the steam mass flow variation.

$$\frac{UA_{evap}}{UA_{evap,ref}} = \left(\frac{\dot{m}_{htf}}{\dot{m}_{htf,ref}} \right)^{0.8} \tag{4.27}$$

4.11 OPERATION STRATEGY

A simplified strategy was implemented in this work to reproduce the operation of a parabolic trough solar field performed by an operator employee. At night or during long periods of no direct irradiance an auxiliary pumping system was used for HTF recirculation. It was considered that this system was able to provide HTF volume flow of around 10 % of nominal flow of main pumping system as reported by Turchi (2010).

When there was the incidence of significant direct solar irradiance

(here defined as 100 W/m^2 according to the procedure reported by Xcel (2011)), the main pumping system was turned on and HTF volume flow was controlled in order to reach HTF goal temperature in the output of solar field. Defocusing was applied in part of solar field area when HTF temperature in output of solar field was close to maximum temperature of thermal fluid. This process happened when G_{bn} was too high and HTF pumping system was operated at full load.

Finally, the HTF from solar field output was always directed to the storage tank described in Section 4.8. If the HTF temperature in the output of storage tank was greater than the minimum required temperature, then HTF was directed to the heat exchangers. If not, recirculation was performed.

The minimum required temperature depended on the integration layout. In case of feedwater heating, the HTF temperature should be higher than feedwater temperature in economizer's inlet. In case of saturated steam generation, the HTF temperature should be higher than the saturated steam temperature.

The implemented operation strategy is summarized in Figure 23

4.12 COMMERCIAL COMPONENTS

In Table 6 the characteristics of three commercial parabolic trough collectors are presented for comparison. The development of new models is performed in order to improve optical and thermal efficiency and to reduce costs involved in fabrication and assembly. The LS-2 collectors are equipped with evacuated Luz Cermet HCEs. The SkyTrough collector by SkyFuel® is equipped with SCHOTT PTR-80 HCE. Finally, IST-PT1 is presented as an option to lower operational temperatures, as hot water supply to residences or industrial processes.

The simulations performed in this work considered the use of LS-2 collectors equiped with evacuated Luz Cermet HCEs due to the greater amount available data in literature and real operation data that turned possible the verification of implemented models.

4.13 MODEL VERIFICATION

The solar field model verification is presented in Appendix A where simulation results are compared with real operation data of SEGS VI power

plant equiped with LS-2 SCAs and evacuated Luz Cermet HCEs. The real operation data is reported by Stuetzle (2002).

Figure 23: Solar field operation stragegy.

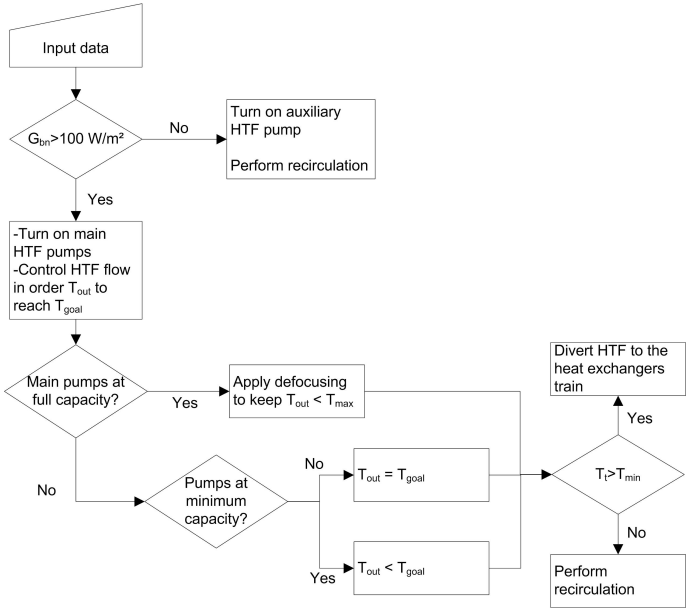

Table 6: Example of commercial models of parabolic trough collectors.

Parameter	Unity	LS-2	SkyTrough	IST-PT1
Temperature range	[^{o}C]	100-400	200-500	100-300
SCA area, A_{sca}	[m^2]	235.5	656.0	13.2
SCA width, w	[m]	5	5.75	2.30
SCA gross length, $L_{sca,g}$	[m]	50	115	6.1
# of SCE per SCA	-	6	8	NA
Average focal dist., fl	[m]	1.84	1.71	0.80
Mirrors reflectivity, ρ	-	0.94	0.94	0.93
Intercept factor, f_{if}	-	0.93	NA	NA
HCE transmissivity, τ	-	0.96	0.96	0.96
HCE absorptivity, α	-	0.96	0.96	0.97

Sources: (DUDLEY, 1994; DUDLEY, 1995);
(FERNáNDEZ-GARCíA *et al.*, 2010; SKYFUEL, 2011).

5 COGENERATION PLANT MODELING

The models implemented to identify the thermodynamic performance of a cogeneration cycle applied to the sugarcane sector are presented in the following sections. Special atention was given to the off-design simulation of power plant components once they may operate at significantly different conditions during harvest and off-season as well when solar heat is integrated in the base case steam cycle.

5.1 STEAM GENERATORS

As exposed in Section 3.2, a parabolic trough solar field might be integrated with a bagasse cogeneration plant to provide solar feedwater preheating (Layout 1) and to produce saturated steam in parallel with steam generators (Layout 2). In both scenarios, the performance of bagasse steam generators might be affected once the thermal load is reduced during sunny hours due to fuel economy operation. Specially in case of Layout 2, it is also necessary to modify the water-steam circuit of the bagasse steam generators and the upper limit of integrated solar heat might be identified in order to avoid strong imbalances.

The set of implemented equations and hypothesis adopted to reproduce the performance of the sugarcane bagasse steam generators are described in Appendix B. The focus was based on natural circulation subcritical water tube steam generators composed of combustion chamber, boiler, convective superheating system, economizer and tubular air heaters.

5.2 STEAM TURBINES

5.2.1 Steam expansion across a turbine stage

Once the feedwater heater bleed-off steam was replaced by solar energy, the steam flow to the last stages of condensing turbine was increased. In this regard, the pressure drop across a turbine stage due to steam expansion was here evaluated as a function of steam mass flow according to the Flügel formula represented by Equation 5.1 (SHLYAKHIN, 2005). This model is valid when steam velocities are lower than critical at nozzle exits and the reference

parameters are previously known.

$$\frac{\dot{m}_s^2}{\dot{m}_{s,ref}^2} = \frac{p_{out}^2 - p_{in}^2}{p_{out,ref}^2 - p_{in,ref}^2} \tag{5.1}$$

5.2.2 Efficiency at off-design operation

The operation of a steam turbine stage at off-design may change its isentropic efficiency in comparison with design point. In this work the isentropic efficiency was modeled as a function of steam mass flow according to Equation 5.2 (JUEDES *et al.*, 2009),

$$\frac{\eta_{t,iso}}{\eta_{t,iso,ref}} = C_4 \left(\frac{\dot{m}_s}{\dot{m}_{s,ref}}\right)^4 + C_3 \left(\frac{\dot{m}_s}{\dot{m}_{s,ref}}\right)^3 + C_2 \left(\frac{\dot{m}_s}{\dot{m}_{s,ref}}\right)^2 + C_1 \left(\frac{\dot{m}_s}{\dot{m}_{s,ref}}\right) + C_0 \tag{5.2}$$

where $\eta_{t,iso,ref}$ is the reference isentropic efficiency of turbine at design point operation, $\eta_{t,iso}$ is the updated off-design efficiency, $\dot{m}_{s,ref}$ is the reference and $\dot{m}_s$ is the off-design mass flow of turbine stage. The parameters C_0 to C_4 were fitted according to empirical part load operation data.

In case of condensing turbines, the efficiency $\eta_{t,iso}$ was also adjusted with respect to changes in the inlet and outlet steam quality (x_{in} and x_{out}). When the steam quality was lower than 1, the adjustment was given by Equation 5.3.

$$\eta_{t,iso,corr} = \eta_{t,iso} - \frac{1}{2}\left(2 - x_{in} - x_{out}\right) \tag{5.3}$$

5.2.3 Power output

The net power output of a turbine stage was calculated according to,

$$\dot{W}_t = \eta_{t,mec}\ \eta_{t,el}\ \dot{m}\ \left(h_{in} - h_{out}\right) \tag{5.4}$$

where $\dot{m}\ (h_{in} - h_{out})$ represents energy output of expanded fluid, $\eta_{t,mec}$ is the efficiency of mechanical system (bearing, coupling, heat loss) and $\eta_{t,el}$ is the

electrical efficiency of generator.

The output enthalpy of exhaust steam is achieved considering the isentropic efficiency of the turbine stage as it is stated by Equation 5.5.

$$\eta_{t,iso} = \frac{(h_{in} - h_{out})}{(h_{in} - h_{out,s})} \tag{5.5}$$

5.3 CONDENSER AND COOLING TOWER

The performance of condenser was predicted by the ε-NTU method (BERGMAN *et al.*, 2008). It was considered a shell-and-tube heat exchanger and its overall heat transfer coefficient-area product UA_{cd} [kW/K] was updated regarding the ratio of actual cooling water mass flow to its design reference value, as represented by Equation 5.6 (PATNODE, 2006). This equation considers that UA_{cd} is relatively less sensible to the steam mass flow variation.

$$\frac{UA_{cd}}{UA_{cd,ref}} = \left(\frac{\dot{m}_{cw}}{\dot{m}_{cw,ref}}\right)^{0.8} \tag{5.6}$$

Regarding the cooling tower, its performance was modeled considering the ε-NTU method implemented by Rice (1991) for a counter-flow configuration. The number of heat transfer units NTU_{ct} of cooling tower was a function of the cooling water and cooling air mass flow ratio, as shown in Equation 5.7,

$$NTU_{ct} = c\left(\frac{\dot{m}_{cw}}{\dot{m}_{ca}}\right)^{1+n} \tag{5.7}$$

where c and n are empirical parameters chosen equal to 1.14 and 1.75 in this work as reported by Patnode (2006). The subscripts *ca* and *cw* represents cooling air and cooling water, respectively.

5.4 PUMPS

The auxiliary electricity power required for a pump operation, $\dot{W}_p$ [kW], was modeled according to Equation 5.8,

$$\dot{W}_p = \frac{\dot{m}\,(h_{out} - h_{in})}{\eta_{p,mec}\;\eta_{p,el}} \tag{5.8}$$

where $\dot{m}\,(h_{out} - h_{in})$ represents energy gain of pumped fluid, $\eta_{p,mec}$ is the efficiency of mechanical system (bearing, coupling, heat loss) and $\eta_{p,el}$ is the efficiency of electric motor.

The output enthalpy of pumped fluid was achieved considering the isentropic efficiency of pump as it is stated by Equation 5.9. In case of cogeneration cycle modeling, the isentropic efficiency of pumps were considered constant.

$$\eta_{p,iso} = \frac{(h_{in} - h_{out,s})}{(h_{in} - h_{out})} \tag{5.9}$$

5.5 FEEDWATER HEATERS

The performance of the feedwater heaters was predicted by the ε-NTU method in the same way as for the condenser. The overall heat transfer coefficient-area product UA_{fw} [kW/K] was updated regarding the ratio of actual feedwater mass flow to its design reference value and considering that UA_{fw} was relatively less sensible to the bleed-off steam mass flow variation.

The mass flow of bleed-off steam was determined by a condensate purge as heat transfer to feedwater occured. The final feedwater temperature was calculated according to the energy balance described by Equation 5.10,

$$\dot{m}_{bs} = \frac{\dot{m}_{fw}\,(h_{fw,out} - h_{fw,in})}{(h_{bs,in} - h_{bs,out})} \tag{5.10}$$

where the subscript *bs* represents bleed-off steam obtained from turbine.

5.6 DEAERATOR

A simplified sketch of a deaerator system with condensate and make-up water as liquid water inputs is represented at Figure 24.

The steam supplied to the deaerator is provided in order to maintain inside pressure at required value. The level control system defines the mass flow of make-up water required. Inlet liquid water streams are boiled to remove dissolved gases to protect the plant from corrosion. The contact of

Figure 24: Deaerator simplified scheme.

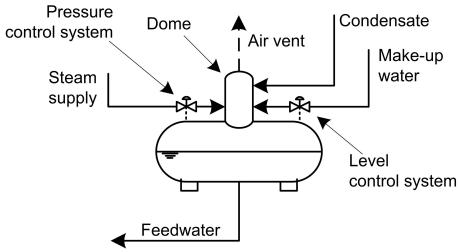

steam and liquid water occurs at dome breaking the water into as many small drops as possible and surrounding these drops with an atmosphere of steam. Injection of steam into the storing vessel can also be performed where the bubbling effect also provides dissolved gases removing. The operation of a pressurized deaerator reduces the oxygen concentration to a minimum (< 20 parts per billion) without the use of chemicals (SPIRAX SARCO, 2014).

Deaerator was modeled in this work considering energy balance according to Equation 5.11. Heat loss to ambient was neglected, as well as air vent stream mass flow.

$$\sum_{i=1}^{M} \dot{m}_{in,i}\, h_{in,i} = \sum_{j=1}^{N} \dot{m}_{out,j}\, h_{out,j} \tag{5.11}$$

5.7 HEAT AND ELECTRICITY PROCESS DEMAND

The process heat load used for sugar and alcohol production, $\dot{Q}_{pro}$ [MW], was calculated according to Equation 5.12,

$$\dot{Q}_{pro} = \frac{q_{pro}\, \dot{m}_{sc}}{10^3} = \frac{\dot{m}_{es}\, (h_{es,in} - h_{es,out})}{3.6\ 10^3} \tag{5.12}$$

where q_{pro} [kWh/t] is the heat demand per ton of processed sugarcane, $\dot{m}_{sc}$ [t/h] is the amount of processed sugarcane, $\dot{m}_{es}$ [t/h] is the mass flow of exhaust steam, $h_{es,in}$ [kJ/kg] is the enthalpy of exhaust steam and $h_{es,out}$ [kJ/kg] the enthalpy of condensate. The process steam used for sugar and alcohol production in the sugarcane sector in Brazil consists tipicaly on 2.5 bar saturated steam.

The electricity demand of process, $\dot{W}_{pro}$ [MW], was calculated according to Equation 5.13,

$$\dot{W}_{pro} = \frac{w_{pro}\,\dot{m}_{sc}}{10^3} \tag{5.13}$$

where w_{pro} represents the electricity demand per ton of processed sugarcane.

5.8 HARVEST OPERATING DAYS

The total duration of sugarcane harvest is mainly dictated by rainfall, as during rainy hours as well as during the necessary time for soil drying it is not possible to harvest sugarcane. When evaluating the integration of a cogeneration plant with solar collectors it is important to identify the rainy and drying days. The solar field operating hours during harvest can be identified and, as a consequence, the fuel economy potential.

In this work, it was defined a straightforward approach in this regard. To identify the operating days of sugarcane processing industry, the daily rainfall intensity was classified in four main categories and each one related to the necessary drying period. This is represented by,

$$drying\ period = \begin{cases} 0, & rainfall \leq 5\ mm/m^2 \\ 1\ day, & 5\ mm/m^2 < rainfall < 25\ mm/m^2 \\ 2\ days, & 25\ mm/m^2 \leq rainfall < 45\ mm/m^2 \\ 3\ days, & rainfall \geq 45\ mm/m^2 \end{cases}$$

where a drying day was defined as a sunny day with no precipitation above 5 mm per square meter necessary after a rainy period to provide field drying. The necessary drying days were cumulative.

It was considered that if sugarcane processing industry was out of operation due to no sugarcane harvesting, the cogeneration cycle was turned off as well. In general, the operation strategy adopted in the sugarcane sector is not restricted to this case. There may be in some unities the interest to keep the cogeneration cycle operation even on days when no sugarcane is harvested. In this scenario, bagasse might be stored so it can be burned in these rainy and soil drying days.

6 BASE CASE COGENERATION PLANT

6.1 GENERAL ASSUMPTIONS

Plant site and TMY data used in simulations are described in Table 7. The state of Mato Grosso do Sul consisted on the focus of this work due to the high incidence of new greenfield cogeneration power plants. The code and approach here developed can be extended to other regions of interest.

Table 7: Cogeneration power plant site and TMY data.

Plant site	Campo Grande - Mato Grosso do Sul
Coordinates	(-20.45; -54.62)
TMY data	Meteonorm® 7.0
Time resolution	1-hour

The simulation of base case cogeneration power plant was performed using the Engineering Equation Solver® (EES) Matlab® (used specifically to perform the steam generators modeling in order to avoid the convergence problems obtained under the use of EES).

6.2 COGENERATION PLANT DESCRIPTION

A hypothetical sugarcane bagasse cogeneration plant with configuration and operational parameters identified in cooperation with equipment suppliers was simulated to evaluate its integration with solar thermal energy. The layout and main results related to the simulation of cogeneration plant at design point peak summer operation are presented in Figure 25. The steam cycle was equipped with two 170 t/h capacity steam generators that produced superheated steam at 525 ^{o}C / 67 bar (point 1). The base case scenario was operated during harvest burning 142.5 t/h of bagasse from sugarcane crushing station. The major part of superheated steam (point 2, 220 t/h) was expanded in the back-pressure turbine (BPST) until 2.5 bar as required by process heat demand. In parallel, roughly one third of the superheated steam (point 6, 117 t/h) was expanded in the condensing-extraction turbine (CEST). Three extractions were implemented in CEST turbine to preheat feedwater to 200 ^{o}C (point 20). The CEST exhaust steam (point 10) was condensed in a wet-cooled condenser. The assumptions adopted for cogeneration cycle simulation are presented at Table 8.

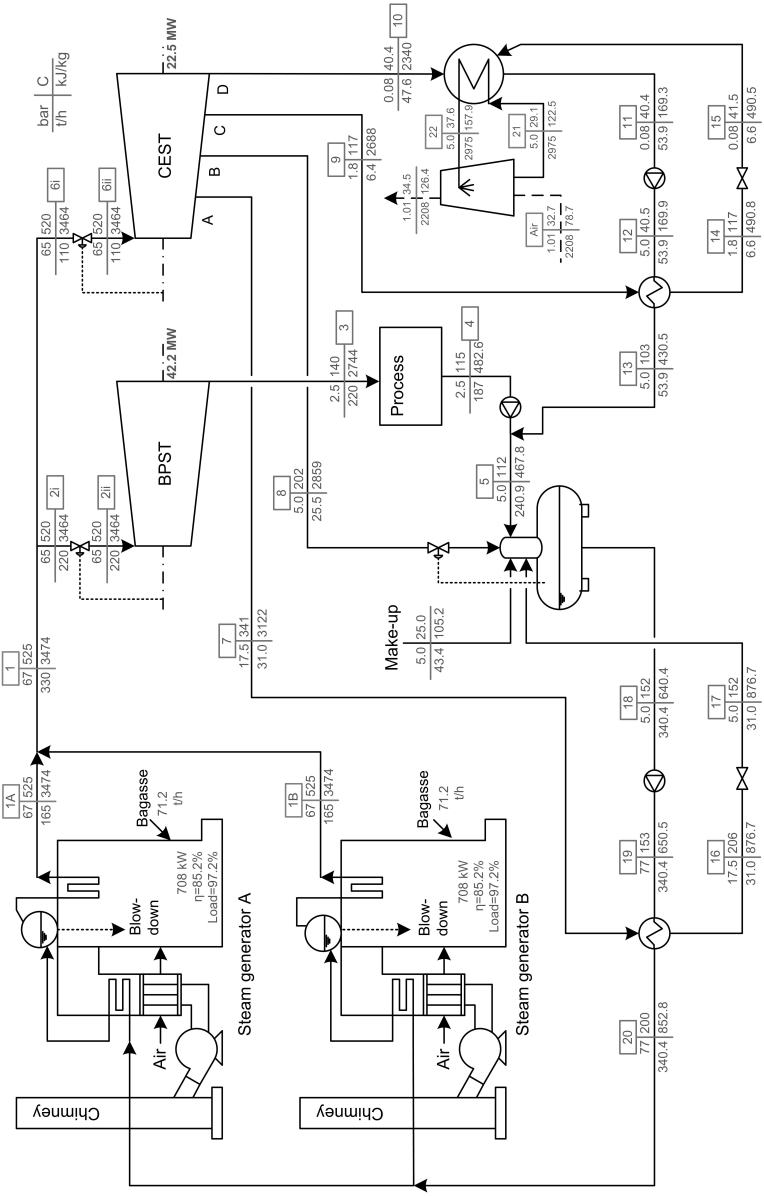

Figure 25: Base case cogeneration power plant layout and simulation results at design point operation.

The properties of sugarcane bagasse considered in simulations are presented at Table 4 of Chapter 2. To calculate the amount of produced bagasse at the sugarcane crushing station output the bagasse content in sugarcane (dry basis) was considered equal to 12.5 % (LAMôNICA; LINERO, 2013). Based on this assumption, 250 kg of wet bagasse with a moisture content of 50 % was produced for each ton of crushed sugarcane. It was considered that 95 % of wet bagasse was directly burned at steam generator, while the remaining 5 % was stored as a back-up to start the plant on next coming season.

Table 8: Design point assumptions adopted for cogeneration cycle simulation.

Parameters	Unit	Adopted assumption
Sugarcane milling capacity, $\dot{m}_{sc}$	t/h	600
Sugarcane milled yearly	Mt	3
Harvest start	-	01st April
Bagasse content in sugarcane (dry)[a]	%	12.5
Isentropic efficiency of BPST[†]	%	89
Isentropic efficiency of CEST (A to D)[†]	%	86; 88; 88; 75
Electromechanical generators efficiency[†]	%	96
Isentropic efficiency of pumps[†]	%	78
Electromechanical efficiency of pumps[†]	%	96
Condenser capacity, $UA_{cd,ref}$	kW/K	4000
Low pressure heater capacity $UA_{lfw,ref}$	kW/K	105
High pressure heater capacity $UA_{hfw,ref}$	kW/K	905
Steam generators auxiliary power, w_{sg}	MW/MW	0.05
Process electricity consumption, w_{pro}	kWh/t	28
Process heat consumption, q_{pro}	kWh/t	230
Peak summer temperature[‡], $T_{amb,ref}$	^{o}C	33.5; 25.5 (WB)

Source: [a](LAMôNICA; LINERO, 2013).
[†]Equipment manufacturer data; [‡]See Appendix C for design point calculation.

Two 170 t/h capacity steam generators were used in the evaluated cogeneration power plant. Each steam generator unity was equiped with an over feed stoker furnace, membrane walls, convective superheaters (SH1 and SH2), one economizer and two tubular air heaters (AH1 and AH2). The evaporation occurred along the water wall panels enclosing the biomass combustion chamber. One steam temperature control using dessuperheater was located between SH1 and SH2. In Table 9 are presented the heat exchange area, the longitudinal s_l and transversal s_t spacing of tubes, the external diameter d_{ext} and thickness t of tubes as well as the arrangement of bundle of tubes. In Table 10 are presented the adopted assumptions related to the thermal losses of steam generators at design point.

Table 9: Configuration of heat exchangers used in superheaters, economizer and air heaters of studied steam generators.

Parameter	Unit	SH2	SH1	ECO	AH2	AH1
Area	m^2	520.5	1041.0	1307.5	3030.0	3030.0
s_l	mm	134.0	134.0	134.0	87.0	87.0
s_t	mm	102.0	102.0	100.0	100.0	100.0
d_{ext}	mm	44.5	44.5	50.8	63.6	63.6
t	mm	3.8	3.8	3.8	2.3	2.3
Arrangement	-	Aligned	Aligned	Aligned	Scattered	Scattered

Source: Equipment manufacturer data.

Table 10: Design point assumptions adopted for steam generators simulation.

Parameters	Unit	Adopted assumption
Heat loss to ambient	% of $\dot{m}_b \cdot LHV$	0.8
Ash collection points[a]		
Furnace bottom, α	-	0.28
Economizer exit, β	-	0.32
Between AH1 and AH2, γ	-	0.40
Unburned carbon[a]		
Furnace bottom, $C_{r,\alpha,ref}$	-	0.20
Economizer exit, $C_{r,\beta,ref}$	-	0.15
Between AH1 and AH2, $C_{r,\gamma,ref}$	-	0.10
CO emission[b], $CO_{fg,ref}$	mg/Nm^3	100
Blowdown	% of SH mass flow	3

Source: [a](PRIETO, 2003); [b](LOO; KOPPEJAN, 2008).

The results of design point operation of steam generators are presented in Figure 26. As it can be seen, 209.2 t/h of air was preheated from ambient temperature to 285.6 ^{o}C. Additional 23.2 t/h of air (10 % of total) was used as bagasse carrying air. Both streams consisted in 30 % air excess as required to optimize combustion process. Feedwater (170.2 t/h) was heated from 200 to 276.6 ^{o}C in economizer. Blowdown consisted of 3 % of main steam mass flow in order to maintain impurities concentration under specification limits. Finally, 165.2 t/h superheated steam was produced by heating saturated steam until required final parameters (525 ^{o}C / 67 bar). It was here assumed that saturated steam prevenient from boiler drum was at x=1 and 72 bar. In practice the saturated steam quality would be $x \leq 0.99$ and it could be also changed at part load operation. It is also important to notice that 13.9 t/h of saturated water (x=0 / 72 bar) was injected between SH1 and SH2 at design point operation. At part load this amount was gradually reduced to keep main steam temperature constant.

Figure 26: Base case steam generator simulation results at design point operation.

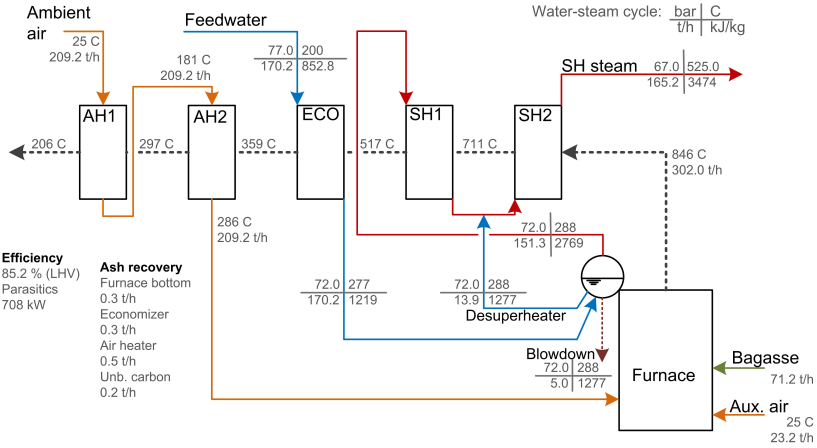

The results related to cogeneration power plant simulation at design point operation in harvest are summarized in Table 11.

Table 11: Bagasse mass flow rate and electric power production at design point operation.

Parameter	Unit	Value
Produced bagasse	t/h	150.0
Burned bagasse	t/h	142.5
Stored bagasse	t/h	7.5
BPST gross output	MW	42.3
CEST gross output	MW	22.5
Net electricity production	MW	62.3
Auxiliary electricity consumption	MW	2.5
Process electricity consumption	MW	16.8
Process heat consumption	MW	138.2
Net electricity exported to the grid	MW	45.5

6.3 OFF-DESIGN SIMULATION

The existing unburned carbon content in residue streams and CO emission in case of inefficient combustion were assigned as input data in order

to simulate the part load performance of steam generators. Regarding CO emission, the general profile presented in Figure 49 of Section B.1.3.4 was adopted as a first approximation. No clear information was found in the literature related to unburned carbon content in residues, C_r [kg/kg], for bagasse fired steam generators under part load operation[1]. In this regard, four different curves expressing the variation of C_r according to fuel mass flow were proposed in order to compose a sensitive analysis (see Figure 27). For the base case scenario, C_r was increased by 100 % in comparison with reference $C_{r,ref}$ (full load operation) when fuel flow was reduced by 50 %. In opposition to the base case scenario, it was considered that unburned carbon content in residues was moderately increased (test 2), considered constant (test 3) and reduced (test 4) at part load.

Figure 27: Unburned carbon sensitive analysis.

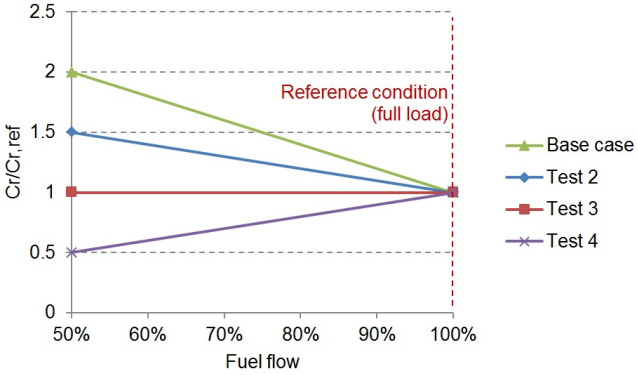

Air excess profile at part load operation consisted on gradually increasing it linearly as procedure adopted by the contacted manufacturer:

- At 100 % fuel mass flow: 30 % air excess;
- At 50 % fuel mass flow: 40 % air excess.

The part load efficiency of steam generators (based on LHV calculation - see Section B.1.5 of Appendix B) are presented in Figure 28 for the different tests performed regarding unburned carbon content in residue streams. As it can be observed, the higher the unburned carbon content, the lower the efficiency of steam generators at reduced load.

[1] See in Sections B.1.1 and B.1.3.3 how C_r [kg/kg] affects steam generator's efficiency.

Figure 28: Part load efficiency (LHV basis) profiles for the different tests performed regarding the unburned carbon content in ash.

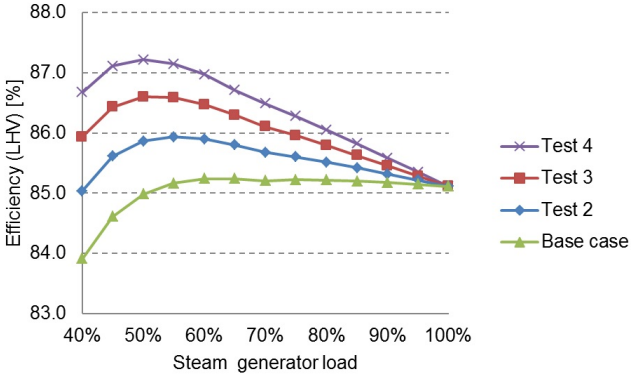

The feasibility of solar integration might be influenced by steam generator's efficiency. This is discussed in Section 7.4.1 of Chapter 7 where the different unburned carbon tests are considered in a sensitive analysis. Notice that the remaining results presented in this chapter related to the part load performance of steam generators and cogeneration cycle concern the base case scenario described in Figure 27.

The calculated heat loss components presented as percentage of fuel's heat input are shown in Figure 29. As load was decreased, the flue gas temperature in the control volume exit was lower and the sensible heat losses related to dry flue gas and flue gas humidity was reduced. The gain in terms of efficiency was, on the other hand, contrasted with increased losses related to CO emission, unburned carbon and heat loss to the ambient.

The steam temperature profiles at part load are presented in Figure 30. Attemperation consisted on injecting saturated liquid water from boiler drum in between SH1 and SH2 modules in order to reduce the steam temperature before it entered in SH2 (see SH1-Output and SH2-Input curves). As it can be observed, there was an operation limit in which attemperation flow was totally closed and supererheated steam final temperature (SH2-output) could not be maintained anymore at design point (here equal to 525 ^{o}C). The lower limit occurred in 70 % load as specified by the contacted manufacturer.

Finally, the cogeneration cycle was designed to operate also during off-season period if bagasse was available. This represents an approach currently adopted in the sugarcane sector where electricity production can be improved by purchasing bagasse if market prices are favourable. The results related to cogeneration power plant off-season operation during off-season

are presented in Figure 31 and Table 12. During this period no sugarcane crushing was performed and industry was out of operation. The power plant Was operated with one steam generator at 65 % load (110 t/h steam). The second steam generator and BPST turbine were both turned off. The calculated condensing temperature was equal to 49.0 ^{o}C once exhaust steam mass flow rate was higher (78.8 t/h) when compared to harvest condition. It is important to notice that cooling system might be designed to meet this worst case associated with peak summer weather condition that coincides with the off-season.

Figure 29: Participation of the distinct losses (LHV basis) at part load.

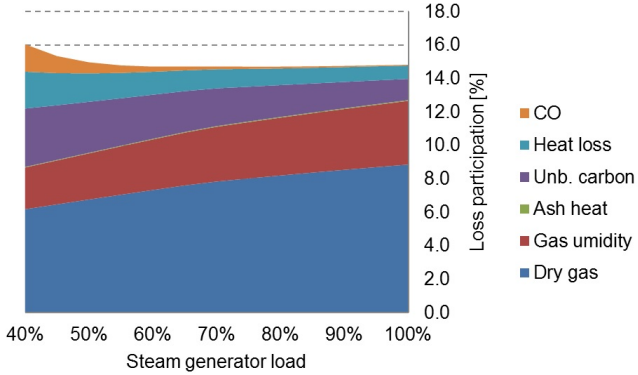

Figure 30: Steam temperature profiles at part load.

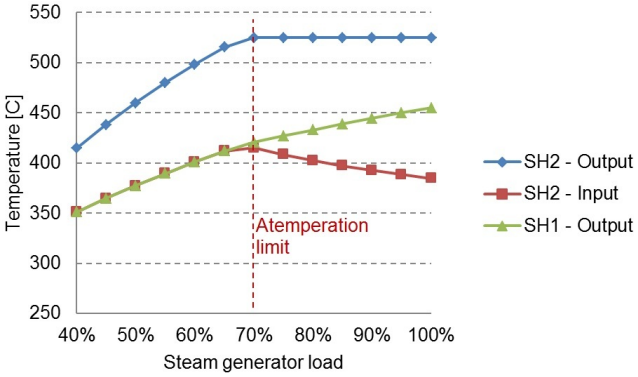

Figure 31: Base case cogeneration power plant simulation results at off-season operation.

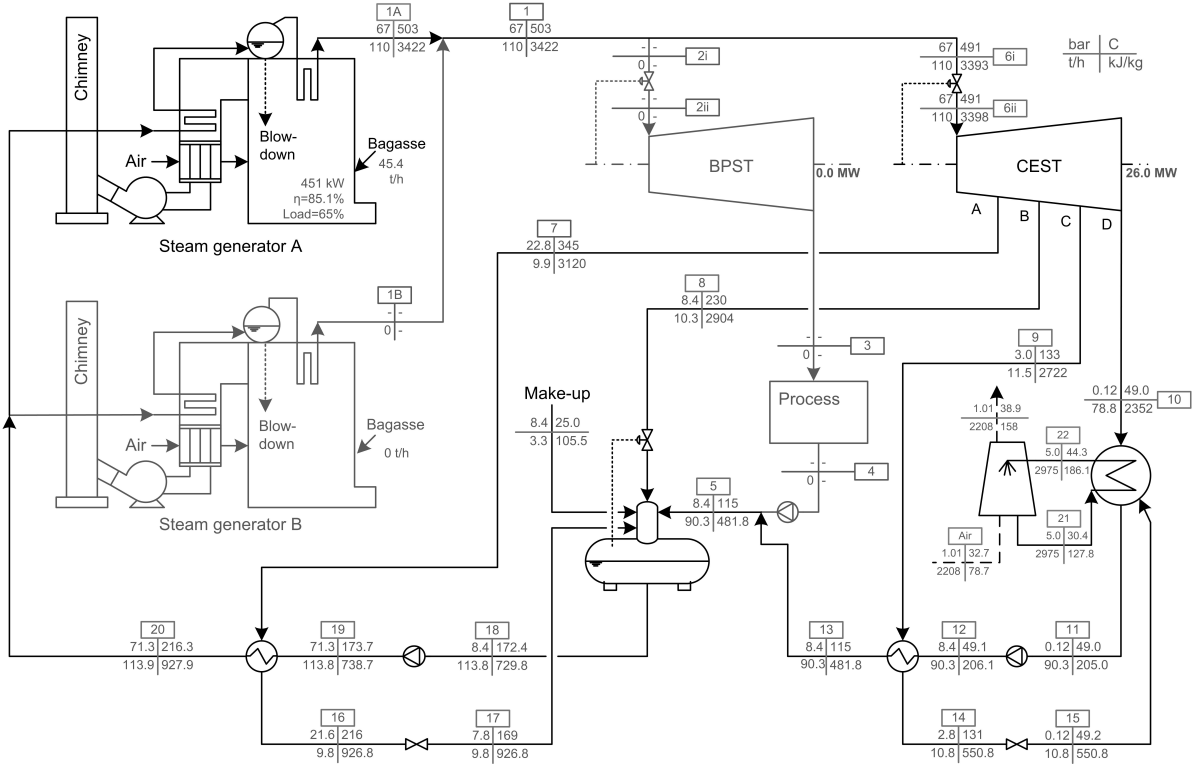

Table 12: Bagasse mass flow rate and electric power production for off-season operation at peak summer weather condition.

Parameter	Unit	Value
Produced bagasse	t/h	-
Burned bagasse	t/h	45.4
Stored bagasse	t/h	-
BPST gross output	MW	-
CEST gross output	MW	26.0
Net electricity production	MW	25.2
Auxiliary electricity consumption	MW	0.8
Process electricity consumption	MW	-
Process heat consumption	MW	-
Net electricity exported to the grid	MW	25.2

6.4 HARVEST SIMULATION

A simulation for all harvest period was performed keeping the net electric power exported to the grid equal to the reference condition (45.5 MW) and respecting ambient fluctuations - results are presented at Table 13. The required time to crush 3 Mt of sugarcane was equal to 5000 hours, when 750,000 t of bagasse was produced, 710,435 t of bagasse was burned (94.7 % of total) and 227,660 MWh was exported to the grid. The operation of plant started at 1st April and according to the operating days identification (Section 5.8) it was finished at 8th December. The total harvest period was 6032 hours, what represented a capacity factor of 82.9 %. This result is in accordance with the capacity factor of sugarcane cogeneration plants located in the Center-South region of Brazil that normally ranges from 80 % to 85 % (BRESSAN; ANDRADE, 2013; BRESSAN; ANDRADE, 2012).

The bagasse consumption profile along harvest is presented in Figure 32. The operation of power plant was interrupted in rainy and in drying days. During operating days it was considered that plant operated at full load milling 600 t/h of sugarcane. The small fluctuations in burned bagasse mass flow rate were due to weather conditions variation and imposed constant net electric power exportation to the grid when plant was under operation.

The cogeneration power plant described in this chapter is considered in Chapter 7 in order to study the hybridization feasibility with parabolic trough collectors. The same base case power plant was considered in the develop-

ment of iNOPA cooperation project in which additional integration layouts were tested based on linear Fresnel and central tower CSP technologies. All integration layouts considered are presented in Chapter 3, while the iNOPA project results are summarized in Appendix E.

Table 13: Base case cycle managed bagasse amount and electricity generation during harvest period.

Parameter	Unit	Value (5000 h)
Produced bagasse	t	750,000
Burned bagasse	t	710,435
Stored bagasse	t	39,565
BPST gross output	MWh	211,256
CEST gross output	MWh	112,510
Net electricity production	MWh	311,660
Auxiliary electricity consumption	MWh	12,106
Process electricity consumption	MWh	84,000
Process heat consumption	MWh	691,099
Net electricity exported to the grid	MWh	227,660

Figure 32: Bagasse consumption profile during harvest operation.

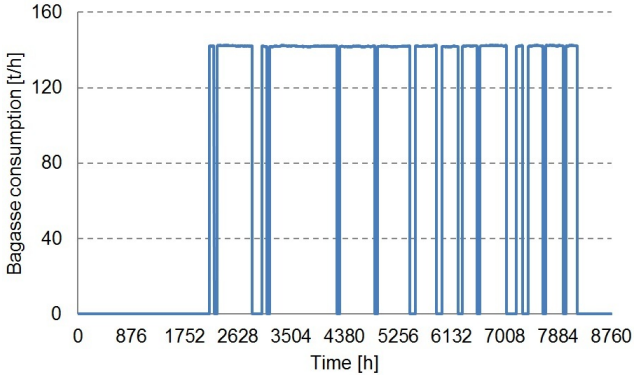

7 HYBRID LAYOUTS

Two integration layouts of cogeneration cycle and parabolic trough solar field were proposed in order to attend the objectives of this work. The general assumptions adopted for solar field sizing, simulation and for economic analysis are presented in Section 7.1. The results for solar feedwater heating are presented in Section 7.2, while the results for solar saturated steam generation are presented in Section 7.3. In both cases the solar-aided operation strategy was implemented as follows:

- Harvest operation: the solar field provided bagasse economy. The amount of economized bagasse was stored to be used during off-season period extending the operation of the power plant;
- Off-season operation: the power plant was operated with one steam generator at 65 % load (110 t/h of SH steam) and back-pressure turbine (BPST) turned off. The hybrid operation of cogeneration cycle was not performed during the off-season period in order to avoid the additional reduction of steam generator's load below 65 % (110 t/h steam).

Additional integration layouts were evaluated under the scope of the iNOPA project developed in cooperation with the University of Duisburg-Essen. The description of evaluated cases is presented in Section 3.2, while the results are summarized in Appendix E.

7.1 GENERAL ASSUMPTIONS

The general assumptions adopted for parabolic trough solar field sizing and simulation are presented in Table 14. The LS-2 collector assemblies equiped with the Luz cermet heat collector elements were considered for simulations once a comprehensive performance data set of these components is available in the literature. Regarding the heat loss modeling in HCE evacuated tubes, the model proposed by Burkholder and Kutscher (2009) and described in Section 4.6.1 was used. The commercial Therminol VP-1 heat transfer fluid is widely used in trough plants around the world and its thermophysical and transport properties are provided by the manufacturer (see Annex A). The design point irradiance, ambient dry bulb temperature and wind velocity were necessary in order to perform the solar field sizing. The procedure implemented to define these reference conditions for the region of Campo Grande -

MS are presented in Appendix C. The solar field electric power consumption was estimated based on the required power for HTF pumping. The tracking system parasitic consumption was here assigned as negligible. Finally, the values of degradation parameters reported by Forristall (2003) were adopted. The cleanliness factors depend on the cleaning strategy implemented in solar field. Normally the whole solar field might be cleaned once or twice a week depending on ambient and soil conditions.

Table 14: General assumptions adopted for solar field sizing and simulation.

Parameters	Unit	Adopted assumption
Solar collector assemblies[a]	-	LS-2
Heat collector elements[a,†]	-	Luz cermet, vacuum
Heat transfer fluid[b]	-	Therminol VP-1
Space between rows, d	m	15 (north-south orientation)
Design point irradiance[‡], $G_{bn,ref}$	W/m^2	953 (solar noon, 23rd Sep)
Design point ambient temp.[‡], $T_{amb,ref}$	^{o}C	28 (DB)
Design point wind velocity[‡], $V_{w,ref}$	m/s	9.5
Solar field pressure drop[c,♯], Δp_{ref}	bar	10
Oil pumping efficiency[d,♮], $\eta_{p,ref}$	-	0.6
SCE cleanliness[e], $f_{cl,sce}$	-	0.95
HCE cleanliness[e], $f_{cl,hce}$	-	0.98
Tracking error[e], f_{trk}	-	0.99
Additional degradation[e], f_{add}	-	0.96

Sources: [a](DUDLEY, 1994); [b](SOLUTIA, 2014); [c](MANZOLINI *et al.*, 2011b); [d](LIPPKE, 1995); [e](FORRISTALL, 2003).

[†]Burkholder and Kutscher (2009) heat loss modeling; [‡]See Appendix C.

[♯]Pressure drop at 5 kg/s HTF mass flow rate in loops.

[♮]Pumping system designed for design point HTF mass flow.

The adopted assumptions regarding economic analysis are presented in Table 15. The capital costs were defined based on quotations performed with parabolic trough solar field suppliers and on literature data. The cost of land area was also accounted as part of initial investment. The annual O&M costs were here assigned to the material replacement costs reported by Morin *et al.* (2012) for a parabolic trough solar field and on paying employees to operate solar field and to execute the maintenance services. In all simulations it was considered that five employees were necessary in addition to the biomass power plant staff to perform solar field operation and maintenance.

The modelling and simulation of solar field components was performed using the software Matlab®.

Table 15: Assumptions adopted for economic analysis.

Parameters	Unit	Adopted assumption
Solar field†	U$/m^2	310
Economizer^{a}	U$/kWth	27
Evaporator^{a}	U$/kWth	47
Balance of plant†	U$/m^2	75
Procurement and construction†	U$	10 % of *DC*
Engineering and management†,‡	U$	10 % of *DC*
Site improvements^{b}	U$/ha	250,000
Land investment$^{\diamondsuit}$	U$/ha	20,000
Material replacement^{c}	U$/year	1 % of *DC*
Employee charge$^{\diamondsuit}$	U$/year	40,000 %
Interest rate, r	-	8 %
Life time of plant, lt	years	25

Sources: ^{a}(MANZOLINI *et al.*, 2011b); ^{b}(TURCHI, 2010); ^{c}(MORIN *et al.*, 2012).
†Quoted cost; ‡Considered not dependent on solar field area; $^{\diamondsuit}$Estimated cost.

7.2 RESULTS FOR SOLAR FEEDWATER HEATING

7.2.1 Solar integration at design point condition

The main results of solar feedwater heating at design point operation are presented in Figure 33. Feedwater at point 19i was pre-heated using an oil-water heat exchanger before the stream entered the closed feedwater heater at point 19ii. The pressure drop across the oil-water heat exchanger was negligible. The solar field was sized to pre-heat feedwater to 200 ^{o}C in order to displace CEST high pressure extraction at design point irradiance during harvest operation (Solar Multiple (SM) equal one, SM=1.00). In this regard, it was proposed the installation of 28,260 m^2 aperture area in a land area of 12 ha. The layout of solar field consisted of 120 LS-2 assemblies disposed in 15 loops.

Due to solar heat load, the CEST turbine extraction mass flow rate at point 7 was reduced from 25.5 t/h (see Figure 25 of Section 6.2) to 7.7 t/h (-70 %). It was not totally displaced as the steam extraction implemented in turbine was not controlled and its flow was determined by the heat exchanger purge that released the condensate formed as heat was transferred to feedwater. Due to this aspect the final feedwater temperature in point 20 was equal to 212 ^{o}C.

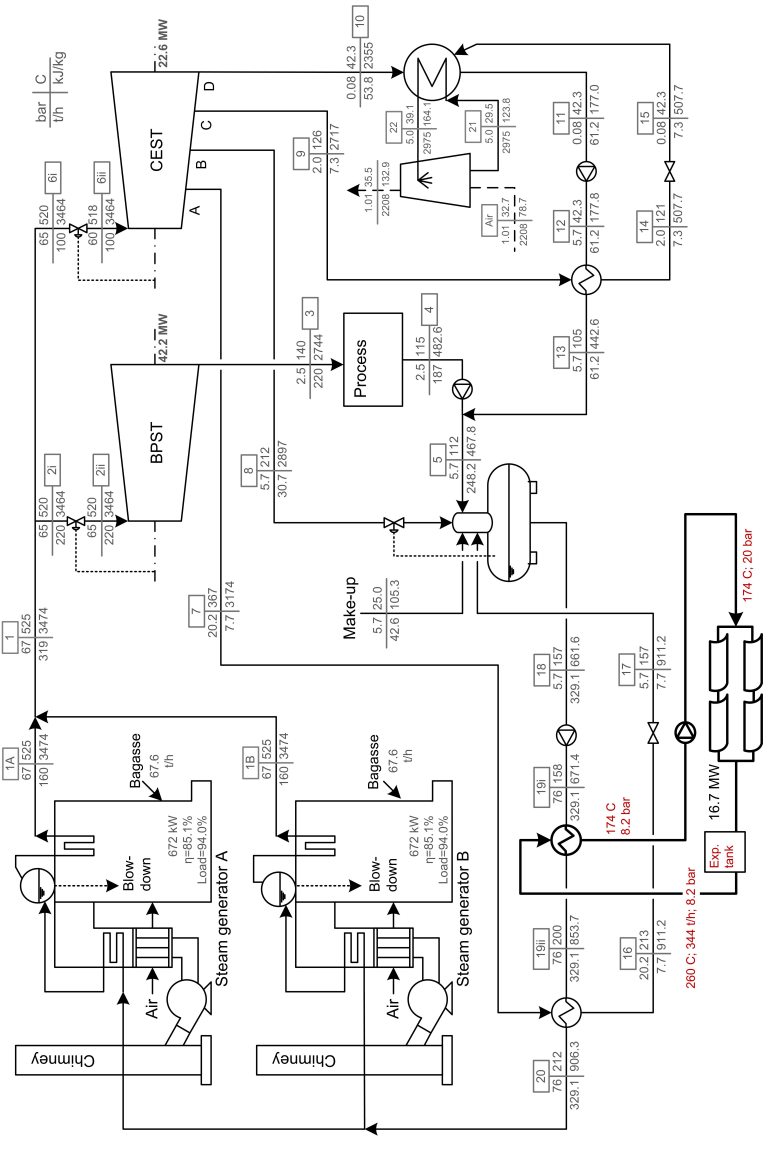

Figure 33: Solar-aided (solar feedwater heating) cogeneration plant simulation results at design point operation.

Results related to the solar field performance at design point are presented in Table 16. The number of solar collector assemblies per loop was configured to provide oil mass flow rate in loops close to 25 t/h as it is usual for 70 mm inner diameter heat collector elements (BURKHOLDER; KUTSCHER, 2009). The solar field delivered heat was 16.7 MW with 61.9 % thermal efficiency. The electric power consumption was 0.2 MW as required by pumping 344 t/h of thermal oil across solar field. The bagasse consumption was reduced to 135.3 t/h (-5.1 %), keeping the same net electric power exportation to the grid identified for base case.

Table 16: Solar field (solar feedwater heating) results at design point operation.

Parameter	Unit	Value
Solar field aperture area, A_{sf}	m^2	28,260
Land area, A_{land}	ha	12
Solar field delivered heat, $\dot{Q}_{av,ref}$	MW	16.7
Solar field thermal efficiency, $\eta_{sf,ref}$	%	61.9
Oil pump parasitic consumption, $\dot{W}_{p,ref}$	MW	0.2
Oil temperature rise in loops	^{o}C/m	0.2
Oil mass flow in loops, $\dot{m}_{htf,ref}/N_{loop}$	t/h	22.2
Burned bagasse, $\dot{m}_b$	t/h	135.3 (-5.1 %)

No major impact in steam generators performance was found due to solar-aided feedwater heating. The load of these components was reduced to 94 % with a weak reduction in thermal efficiency from 85.2 % (base case) to 85.1 %.

The CEST turbine operation results under: a) base case harvest; b) off-season and c) solar-aided harvest (16.7 MW solar thermal load) are presented at Figure 34 for design point condition. As the mass flow rate of steam delivered to the last stages of turbine was increased due to solar heat load, the condensing temperature was ranged from 40.4 ^{o}C to 42.3 ^{o}C with air and cooling water mass flow rates kept at maximum capacity. For off-season operation, even with no solar integration, the condensing temperature was equal to 50.0 ^{o}C once exhaust steam mass flow rate was higher (78.8 t/h) when compared to harvest condition. In this regard, solar integration didn't require the retrofit of cooling system which was already designed to meet off-season operation. It is also important to point out that steam extraction to deaerator was increased in 20 % due to solar heat input. In this work it was considered that deaeration system was able to handle with additional thermal load, but the capacity of this component might be addressed when designing solar field in order to avoid its malfunction. Finally, minor isentropic efficiency

variation was predicted due to solar integration.

Figure 34: CEST turbine operation results for design point peak summer weather condition under: a) base case harvest operation; b) off-season operation and c) solar-aided harvest operation (16.7 MW solar thermal load).

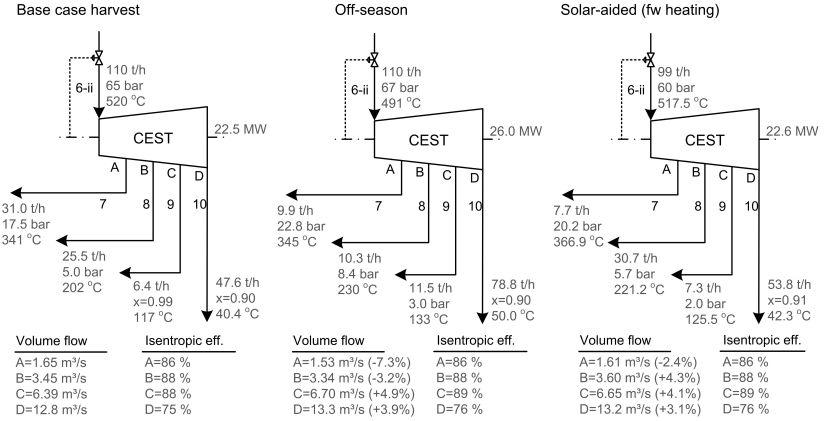

7.2.2 Annual analysis

The hybrid power plant operation along harvest as well as the extended off-season operation are evaluated in this section. The first result consists on the economized bagasse mass flow rate profile along harvest operating days, which is presented in Figure 35. Peak fuel economy of around 7 t/h was obtained in the beginning and in the end of harvest, while during winter (June, July and August) it was minimized due to higher optical and thermal losses. The same general pattern was described by Peng *et al.* (2014) for the off-design operation of a parabolic trough solar field integrated into a conventional coal fired plant. According to authors, the optical efficiency of solar field could be improved in winter by changing the orientation of collectors from North-South to East-West. This suggestion was also tested in this work. Nevertheless, the lower efficiency during summer caused by orientation change didn't represent a net annual gain in terms of bagasse economy. The total bagasse economy under East-West orientation was 36 % lower in comparison with the initially proposed North-South orientation.

As it can be seen in Table 17, the economized amount of bagasse was

5,594 t, what turned possible generating additional 3,135 MWh of electricity during off-season (additional 1.4 % electricity exportation to the grid when compared to base case). Nevertheless, the solar field was out of operation during stopped drying days in harvest and during off-season and, as a consequence, the solar-to-electricity efficiency of hybrid system was reduced to 7.4 % - what is significantly lower when compared to the typical range of 11-16 % obtained in commercial parabolic trough power plants without heat storage (IRENA, 2012). The reduced capacity factor of solar integration contributed to obtain the not attractive LCOE of 619.2 U$/MWh despite the reduced capital cost of solar aided power plants.

Figure 35: Economized bagasse during harvest operating days.

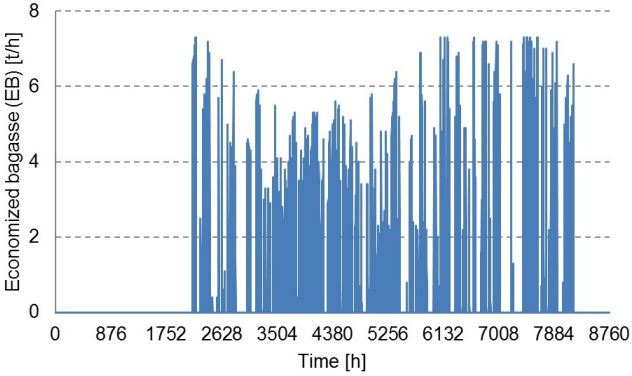

Table 17: Results related to solar aided power plant (solar feedwater heating).

Parameter	Unit	Value
Fuel economy, EB	t	5,594
Additional electricity, AE	MWh	3,135 (+1.4 %)
Solar field efficiency, η_{sf}	%	29.8
Solar-to-electricity efficiency, η_{se}	%	7.4
Capital costs, CC	10^3U$	17,379.2
Annual costs	10^3U$	313.3
Solar LCOE	U$/MWh	619.2

It is important to notice that the operation strategy here implemented could be also modified by considering the use of economized bagasse due to solar hybridization during the otherwise stopped drying days. In this regard, the economized amount of bagasse would be consumed during harvest non-operating days instead of extending the operation of power plant during off-

season. This strategy would also reduce the stored bagasse volume along the harvest. The calculated additional electricity production, nevertheless, would be the same and the operation strategy proposed in Section 13 was here adopted to simplify the implementation of simulation procedures.

7.3 RESULTS FOR SOLAR SATURATED STEAM GENERATION

7.3.1 Solar integration at design point condition

In case of solar saturated steam generation, the parabolic trough solar field was sized to displace fuel consumption (boiler heat load) of both bagasse steam generators during harvest operation of cogeneration cycle. The minimum boiler heat load was defined as the operation condition in which attemperation mass flow rate was turned zero (the limit in which it was possible to maintain SH steam temperature equal to 525 ^{o}C). The main results related to the part load operation of one bagasse steam generator are presented in Figure 36 for harvest peak summer design point condition. The results of both steam generators are the same - the simulation was performed for one system and replicated to the other. It is important to emphasize that the part load efficiency of steam generators here correspond to the use of the base case unburned carbon profile (see Figure 27 of Section 6.3). A sensitive analysis regarding the use of the alternative unburned carbon profiles is performed in Section 7.4.1.

As it can be seen in Figure 36, 28.1 t/h of feedwater at 200 ^{o}C was diverted to the oil-water heat exchangers in order saturated steam (x=1) to be generated. The saturated steam was introduced back at 288 ^{o}C in bagasse steam generation system to be superheated to the final temperature of 525 ^{o}C. Notice that economizer and boiler were both operated in reduced load, but superheaters were operated close to nominal full load. One concern was initially related to the reduction of ECO feedwater mass flow rate and the possibility of water evaporation. This would lead to hot spots in bundle of tubes and failure of heat exchanger (see Appendix D where an alternative design is presented). Nevertheless, as boiler load was reduced, flue gas temperature was also reduced and, as a consequence, the final feedwater temperature got lower when compared to the base case operation. It was proposed the installation of 54,636 m^2 aperture area in a land area of 23 ha (Solar Multiple equal one, SM=1.00). The layout of solar field consisted of 232 LS-2 assemblies disposed in 29 loops.

Figure 36: Solar-aided bagasse steam generator simulation results at design point operation.

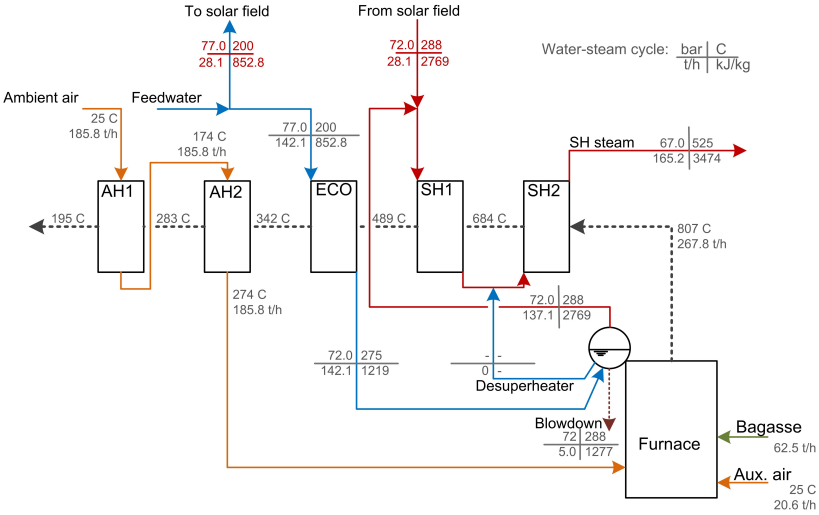

Solar field simulation results based on harvest peak summer design point condition and layout of heat exchangers (economizer and boiler) are presented in Figure 37. Feedwater from both bagasse steam generators was introduced in oil-water economizer where it was pre-heated to 267 ^{o}C. After that, it was evaporated in boiler (a recirculating system with a steam/water separator drum). Thermal oil was heated in solar field to 370 ^{o}C. First it was cooled to 297 ^{o}C in boiler and finally to 282 ^{o}C in economizer.

Figure 37: Solar field (saturated steam generation) simulation results at design point operation.

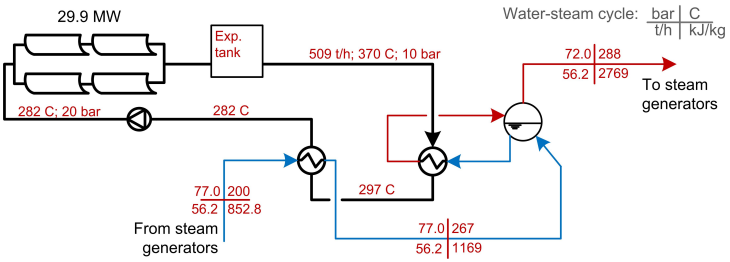

The results related to the solar field performance at design point are

presented in Table 18. The number of solar collector assemblies per loop was configured to provide oil mass flow rate in loops close to 25 t/h as it is usual for 70 mm inner diameter heat collector elements (BURKHOLDER; KUTSCHER, 2009). The solar field delivered heat was 29.9 MW with 57.4 % thermal efficiency. Observe that it was 7 % lower in comparison with solar field efficiency of feedwater heating scheme due to the increased thermal oil average temperature. The electric power consumption was 0.3 MW as required by pumping 509 t/h of thermal oil across solar field. The bagasse consumption was reduced to 125.3 t/h (-12.1 %), keeping the same net electric power exportation to the grid identified for base case.

Table 18: Solar field (saturated steam generation) simulation results at design point operation.

Parameter	Unit	Value
Solar field aperture area, A_{sf}	m^2	54,636
Land area, A_{land}	ha	23
Solar field delivered heat, $\dot{Q}_{av,ref}$	MW	29.9
Solar field thermal efficiency, $\eta_{sf,ref}$	%	57.4
Oil pump parasitic consumption, $\dot{W}_{p,ref}$	MW	0.3
Oil temperature rise in loops	^{o}C/m	0.2
Oil mass flow in loops, $\dot{m}_{htf,ref}/N_{loop}$	t/h	17.6
Burned bagasse, $\dot{m}_b$	t/h	125.3 (-12.1 %)

7.3.2 Annual analysis

Results related to annual simulation of solar saturated steam generation layout are presented in Table 19. The economized amount of bagasse was 11,565 t, what turned possible generating additional 6,482 MWh of electricity during off-season (additional 2.8 % electricity exportation to the grid when compared to base case). Annual solar-to-electricity conversion efficiency of hybrid system was equal to 7.9 %, which was higher if compared to the feedwater heating scheme even with higher thermal oil average temperature. Nevertheless, once again the solar field was out of operation during stopped drying days in harvest and during off-season and, as a consequence, the solar-to-electricity conversion efficiency of hybrid system was significantly lower when compared to the typical range of 11-16 % obtained for commercial parabolic trough power plants without heat storage (IRENA, 2012). The redu-

ced capacity factor of solar integration contributed to obtain the not attractive LCOE value of 558.5 U$/MWh.

Table 19: Results related to solar aided power plant (saturated steam generation).

Parameter	Unit	Value
Fuel economy, EB	t	11,565
Additional electricity, AE	MWh	6,482 (+2.8 %)
Solar field efficiency, η_{sf}	%	24.1
Solar-to-electricity efficiency, η_{se}	%	7.9
Capital costs, CC	10^3U$	34,124.7
Annual costs	10^3U$	423.4
Solar LCOE	U$/MWh	558.5

7.4 SENSITIVE ANALYSIS

In this section it is presented a sensitive analysis considering important input parameters that influence the technical and economical feasibility of CSP hybridization layouts.

7.4.1 Part load efficiency of steam generators

The results related to the additional electricity AE [MWh] and LCOE [U$/MWh] for solar feedwater heating and saturated steam generation layouts considering the distinct tests performed regarding unburned carbon content at part load (see Section 6.3) are presented in Figure 38. In opposition to the base case scenario, it was considered that unburned carbon content in residues was moderately increased (test 2), considered constant (test 3) and reduced (test 4) at part load.

In case of solar feedwater heating, AE [MWh] was increased in +7 % comparing test 4 with base case, while LCOE [U$/MWh] was reduced in 7 % from 619 (base case) to 579 U$/MWh (test 4). For saturated steam generation similar results were observed. AE [MWh] was increased in 7 % comparing test 4 with base case, while LCOE [U$/MWh] was reduced in 6 % from 559 (base case) to 523 U$/MWh (test 4).

Figure 38: Influence of steam generator's part load efficiency on solar electricity LCOE.

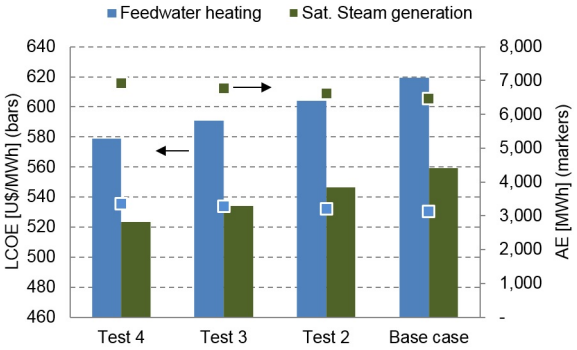

7.4.2 Economic assumptions

The economic assumptions (quotations, operational costs and the interest rate related to the economic scenario of a certain country and market) might carry uncertainties and change over time. It is expected that capital costs will decrease in next years as a consequence of the learning curve of CSP technology (IRENA, 2012). Thus, capital costs, operational costs and interest rate were changed in ± 25 % around their central values in order to identify their influence in LCOE [U$/MWh] of additional solar electricity generated due to hybridization.

As it can be seen in Figure 39, in both integration layouts LCOE was more sensitive to capital costs variation. It was here considered the variation of costs related to solar field components, balance of plant and heat exchangers. In case of solar feedwater heating, it ranged from 509 to 730 U$/MWh as CAPEX ranged from 14.0 to 20.8 millions of dollars. For saturated steam generation, LCOE ranged from 453 to 664 U$/MWh as CAPEX ranged from 27.4 to 40.8 millions of dollars. Solar thermal plants are yet cost intensive. If a CAPEX reduction of 40 % is considered, as it is expected by IRENA (2012) for the next 10 years, LCOE would be reduced to 440 U$/MWh (-29 %) and 390 U$/MWh (-30 %) for feedwater heating and saturated steam generation, respectively.

Regarding interest rate, it is higher if risks involved are higher. Investments in regulated electricity markets, for instance, might have lower risks in comparison with investments in open and competitive markets. A discussion related to this topic is performed in IEA (2010). Thus, it was here conside-

Figure 39: Influence of economic assumptions on solar electricity LCOE.

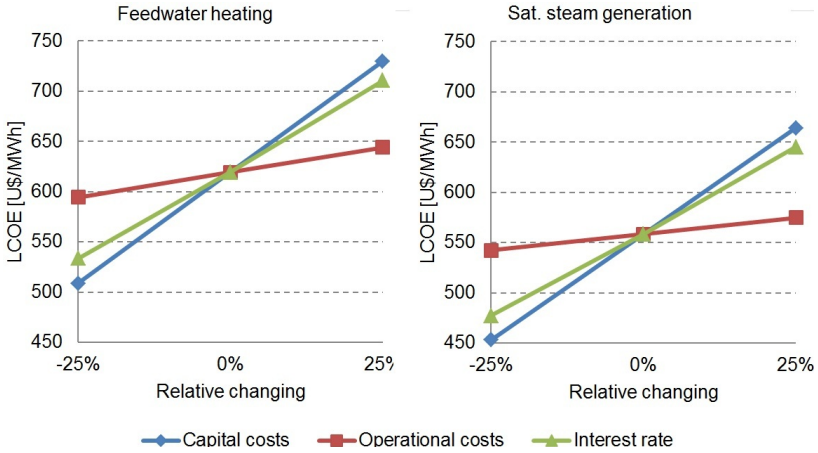

red a range of interest rate values. As it was ranged from 6 to 10 %, LCOE was ranged from 534 to 711 U$/MWh for solar feedwater heating and 477 to 645 U$/MWh for solar saturated steam generation.

Finally, LCOE was less sensitive to the variation of operational costs. It was here considered the variation of employee's charge (for operation and maintenance) and price of materials for replacement. In fact, operational costs of CSP can be considered low as there are no costs related to fuel purchasing. In case of solar feedwater heating, varying annual costs from 235.0 to 391.6 thousand of dollars per year leaded to an LCOE increase from 594 to 644 U$/MWh. In case of saturated steam generation, varying annual costs from 317.6 to 529.3 thousand of dollars per year leaded to an LCOE increase from 542 to 575 U$/MWh.

7.4.3 Solar multiple sensitive analysis

The solar multiple (SM) represents the ratio at which the solar field aperture area is modified in comparison with the design point aperture area calculated during design phase. The SM=1.10 means that aperture area is increased by 10 % in comparison with design point. As it can be seen in Figure 40, once solar field area was increased, the electricity produced due to hybridization was increased asymptotically. There were additional hours during harvest in which solar field was operated in maximum heat load capacity.

In the other side, there was additional hours in which solar field was defocused and solar thermal energy was dumped. Solar field defocusing consisted in not using available capacity of equipment. Regarding economic analysis, engineering and management costs and employees charge were considered constant and equal to the SM=1.00 case. These costs are weakly correlated on solar field size for the considered SM range evaluated in this work. The LCOE, as a consequence, was changed as a function of solar field area and the most feasible design was found. It was identified for solar feedwater heating approach that optimum solar field SM in accordance with LCOE was between 1.10 and 1.20 reaching LCOE of 617 U$/MWh. In case of solar saturated steam generation the optimum LCOE was equal to 558 U$/MWh for SM=1.00. The optimum SM depends on the economic assumptions and technical aspects of CSP plant under consideration. Results here presented are only valid for the specific scenario described in this work.

Figure 40: Solar equivalent electricity and LCOE for different solar multiples.

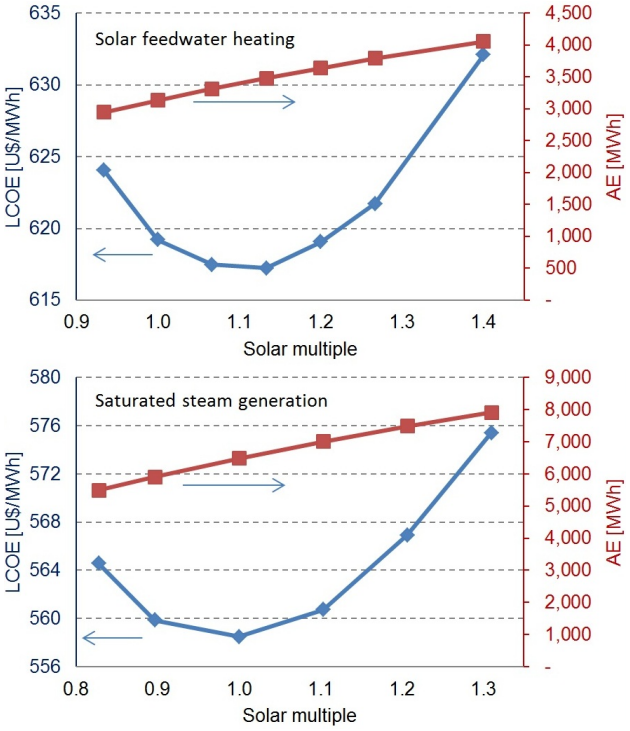

7.4.4 DNI incidence and operation period

The analysis of bagasse cogeneration plants hybridization with CSP was focused in this work to the city of Campo Grande - MS. According to the TMY data used in simulations, the DNI incidence during harvest was 1034 kWh/m^2-harvest, corresponding to 69 % of total annual DNI incidence of 1502 kWh/m^2-year. In this regard, at least 31 % of solar DNI was not used in evaluated layouts once solar field was out of operation during off-season.

In order to evaluate the influence of DNI incidence and operation period on the economic feasibility of hybridization layouts, two tests were performed and the results are presented Figure 41. As reported in Solargis (2014), the DNI incidence in the south of Goias state can reach 2000 kWh/m^2-year. Under this more favorable DNI incidence condition, it was found that AE could be increased to 4,170 MWh (at 466 U$/MWh) in case of solar feedwater heating and to 8,621 MWh (at 420 U$/MWh) in case of solar saturated steam generation.

The second test consisted on the straightforward estimation of AE [MWh] and LCOE [U$/MWh] considering the use of 1502 kWh/m^2-year by hypothetical CSP plants with the same performance of both solar feedwater heating and solar saturated steam generation layouts. Under this condition AE would reach 4,546 MWh (at 427 U$/MWh) in case of solar feedwater heating and 9,399 MWh (at 385 U$/MWh) in case of solar saturated steam generation. Thus, together with selecting a site with as high as possible DNI incidence, improving the capacity factor of solar field is also a key factor for improving economic feasibility of hybridization layout.

Figure 41: Influence DNI and operation period on solar electricity LCOE.

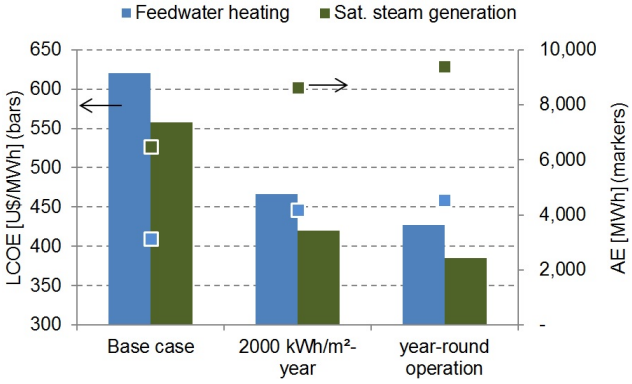

7.5 SUMMARY AND OUTLOOK

Both hybrid scenarios studied in this work provided relatively high cost electricity - above the range of 210-370 U$/MWh reached nowadays in commercial CSP plants (IRENA, 2015; IRENA, 2012). In Figure 42 the LCOE [U$/MWh] results here obtained are compared with a CSP parabolic trough plant located in US and with conventional technologies applied in Brazil (IEA, 2010)[1]. All conventional plants LCOE results were limited to around 100 U$/MWh. The parabolic trough plant provided LCOE ranging from 200 to 370 U$/MWh. Thus, it is clear that there is yet a wide room for cost reductions.

Figure 42: Comparison of LCOE [2014 U$/MWh] for distinct technologies.

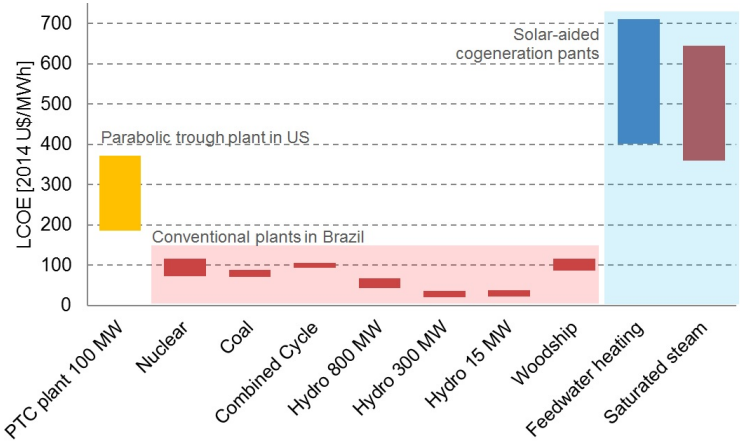

Source: adapted from IEA (2010).

Solar saturated steam generation provided a higher conversion efficiency and economic feasibility in comparison with solar feedwater heating. Nevertheless, the complexity of hybridization might be further evaluated. It was necessary to modify bagasse steam generator's circuit for solar saturated steam generation, while feedwater pre-heating was performed considering just the integration of an additional oil-water heat exchanger before biomass system's inlet. This preliminary evaluation, together with iNOPA project re-

[1]The IEA report was based on data provided by electricity companies. The ranges of LCOE were due to 5 and 10 % interest rates. The scenarios related to this work were based in pessimistic (1502 kWh/m^2-year; r=10%) and optimistic (2000 kWh/m^2-year; r=5%) scenarios.

sults (see Appendix E), was important to identify general aspects of distinct integration options and further work might be implemented in the experimental field.

An additional aspect that might be studied in future works consists on the evaluation of the dynamic heavior of bagasse steam generators once solar heat is integrated in steam cycle. In this work, the simulation of bagasse steam generators was perfored at steady-state. In this regard, it was considered that these components were able to absorb the fluctuations of solar field delivered heat by changing the bagasse feeding rate once it was necessary.

The operation of a cost intensive parabolic trough solar field installation limited to the harvest period can be considered the main drawback of proposed strategies. Providing year-round operation turns possible to increase the solar electricity generation and to improve the economic feasibility of investment. See in Appendix E that LCOE of additional electricity generated due to solar hybridization was reduced to 220 U$/MWh in case of using a central tower solar field to produce superheated steam in parallel with bagasse steam generators. During periods of no bagasse availability, CEST turbine was operated in a solar-only mode. This option was considered in iNOPA project but, again, the complexity of this layout might be further evaluated together with the equipment suppliers.

Considering the current context of the Brazilian electricity sector and the results presented in this study, it can be indicated that the hybridization methods here proposed are not economically feasible. In the last auctions of the controlled energy market performed in 2014, the electricity produced by thermal power plants (natural gas; coal; biomass in general) was contracted on the average price of 70 U$/MWh. In the same period, onshore wind electricity was contracted on the average price of 45 U$/MWh. Solar energy contracts were performed exclusively for photovoltaics in an average price of 87 U$/MWh (EMPRESA DE PESQUISA ENERGéTICA (EPE), 2015). The inclusion of CSP in the Brazilian energy matrix would require today alternative subsidized contracts independently on CSP plant configuration. It should be kept in mind, however, that there is yet great room for reducing CSP investment and O&M costs. Regarding parabolic trough technology, it is estimated that in 10 years the capital costs will decrease by 40 % (IRENA, 2012). Thus, despite the limitations related to the specific cases proposed in this work, further studies might be developed given the local potential of solar and biomass resources. Solar thermal energy can complement the biomass availability in the sugarcane sector and the rational use of this resource can be promoted.

8 CONCLUSIONS

Concentrated solar power hybridization of sugarcane bagasse cogeneration plants equipped with BPST and CEST turned possible to improve the annual electricity output of these plants by maximizing their capacity factor while providing additional off-season operation. This represented a gain due to the use of existing infrastructure that otherwise would stay out of operation part of the year when no sugarcane was available.

Solar feedwater heating has the advantage of requiring minimal modifications on the original plant and investment costs related to solar integration are reduced. This is also true for the hybridization of cogeneration plants equipped with BPST and CEST. Nevertheless, solar-only operation is not possible under this integration concept. In this work, the cogeneration plant was turned off in sunny drying days of harvest and off-season. In this regard, the reduced capacity factor of solar field contributed to the achievement of the high LCOE range of 401-710 U$/MWh of additional electricity produced due to hybridization. This electricity price was above the range of 210-370 U$/MWh reached nowadays in commercial CSP power plants (IRENA, 2015; IRENA, 2012). Finally, the off-design operation of power plant components might be evaluated during design phase. For the presented case study, steam mass flow displaced to the last stage of CEST was increased due to solar heat load, but feasible operation was achieved as cooling system was designed to meet off-season operation. Deaerator thermal load was also increased by 20 %. Thus, the maximum capacity of this system might be addressed during design in order to avoid its malfunction.

Saturated steam production in parallel with bagasse steam generators turned possible to improve both the solar share and solar-to-electricity conversion efficiency in comparison with solar feedwater heating (under specific characteristics of presented case study). An important negative aspect, nevertheless, resides in the complexity inherent to the retrofit and operation of biomass steam generators and heat imbalances that might be observed. This preliminary evaluation was here provided to identify general aspects of this integration option and further works might be implemented in the experimental field. This integration has also the incapability of solar-only operation. In this regard, the reduced capacity factor of solar field contributed to the achievement of the high LCOE range of 359-645 U$/MWh of additional electricity produced due to hybridization - again above the range of 210-370 U$/MWh reached nowadays in commercial CSP power plants.

In order to improve economic feasibility of CSP hybridization with su-

garcane bagasse, year-round operation is necessary. Other integration layouts are possible and might be evaluated. As an example, superheated steam generation in parallel with biomass steam generators may have the advantage of higher solar share and solar-only operation during off-season when no biomass is available - see in Appendix E that LCOE of additional electricity generated due to solar hybridization was reduced to 220 U$/MWh when a central tower solar field was used to produce superheated steam in parallel with bagasse steam generators.

Finally, despite the limitations of proposed hybridization methods with parabolic trough concentrators in terms of economic feasibility, an important aspect was identified. Solar energy can be integrated into bagasse power plants in the sugarcane sector. If in one side CSP hybridization with biomass indicates the possibility of a more reliable power supply, solar thermal load can also lead to the rational use of bagasse availability by improving the exportation of electricity to the grid.

REFERENCES

AALBORG CSP. **Aalborg CSP - your green thermal energy pertner**. 2015. Available in: <http://www.aalborgcsp.com/>.

ALVES, M. **Estudo de sistemas de cogeração em usinas de açúcar e álcool, com utilização do bagaço e palha da cana**. Master thesis (Master) — Universidade Estadual de Campinas (UNICAMP), 2011.

ANEEL. **Banco de Informações de Geração (BIG)**. June 2015. Available in: <http://www.aneel.gov.br/aplicacoes/capacidadebrasil/OperacaoCapacidadeBrasil.asp>.

ANNARATONE, D. **Steam generators: description and design**. [S.l.]: Springer, 2008.

AREVA SOLAR. 2015. Available in: <http://www.areva.com/EN/solar-220-/areva-solar.html>.

ASME PTC 4-2008 Fired steam generators: performance test codes. 2008.

BAKOS, G. C.; PARSA, D. Technoeconomic assessment of an integrated solar combined cycle power plant in greece using line-focus parabolic trough collectors. **Renewable Energy**, v. 60, p. 598–603, 2013.

BAKOS, G. C.; TSECHELIDOU, C. Solar aided power generation of a 300 mw lignite fired power plant combined with line-focus parabolic trough collectors field. **Renewable Energy**, v. 60, p. 540–47, 2013.

BARROSO, J.; BARRERAS, F.; AMAVEDA, H.; LOZANO, A. On the optimization of boiler efficiency using bagasse as fuel. **Fuel**, v. 82, p. 1451–63, 2003.

BAZZO, E. **Geração de vapor**. [S.l.]: Editora da UFSC, 1995.

BERGMAN, T. L.; LAVINE, A. S.; INCROPERA, F. P.; DEWITT, D. P. **Fundamentals of Heat and Mass Transfer**. 6th edition. ed. [S.l.]: John Wiley & Sons, Inc., 2008.

BHATTACHARJEE, S.; DEY, A. Techno-economic performance evaluation of grid integrated pv-biomass hybrid power generation for rice mill. **Sustainable Energy Technologies and Assessments**, v. 7, p. 6–16, 2014.

BNDES; CGEE. **Bioetanol de Cana-de-Acucar: Energia para o Desenvolvimento Sustentável**. [S.l.]: BNDES and, 2008.

BOE. **Boletin Oficial del Estado / Orden IET/3586/2011**. [S.l.], 2011.

BRESSAN, A.; ANDRADE, R. A. de. **Perfil do setor do açúcar e do álcool no Brasil: Edição para a safra 2010-2011**. [S.l.], 2013.

BRESSAN Ângelo; ANDRADE, R. A. de. **Perfil do setor do açúcar e do álcool no Brasil: Edição para a safra 2009-2010**. [S.l.], 2012.

BUONOMANO, A.; CALISE, F.; PALOMBO, A.; VICIDOMINI, M. Energy and economic analysis of geothermal-solar trigeneration systems: A case study for a hotel building in ischia. **Applied Energy**, v. 138, p. 224–41, 2015.

BURKHOLDER, F.; KUTSCHER, C. **Heat Loss Testing of Schott's 2008 PTR70 Parabolic Trough Receiver**. [S.l.], 2009.

COMPANHIA NACIONAL DE ABASTECIMENTO (CONAB). **Series Historicas - Cana-de-Acucar**. April 2015.

CONAMA - CONSELHO NACIONAL DO MEIO AMBIENTE. **RESOLUÇÃO CONAMA no 382, de 26 de dezembro de 2006**. 2006.

DUDLEY, V. E. **Test results - SEGS LS-2 Solar Collector**. [S.l.], 1994.

DUDLEY, V. E. **Test Results - Industrial Solar Technology - Parabolic Trough Solar Collector**. [S.l.], 1995.

DUFFIE, J. A.; BECKMAN, W. A. **Solar engineering of thermal processes**. [S.l.]: John Wiley & Sons, Inc., 1980.

EMPRESA DE PESQUISA ENERGéTICA (EPE). **Leilões de energia**. March 2015. Available in: <http://www.epe.gov.br/leiloes>.

ENSINAS, A. V. **Integração térmica e integralção termoeconômica aplicadas ao processo industrial de produção de açúcar e etanol a partir da cana-de acucar**. Phd thesis (Phd) — Universidade Estadual de Campinas, 2008.

EPIA, E. P. I. A. **Global market outlook for photovoltaics 2014-2018**. [S.l.], 2014.

ESEN, H.; INALLI, M.; ESEN, M. Technoeconomic appraisal of a ground source heat pump system for a heating season in eastern turkey. **Energy Conversion and Management**, v. 47, p. 1281–97, 2006.

FERNáNDEZ-GARCíA, A.; ZARZA, E.; VALENZUELA, L.; PéREZ, M. Parabolic-trough solar collectors and their applications. **Renewable and Sustainable Energy Reviews**, v. 14, p. 1695–721, 2010.

FORRISTALL, R. **Heat Transfer Analysis and Modeling of a Parabolic Trough Solar Receiver Implemented in Engineering Equation Solver**. [S.l.], 2003.

GARCíA-CORTéS, S.; BELLO-GARCíA, A.; ORDóñEZ, C. Estimating intercept factor of a parabolic solar trough collector with new supporting structure using off-the-shelf photogrammetric equipment. **Applied Energy**, v. 92, p. 815–21, 2012.

GIOSTRI, A.; BINOTTI, M.; ASTOLFI, M.; SILVA, P.; MACCHI, E.; MANZOLINI, G. Comparison of different solar plants based on parabolic trough technology. **Energy**, p. 1–16, 2012.

HONG-JUAN, H.; ZHEN-YUE, Y.; YONG-PING, Y.; SI, C.; NA, L.; JUN-JIE, W. Performance evaluation of solar aided feedwater heating of coal-fired power generation (safhcpg) system under different operating conditions. **Applied Energy**, v. 112, p. 710–8, 2013.

HOU, H.; YANG, Y.; HU, E.; SONG, J.; DONG, C.; MAO, J. Evaluation of solar aided biomass power generation systems with parabolic trough field. **Science China Technological Sciences**, v. 54, p. 1455–61, 2011.

IEA. **Projected Costs of Generating Electricity**. [S.l.], 2010.

IPT. **Conservação de Energia na indústria do açúcar e do álcool: manual de recomendações**. [S.l.]: Instituto de Pesquisas Tecnológicas, 1990.

IRENA, I. R. E. A. **Renewable Energy Technologies - cost analysis series - Concentrating Solar Power**. June 2012.

IRENA, I. R. E. A. **Renewable power generation costs in 2014**. January 2015.

JANK, M. S. **O Futuro do Setor Sucroenergético: Ações da UNICA e Cenários**. Novembro 2011. Available in: <http://www.unica.com.br-/multimedia>.

JUEDES, M.; VIGERSKE, S.; TSATSARONIS, G. Optimization in the energy industry energy systems. In: ____. [S.l.]: Springer, 2009. cap. Optimization of the Design and Partial-Load Operation of Power Plants Using Mixed-Integer Nonlinear Programming.

KELLY, B.; KEARNEY, D. **Parabolic Trough Solar System Piping Model**. [S.l.], 2004.

KITTO, J. B.; STULTZ, S. C. (Ed.). **Steam: its generation and use**. [S.l.]: The Babcock and Wilcox Company, 2005.

KOST, C.; MAYER, J.; THOMSEN, J.; HARTMANN, N.; SENKPIEL, C.; PHILIPPS, S.; NOLD, S.; LUDE, S.; SAAD, N.; SCHLEGL, T. **Levelized Cost of Electricity Renewable Energy Technologies**. [S.l.], 2013.

LAMôNICA, H.; LINERO, F. A. B. Importância da palha na geração de excedentes de eletricidade. In: **Curso de Caldeiras, Vapor e Energia (SINATUB)**. [S.l.: s.n.], 2013.

LEAL, M. R. L. V.; GALDOS, M. V.; SCARPARE, F. V.; SEABRA, J. E. A.; WALTER, A.; OLIVEIRA, C. O. F. Sugarcane straw availability, quality, recovery and energy use: A literature review. **Biomass and bioenergy**, v. 53, p. 11–9, 2013.

LEMMON, E. W.; JACOBSEN, R. T. Viscosity and thermal conductivity equations for nitrogen, oxygen, argon and air. **International Journal of Thermophysics**, v. 25, p. 21–69, 2004.

LEMMON, E. W.; SPAN, R. Short fundamental equations of state for 20 industrial fluids. **J. Chem. Eng.**, v. 52, p. 785–850, 2006.

LIPPKE, F. **Simulation of the part-load behavior of a 30MWe SEGS plant**. [S.l.], 1995.

LOO, S. van; KOPPEJAN, J. The handbook of biomass combustion and cofiring. In: ____. [S.l.]: Earthscan, 2008. cap. Environmental Aspects of Biomass Combustion, p. 291–378.

LORA, E. E. S.; ARRIETA, F. R. P.; BESSA, F. C.; ARADAS, M. E. C. Geração termelétrica - planejamento, projeto e operação - volume 1. In: ____. [S.l.]: Editora Interciência, 2004. cap. Caldeiras de vapor convencionais e de recuperação, p. 171–248.

MAGASINER, N. Boiler design and selection in the cane sugar industry. In: **Proceedings of The South African Sugar Technologists Association**. [S.l.: s.n.], 1966.

MANZOLINI, G.; GIOSTRI, A.; SACCILOTTO, C.; SILVA, P.; MACCHI, E. Development of an innovative code for the design of thermodynamic solar power plants part a: Code description and test case. **Renewable Energy**, v. 36, p. 1993–2003, 2011.

MANZOLINI, G.; GIOSTRI, A.; SACCILOTTO, C.; SILVA, P.; MACCHI, E. Development of an innovative code for the design of thermodynamic solar power plants part b: Performance assessment of commercial and innovative technologies. **Renewable Energy**, v. 36, p. 2465–73, 2011.

MONTES, M. J.; ROVIRA, A.; MUñOZ, M.; MARTíNEZ-VAL, J. M. Performance analysis of an integrated solar combined cycle using direct steam generation in parabolic trough collectors. **Applied Energy**, v. 88, p. 3228–38, 2011.

MORIN, G.; DERSCH, J.; PLATZER, W.; ECK, M.; HäBERLE, A. Comparison of linear fresnel and parabolic trough collector power plants. **Solar Energy**, v. 86, p. 1–12, 2012.

NETO, V. C.; RAMON, D. **Análises de opções tecnológicas para projetos de cogeração no setor sucroalcooleiro**. [S.l.], 2002.

NIXON, J.; DEY, P.; DAVIES, P. The feasibility of hybrid solar-biomass power plants in india. **Energy**, v. 46, p. 541–54, 2012.

NOVATEC SOLAR. **Direct molten salt (DMS) demonstrator at demonstration plant PE 1 in Spain**. 2015. Available in: <http://www.novatec-solar.com/121-1-DMS-Demo-E.html>.

PATNODE, A. M. **Simulation and performance evaluation of parabolic trough solar power plants**. Master thesis (Master) — University of Wisconsin-Madison, 2006.

PENG, S.; HONG, H.; WANGA, Y.; WANGA, Z.; JIN, H. Off-design thermodynamic performances on typical days of a 330 mw solar aided coal-fired power plant in china. **Applied Energy**, v. 130, p. 500–9, 2014.

PETERSEIM, J. H.; HELLWIG, U.; TADROS, A.; WHITE, S. Hybridisation optimization of concentrating solar thermal and biomass power generation facilities. **Solar Energy**, v. 99, p. 203–14, 2014.

PETERSEIM, J. H.; TADROS, A.; HELLWIG, U.; WHITE, S. Increasing the efficiency of parabolic trough plants using thermal oil through external superheating with biomass. **Energy Conversion and Management**, v. 77, p. 784–93, 2014.

PIERCE, W.; GAUCHé, P.; BACKSTRöM, T. von; BRENT, A. C.; TADROS, A. A comparison of solar aided power generation (sapg) and stand-alone concentrating solar power (csp): A south african case study. **Applied Thermal Engineering**, v. 61, p. 657–62, 2013.

PLATAFORMA SOLAR DE ALMERIA (PSA). **Photo Gallery: Plataforma Solar de Almeria - Dish/Stirling System Eurodish**. 2015. Available in: <http://www.volker-quaschning.de/fotos/psa/index_e.php>.

POLING, B. E.; PRAUSNITZ, J. M.; O'CONNELL, J. P. **The Properties of Gases and Liquids**. [S.l.]: McGraw-Hill, 2004.

POPOV, D. An option for solar thermal repowering of fossil fuel fired power plants. **Solar Energy**, v. 85, p. 344–49, 2011.

PRIETO, M. G. S. **Alternativas de Cogeração na Indústria Sucroalcooleira, Estudo de Caso.** Master thesis (Master) — Universidade Estadual de Campinas, 2003.

QUERO, M.; KORZYNIETZ, R.; EBERT, M.; JIMéNEZA, A.; RíO, A. del; BRIOSO, J. Solugas - operation experience of the first solar hybrid gas turbine system at mw scale. **Energy Procedia**, v. 49, p. 1820–30, 2014.

REDEAGRO. **Uso da terra no Brasil**. 2010. Available in: <http://redeagro-.org.br/>.

RENEWABLES 2013 - Global status report. [S.l.], 2013.

RICE, J. D. **Employing an effectiveness model for calculating cooling tower performance**. Master thesis (Master) — Georgia Institute of Technology, 1991.

RICHTER, W.; GOERNER, K. Vdi heat atlas. In: ____. [S.l.]: Sringer, 2010. cap. Heat Radiation in Furnaces, p. 1001–12.

RODRIGUES, J. P. Biomass power generation: sugarcane bagasse and trash. In: ____. 1. ed. [S.l.]: PNUD - Programa das Nações Unidas para o Desenvolvimento; CTC - Centro de Tecnologia Canavieira, 2005. cap. Trash recovery cost, p. 19–23.

SCHUHMACHER, R.; BURIN, E. K. L.; BAZZO, E. Thermodynamic and economic analysis of a biomass power plant aided by linear fresnel collectors. In: **Proceedings of 22nd International Congress of Mechanical Engineering (COBEM 2013)**. [S.l.: s.n.], 2013.

SEABRA, J. E. A. **Avaliação técnico-econômica de opções para o aproveitamento integral da biomassa de cana no Brasil**. Phd thesis (Phd) — Universidade Estadual de Campinas (UNICAMP), 2008.

SHAMS POWER COMPANY PJSC. 2015. Available in: <http://www-.shamspower.ae/en/>.

SHLYAKHIN, P. **Steam turbines: theory and design**. [S.l.]: University Press of the Pacific, 2005.

SKYFUEL. **SkyTrough Brochure**. 2011. Acesso em: 17 dez. 2012. Available in: <http://www.skyfuel.com>.

SOLARGIS. **SolarGIS :: Online data and tools for solar energy projects**. March 2014.

SOLARPACES. **Solar Power And Chemical Energy Systems: International Project Database**. Janeiro 2015. Available in: <http://www.solarpaces.org/News/Projects/projects.htm>.

SOLARPACES - SOLAR POWER AND CHEMICAL ENERGY SYSTEMS. **CSP Projects Around the World**. November 2014. Available in: <http://www.solarpaces.org/csp-technology/csp-projects-around-the-world>.

SOLUTIA. **Therminol® VP-1 Technical Bulletin**. 10300 Olive Boulevard - PO Box 66760, June 2014. Available in: <http://www.therminol.com-/products/Therminol-VP1>.

SONNTAG, R. E.; BORGNAKKE, C.; WYLEN, G. J. V. **Fundamentals of Thermodynamics**. [S.l.]: John Wiley & Sons, Inc., 2003.

SOUZA, Z. J. de. **Bioelectricity oberview**. April 2014. Available in: <http:-//www.unica.com.br/multimedia>.

SPAN, R.; W., L. E.; JACOBSEN, R. T.; WAGNER, W.; YOKOZEKI, A. A reference equation of state for the thermodynamic properties of nitrogen for temperatures from 63.151 to 1000 k and pressures to 2200 mpa. **J. Phys. Chem.**, v. 29, 2000.

SPAN, R.; WAGNER, W. A new equation of state for carbon dioxide covering the fluid region from the triple-point temperature to 1100 k at pressures up to 800 mpa. **J. Phys. Chem.**, v. 25, 1996.

SPENCER, J. W. Fourier series representation of the position of the sun. **Search**, v. 2, 1971.

SPIRAX SARCO. **Pressurised Deaerators**. November 2014. Electronic. Available in: <http://www.spiraxsarco.com/>.

SPLIETHOFF, H. **Power generation from solid fuels**. [S.l.]: Springer, 2010.

STEWART, R. B.; JACOBSEN, R. T.; WAGNER, W. Thermodynamic properties of oxygen from de triple point to 300 k with pressures to 80 mpa. **J. Phys Chem.**, v. 20, 1991.

STUETZLE, T. A. **Automatic Control of the 30 MWe SEGS VI Parabolic Trough Plant**. Master thesis (Master) — University of Wisconsin-Madison, 2002.

SURESH, M.; REDDY, K.; KOLAR, A. K. 4-e (energy, exergy, environment, and economic) analysis of solar thermal aided coal-fired power plants. **Energy for Sustainable Development**, v. 14, p. 267–79, 2010.

SWERA. **Solar and Wind Energy Resource Assessment**. 2015. Available in: <http://en.openei.org/apps/SWERA/>.

TORRESOL ENERGY. **Gemasolar power plant**. 2015. Available in: <http://www.torresolenergy.com/TORRESOL/gemasolar-plant/en>.

TURCHI, C. **Parabolic Trough Reference Plant for Cost Modeling with the Solar Advisor Model (SAM)**. [S.l.], 2010.

VESOVIC, V.; WAKEHAM, W. A.; OLCHOWY, G. A.; SENGERS, J. V.; WATSON, J. T. R.; MILLAT, J. The transport properties of carbon dioxide. **J. Phys. Chem.**, v. 19, 1990.

WAGNER, M. J.; GILMAN, P. **Technical Manual for the SAM Physical Trough Model**. 1617 Cole Boulevard, Golden, Colorado 80401, June 2011.

WILKE, C. R. A viscosity equation for gas mixtures. **Journal of Chemical Physics**, v. 18, 1950.

XCEL. **The Colorado Integrated Solar Project**. [S.l.], 2011.

YAN, Q.; YANG, Y.; NISHIMURA, A.; KOUZANI, A.; HU, E. Multi-point and multi-level solar integration into a conventional coal-fired power plant. **Energy Fuels**, v. 24, p. 3733–38, 2010.

YANG, Y.; YAN, Q.; ZHAI, R.; KOUZANI, A.; HU, E. An efficient way to use medium-or-low temperature solar heat for power generation - integration into conventional power plant. **Applied Thermal Engineering**, v. 31, p. 157–62, 2011.

YAWS, C. L. **Chemical properties handbook**. [S.l.]: McGraw-Hill, 1999.

ZHAO, J. Analysis of solar aided steam production in a pulverized coal boiler. In: **Asia-Pacific Power and Energy Engineering Conference**. [S.l.: s.n.], 2012. p. 1–4.

ZHAO, Y.; HONG, H.; JIN, H. Evaluation criteria for enhanced solarecoal hybrid power plant performance. **Applied Thermal Engineering**, v. 73, p. 575–85, 2014.

ZHAO, Y.; HONG, H.; JIN, H. Mid and low-temperature solar coal hybridization mechanism and validation. **Energy**, p. 1–10, 2014.

ZHU, G.; NEISES, T.; TURCHI, C.; BEDILION, R. Thermodynamic evaluation of solar integration into a natural gas combined cycle power plant. **Renewable Energy**, v. 74, p. 815–24, 2015.

APPENDIX A – SOLAR FIELD MODEL VERIFICATION

The verification of solar field model was performed considering the 30 MW SEGS VI plant operational data reported by Stuetzle (2002). SEGS VI power plant is equipped with LS-2 SCEs and Luz Cermet HCEs. There are 800 SCAs disposed in 50 loops. Expansion and overflow tanks are located in the output of solar field and accommodate expansion of HTF. The plant's layout is presented in Figure 43.

Figure 43: SEGS VI power plant layout.

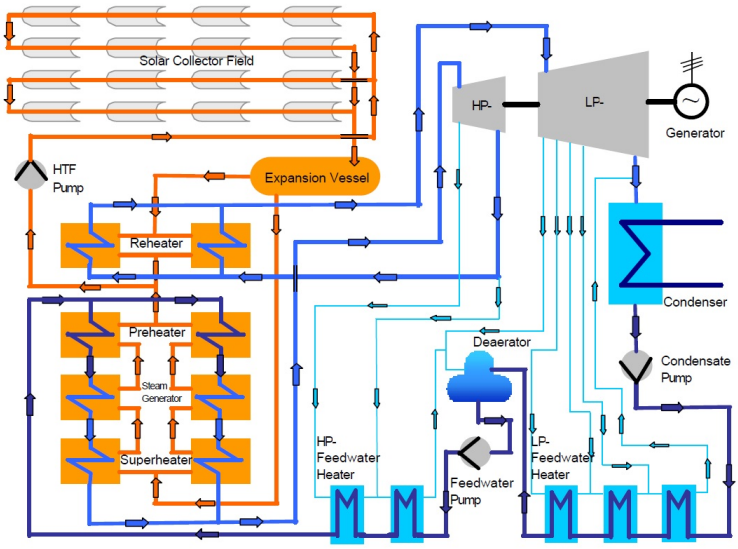

Source: (STUETZLE, 2002).

The solar field model presented in Chapter 4 does not include thermal capacitance effects. Thus, a fully-mixed storage tank model was implemented to account for the thermal capacitance of the heat transfer fluid in the solar field and the expansion and overflow tanks (PATNODE, 2006). The storage tank was located between the solar field and the plant's heat exchanger train.

A schematic of solar field model verification process is presented in Figure 44. Experimentally measured parameters are: HTF temperature and volume flow in solar field inlet, solar irradiance, ambient temperature and wind velocity. The model input parameters were set according to solar field specifications. Heat loss in heat collector elements was modeled according

to Burkholder and Kutscher (2009). Degradation factors were set according to Table 14 of Chapter 7. Storage tank capacity was set as 313 tonnes of thermal oil accounting for the mass of HTF in solar field (evacuated tubes) and expansion and overflow tanks under design point.

Figure 44: Schematic of solar field model verification.

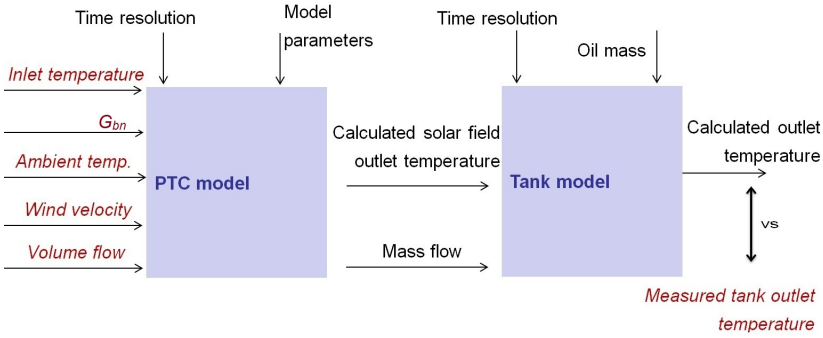

Two operation days were used in verification process. Solar irradiance profiles of both summer and winter days are shown in Figure 45. Blue lines represent data with 12-minutes time resolution. Sum markers in red represent average irradiance for 1-hour time resolution (averages were calculated based on raw data reported by Stuetzle (2002)). Three time resolutions were tested in order to compare the accuracy of simulation model.

Figure 45: DNI data of two typical operation days used in verification process presented under two time steps.

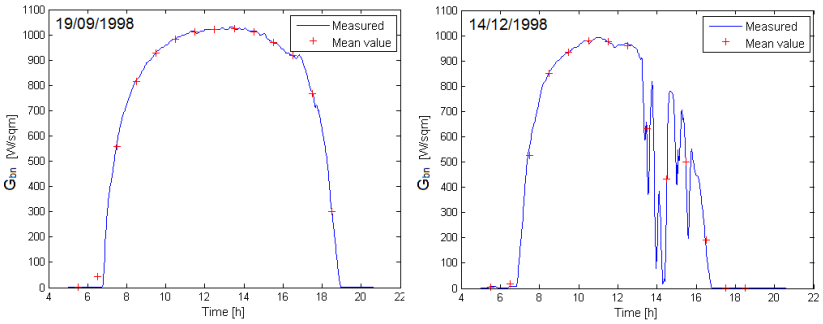

Source: (STUETZLE, 2002).

It is presented in Figure 46 the comparison of measured and simulated

temperature values in the outlet of expansion tank for the two tested operation days. As it can be observed, simulated and measured values matched accordingly for the summer day; the difference was increased when comparing results for winter day. There are two possibilities for increased differences: sub-estimation of heat losses during winter and/or variation of cleanliness of mirrors. Both aspects lead to solar field efficiency variation.

Figure 46: Comparison of measured and calculated HTF temperature in expansion tank outlet (12-minutes time resolution) for two typical operation days.

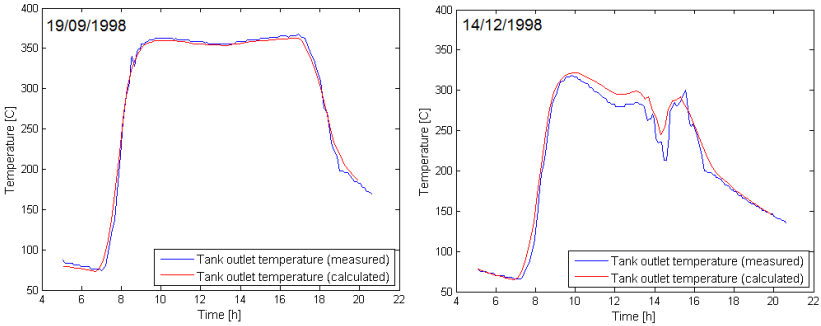

Source: (STUETZLE, 2002).

The prediction of HTF temperature in the expansion tank output was also performed for 30-minutes and 1-hour time resolutions. There was the interest to identify if the reduction in time resolution would bring degradation of simulation accuracy in terms of daily absorbed heat once available TMY data sets are normally limited to 1-hour time steps. As it can be seen in Figure 47, the same general pattern was observed. What happened, nevertheless, is that once time resolution was decreased some temperature fluctuation details were lost (compare winter day results in Figures 46 and 47). It might be clarified here that the aim of this work consisted on estimating the annual gains in sugarcane bagasse cogeneration plants electricity generation due to hybridization. To do that 1-hour time resolution TMY data was here used. The detailed evaluation on the dynamic operation of components (specially solar field and steam generators) might be carefully aderessed in the next step.

Finally, the absorbed energy in solar field was calculated based on measured data and compared with results predicted by simulation model under three distinct time resolutions (see Table 20). There was no significant degradation in accuracy of daily energy collection results as time resolution was decreased. The improvement in time resolution turns possible to find details of temperature fluctuations and this is important when studing the dynamic

Figure 47: Comparison of measured and calculated HTF temperature in expansion tank outlet (1-hour time resolution) for two typical operation days.

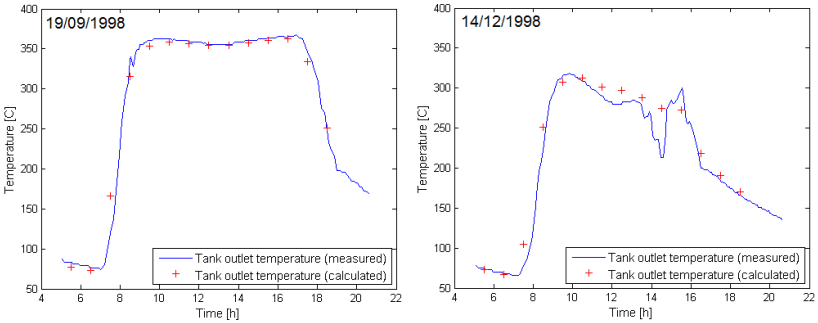

Source: (STUETZLE, 2002).

Table 20: Comparison of solar field energy output calculated by using measured data and simulated data under distinct time resolutions.

Day	Parameter	Measured (12 mins)	Model (12 mins)	Model (30 mins)	Model (1 hour)
19/09/1998	Energy [MJ]	3.586E+6	3.712E+6	3.705E+6	3.703E+6
	Error [%]	-	3.5	3.4	3.3
14/12/1998	Energy [MJ]	1.022E+6	1.330E+6	1.334E+6	1.333E+6
	Error [%]	-	30.2	30.6	30.5

operation of cycle components. Again, simulated and measured values matched accordingly for the summer day, while the prediction error was increased for the winter day. The reason can be the sub-estimation of heat losses during winter and/or variation of cleanliness of mirrors. Both aspects lead to solar field efficiency variation.

APPENDIX B – STEAM GENERATORS MODELING

It is presented in this chapter the set of equations and corresponding hypothesis implemented in this work to reproduce the performance of sugarcane bagasse steam generators. The scope is certainly limited as the detailed analysis is dependent on particular configuration, geometry and operational parameters of steam generator under evaluation. Here the focus was based on natural circulation subcritical water tube steam generators composed of combustion chamber, boiler, convective superheating system, economizer and tubular air heaters.

B.1 ENERGY BALANCE

The energy balance of a steam generator is schematically represented in Figure 48. It consisted on calculating the energy input rate ($\dot{E}_{in}$ [kW]), energy credits rate ($\dot{E}_{cred}$ [kW]), energy losses rate ($\dot{E}_{l}$ [kW]) and energy output rate ($\dot{E}_{out}$ [kW]). The relationship between these terms was given by Equation B.1 (ASME..., 2008),

$$\dot{E}_{in} + \dot{E}_{cred} = \dot{E}_{out} + \dot{E}_{l} \tag{B.1}$$

or yet devided per fuel mass flow rate,

$$e_{in} + e_{cred} = e_{out} + e_{l} \tag{B.2}$$

As simplifying assumptions adopted in this work, energy streams related to auxiliary equipment power, soot blowing system, air infiltration and NO_x formation were desconsidered.

The ambient reference condition adopted for calculations is presented below:

- Ambient temperature and pressure: $T_0 = 25\ ^oC$ and $p_0 = 1.01\ bar$;
- Air volumetric composition: $y_{air,O_2} = 0.2095$ and $y_{air,N_2} = 0.7905$;
- Air gravimetric composition: $c_{air,O_2} = 0.2314$ and $c_{air,N_2} = 0.7686$.

The energy input was based on fuel's Higher Heat Value (HHV) as procedure described on ASME... (2008) (Equation B.3),

$$\dot{E}_{in} = \dot{m}_{fuel}\, HHV \tag{B.3}$$

or yet devided per fuel mass flow rate.

$$e_{in} = HHV \tag{B.4}$$

Figure 48: Energy balance of steam generators.

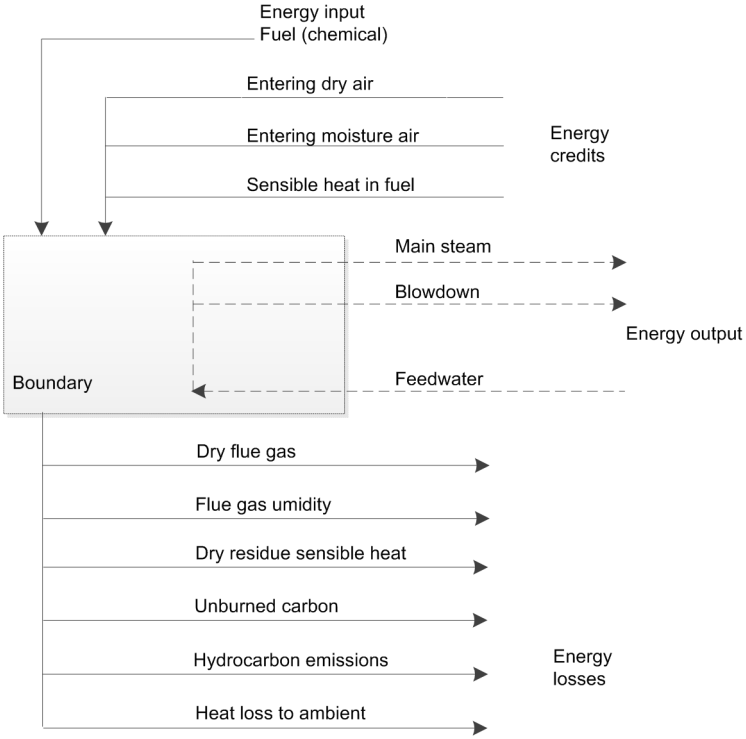

Source: Adapted from ASME… (2008).

In the next sections the calculation steps implemented to evaluate the other terms of Equation B.1 are presented.

B.1.1 Combustion

The dry stoichiometric air mass flow represents the ideal amount of air necessary to react with fuel to transform carbon to CO_2, hydrogen to H_2O and sulfur to SO_2[1]. Its calculation considered correction in carbon content due to unburned carbon present in ash, as represented by Equation B.5 in a specific basis (per kilogram of fuel [kg/kg]),

$$m_{air,d}^{st} = 138.2 \left(\frac{C_{fuel} - C_{ash}}{12} + \frac{H_{fuel}}{4} + \frac{S_{fuel}}{32} - \frac{O_{fuel}}{32} \right) \tag{B.5}$$

where C_{fuel}, H_{fuel}, S_{fuel} and O_{fuel} are the carbon, hydrogen, sulfur and oxygen mass per kilogram of fuel [kg/kg]. The term C_{ash} is the share of fuel carbon found in ash given in kilogram of unburned carbon per kilogram of fuel [kg/kg].

The unburned carbon content, C_{ash} [kg/kg], depends on several factors related to steam generator's design and operation. Its determination consists initially on measuring the share of carbon in ash. The collected mixture of ash and unburned carbon was called residue. As distinct ash collection points might be present in steam generators, the final composition was calculated according to Equation B.6,

$$C_r = \alpha\, C_{r,\alpha} + \beta\, C_{r,\beta} + \gamma\, C_{r,\gamma} + ... \tag{B.6}$$

where $\alpha + \beta + \gamma + ... = 1$ represented the share of residue mass flow identified in distinct residue collection points and ($C_{r,\alpha}$, $C_{r,\beta}$, $C_{r,\gamma}$, ...) the unburned carbon content in residue [kg/kg] for the distinct residue collection points.

The correction of unburned carbon content per kilogram of residue to unburned carbon content per kilogram of fuel was performed by Equations B.7 and B.8.

$$R = Ash_{fuel} / (1 - C_r) \tag{B.7}$$

$$C_{ash} = C_r\, R \tag{B.8}$$

where R is the mass of residue (ash plus carbon) per kilogram of fuel [kg/kg].

[1] In an actual combustion process, small amounts of CO, nitrous oxides (NO_x) and other species are formed, but the impact of them in the calculation of air and flue gas mass flow can be considered negligible (ASME..., 2008).

Air excess in addition to the stoichiometric amount is used to minimize the unburned carbon content in ash. Nevertheless, if in one side increasing air excess improves combustion efficiency, the flue gas sensible heat thermal loss is also increased and the optimal operation point that maximizes thermal efficiency of steam generator might be determined (BAZZO, 1995). The air excess was represented by Equation B.9,

$$ae = 100\,\frac{m_{air,d}}{m^{st}_{air,d}} \cong 100\,\left(\frac{0.21}{0.21 - y_{fg,O_2}} - 1\right) \tag{B.9}$$

where y_{fg,O_2} [kmol/kmol] consisted on the mole fraction of oxygen in dry flue gas measured after combustion process.

Based on air excess, the total amount of dry air was calculated by Equation B.10. In addition, the mass flow of wet air considering also air humidity was calculated by Equation B.11,

$$m_{air,d} = m^{st}_{air,d}\,\left(1 + \frac{ae}{100}\right) \tag{B.10}$$

$$m_{air} = m_{air,d}\,(1 + \omega_{air}) \tag{B.11}$$

where $m_{air,d}$ is the mass flow of dry air per kilogram of fuel [kg/kg], m_{air} is the mass flow of wet air per kilogram of fuel [kg/kg] and ω_{air} is the air humidity ratio (kilogram of water per kilogram of dry air [kg/kg]).

Finally, the mass flow rate of wet air $\dot{m}_{air}$ [kg/s] was represented according to Equation B.12.

$$\dot{m}_{air} = m_{air}\,\dot{m}_{fuel} \tag{B.12}$$

The mass flow of wet flue gas depends on fuel composition, fuel moisture, air humidity and air excess. It was calculated by Equation B.13 in a specific basis (per kilogram of fuel [kg/kg]) and by Equation B.14 in kilograms of flue gas per second.

$$\begin{aligned} m_{fg} = {} & 44\,\frac{C_{fuel} - C_{ash}}{12} + 64\,\frac{S_{fuel}}{32} + 18\,\frac{H_{fuel}}{2} + m_{air,d}\,\omega_{air} + N_{fuel} + \\ & + m_{air,N_2}\,m^{st}_{air,d}\,(1 + ae) + m_{air,O_2}\,m^{st}_{air,d}\,ae + H2O_{fuel} \end{aligned} \tag{B.13}$$

$$\dot{m}_{fg} = m_{fg}\,\dot{m}_{fuel} \tag{B.14}$$

B.1.2 Energy credits

B.1.2.1 Entering air

The sensible heat of air $e_{cred,air}$ [kJ/kg] was accounted by the sum of both dry air $e_{cred,air,d}$ [kJ/kg] and air moisture e_{cred,air,H_2O} [kJ/kg] specific heat streams (Equations B.15, B.16 and B.17),

$$e_{cred,air,d} = m_{air,d} \left(h_{air,d}(T_{air}) - h_{air,d}(T_{ref})\right) \tag{B.15}$$

$$e_{cred,air,H_2O} = m_{air,H_2O} \left(h_{air,H_2O}(T_{air}) - h_{air,H_2O}(T_{ref})\right) \tag{B.16}$$

$$e_{cred,air} = e_{cred,air,d} + e_{cred,air,H_2O} \tag{B.17}$$

where air temperature was related to the inlet temperature in system's control volume.

B.1.2.2 Sensible heat in fuel

The sensible heat of fuel is accounted by Equation B.18,

$$e_{cred,fuel} = cp_{fuel} \left(T_{fuel} - T_ref\right) \tag{B.18}$$

where the specific heat for sugarcane bagasse was set as $cp_{fuel} = 1.76$ kJ/kg (IPT, 1990).

B.1.3 Energy losses

B.1.3.1 Flue gas

The thermal heat loss related to flue gas stream was also treated considering separately dry flue gas and its humidity content. The enthalpy of dry flue gas was dependent on its main components (CO_2, SO_2, O_2 and N_2) and the mixture's enthalpy calculation was described in Section B.3. The dry flue

gas heat loss $e_{l,fg,d}$ [kJ/kg] was represented by Equation B.19.

$$e_{l,fg,d} = m_{fg,d}\,(h_{fg,d}(T_{fg}) - h_{fg,d}(T_{ref})) \tag{B.19}$$

Regarding flue gas humidity heat loss e_{l,fg,H_2O} [kJ/kg], its calculation considered not just sensible heat but also the evaporation heat related to fuel moisture and water formed due to its hydrogen content (Equation B.20)[2].

$$\begin{aligned} e_{l,fg,H_2O} = \left(H_2O_{fuel} + 18\,\frac{H_{fuel}}{2}\right)\,h_{lv,H_2O} + \\ + m_{fg,H_2O}\,(h_{fg,H_2O}(T_{fg}) - h_{fg,H_2O}(T_{ref})) \end{aligned} \tag{B.20}$$

Finally, flue gas heat loss was given by Equation B.21.

$$e_{l,fg} = e_{l,fg,d} + e_{l,fg,H_2O} \tag{B.21}$$

B.1.3.2 Dry residue sensible heat

The thermal loss related to dry residue sensible heat was accounted for each stream leaving the control volume. As this term represented a low share in heat loss due to low ash content of sugarcane bagasse, an approximate procedure was here used, as presented by Equation B.22 (ASME..., 2008),

$$\begin{aligned} e_{l,ash} = \alpha\,R\,(h_r(T_\alpha) - h_r(T_{ref})) + \\ + \beta\,R\,(h_r(T_\beta) - h_r(T_{ref})) + \\ + \gamma\,R\,(h_r(T_\gamma) - h_r(T_{ref})) + ... \end{aligned} \tag{B.22}$$

where residue enthalpy h_r [kJ/kg] was given according Equation B.23 as a function of temperature (in Kelvin, K) and Table 21. Coefficients are based upon a curve fit for SiO_2 (ASME..., 2008).

$$h_r(T) = 2.326\,(C_0 + C_1\,T + C_2\,T^2 + C_3\,T^3 + C_4\,T^4 + C_5\,T^5) \tag{B.23}$$

[2]The evaporation heat related to fuel moisture and water formed due to its hydrogen content was considered in heat loss calculation as heat input was based on HHV of fuel. The utilization of LHV in heat balance calculations indicates that evaporation of water is previously stated as energy loss.

Table 21: Coefficients for dry residue enthalpy calculation.

Parameter	For T from 255 to 1000 K	For T above 1000 K
C_0	-0.32E+02	0.18E+02
C_1	-0.24E+00	0.36E-01
C_2	0.17E-02	0.43E-03
C_3	-0.26E-05	-0.20E-06
C_4	0.21E-08	0.48E-10
C_5	-0.64E-12	-0.46E-14

Source: (ASME..., 2008)

B.1.3.3 Unburned carbon

The calculation of heat loss due to unburned carbon in ash was based on the previously calculated term C_{ash} [kg/kg], and it was based on Equation B.24,

$$e_{l,unb} = C_{ash}\, h_C \tag{B.24}$$

where the heating value of carbon is $h_C = 33727$ kJ/kg.

B.1.3.4 Hydrocarbon emissions

The conversion of biomass carbon to CO_2 takes place through several elementary steps and several intermediate components are formed and reacted. Monoxide carbon, CO, is the most important final intermediate. Hydrocarbons are, in general, earlier intermediates than CO, which means they have lower emission levels. In this way, CO was here regarded as a good indicator of combustion efficiency (LOO; KOPPEJAN, 2008).

Considering the volumetric concentration of CO in dry flue gas, CO_{fg} [mg/Nm^3], the specific mass flow of CO (kilogram of CO per kilogram of fuel) was calculated according to Equation B.25,

$$m_{CO} = 10^{-6}\, v_{fg,d}\, CO_{fg} \tag{B.25}$$

where $v_{fg,d}$ [Nm^3/kg] is the volumetric flow of dry flue gas per kilogram of burned fuel.

Finally, the heat loss $e_{l,CO}$ [kJ/kg] was calculated by Equation B.26,

$$e_{l,CO} = m_{CO}\, h_{CO} \tag{B.26}$$

where the heating value of monoxide carbon is $h_{CO} = 10111$ kJ/kg.

In Brazil the CONAMA 382 Resolution defines emission limits for particulate matter and NOx in thermal systems that use sugarcane bagasse external combustion. For low thermal capacity systems (< 10 MW) only CO limits are specified (CONAMA - CONSELHO NACIONAL DO MEIO AMBIENTE, 2006), as stated in Table 22.

Table 22: Monoxide carbon emission limits for thermal systems that use sugarcane bagasse external combustion.

Nominal thermal capacity, $\dot{Q}$ [MW]	CO [mg/Nm^3][a]
Up to 0.05	6500
$0.05 < \dot{Q} <= 0.15$	3250
$0.15 < \dot{Q} <= 1.0$	1700
$1.0 < \dot{Q} <= 10$	1300

Source: (CONAMA - CONSELHO NACIONAL DO MEIO AMBIENTE, 2006).

[a]For dry flue gas with 8% oxygen excess.

The CO emission is related to the excess air ratio and combustion temperature (LOO; KOPPEJAN, 2008). The CO profile as a function of combustion temperature for biomass combustion applications is presented in Figure 49. As the combustion temperature is decreased in comparison to the design point, the CO emission [mg/Nm^3] is increased exponentially. Surely this represents a general trend once the problem is dependent on the type of fuel, operation parameters and the furnace configuration.

B.1.3.5 Heat loss to ambient

The accurate determination of surface radiation and convection heat loss of steam generator to the ambient, $e_{l,a}$ [kJ/kg], is a difficult task. In ASME... (2008) standard a correlation is presented based on the measurement of flat projected surface area of casing, average surface temperature and average air velocity and ambient temperature at 2 to 5 ft of surface. A systematic uncertainty for the correlation of at least ± 30 % is suggested if the parameters required are measured accordingly.

In Magasiner (1966) it is presented a review on heat transfer modeling and efficiency calculation of sugarcane bagasse steam generators. Regarding

Figure 49: CO emission in mg/Nm^3 as a function of combustion temperature for biomass combustion applications.

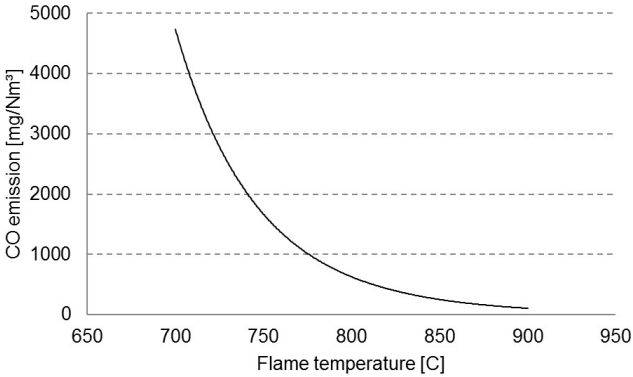

Source: adapted from Loo and Koppejan (2008).

radiation and convection heat loss to the ambient, the author states that it ranges from 0.5 to 1.5 % of the heat input given by $\dot{m}_{fuel}\ LHV$. The efficiency of a 45 t/h capacity (superheated steam with parameters of 19 bar and 320 ^{o}C) sugarcane bagasse steam generator was calculated experimentally in Barroso *et al.* (2003) and the thermal loss to the ambient was found to be 1.2 % of heat input at full load. Finally, Lora *et al.* (2004) states that heat loss to the ambient in sugarcane bagasse steam generators is in average 0.8 % of heat input. As load is reduced in off-design operation, the relative importance of this loss is increased as evaporation temperature can be assigned to be constant - keeping constant the heat loss in an absolute basis [kW].

B.1.4 Energy output

Energy output is the amount transferred to the water-steam circuit. In ASME... (2008) standard the term related to blowdown stream is also accounted as energy output[3]. Other streams (as auxiliary steam) might also be included as output if they are implemented in the steam generator to be evaluated. Energy output, $\dot{E}_{out}$ [kW], was here calculated by Equation B.27 and in a specific basis (per kilogram of fuel) by Equation B.28,

$$\dot{E}_{out} = \dot{m}_{sh}\ (h_{sh} - h_{fw}) + (\dot{m}_{fw} - \dot{m}_{sh})\ (h_{bd} - h_{fw}) \tag{B.27}$$

[3]Blowdown stream can also be accounted as energy loss accordingly.

$$e_{out} = \dot{E}_{out} / \dot{m}_{fuel} \tag{B.28}$$

where the subscripts *sh*, *fw* and *bd* are superheated steam, feedwater and blowdown, respectively.

B.1.5 Efficiency calculation

Steam generator's efficiency can be calculated by the direct and energy balance methods (ASME..., 2008). The direct method is based on the measurement of output and heat input energy streams as it is represented by Equation B.29.

$$\eta_{dm,HHV} = 100 \frac{\dot{E}_{out}}{\dot{m}_{fuel} HHV} \tag{B.29}$$

The measurement of solid fuels mass flow is a difficult task that brings high uncertainty to the efficiency calculated using the direct method. In this regard, the energy balance method is commonly used by taking advantage of energy credits and losses calculated in a specific basis (per kilogram of fuel [kJ/kg]). By rearranging Equation B.2 the heat output energy stream is stated as,

$$e_{out} = e_{in} + e_{cred} - e_l$$

Thus, efficiency calculation according to the energy balance method is represented by Equation B.30.

$$\eta_{eb,HHV} = 100 \left[1 + \frac{(e_{cred} - e_l)}{HHV} \right] \tag{B.30}$$

The thermal efficiency calculation can also be based on LHV of fuel. In this regard the latent heat related to fuel moisture and water steam formed due to its hydrogen content is not considered in flue gas heat loss calculation as discussed on Section B.1.3.1.

B.2 HEAT TRANSFER ANALYSIS

B.2.1 Combustion chamber

Modeling the heat transfer in a combustion chamber is a very complex problem involving distinct phenomena. On sugarcane bagasse steam generators this process is dominated by radiation with a participant media composed of gaseous combustion room components and suspended particulate matter, as soot, char and ash (MAGASINER, 1966). The problem is characterized by a strong coupling between flow, concentration, heat release and temperature fields (RICHTER; GOERNER, 2010).

In this work the heat released from products of combustion to the furnace walls was evaluated according to the empirical model presented by Spliethoff (2010) with focus on coal combustion, natural gas and oil. The same approach is described by Magasiner (1966) for sugarcane bagasse steam generators.

As it is stated by Equation B.31, the heat released by products of combustion, $\dot{Q}_f$ [kW], is related to the cooling of flue gas along the furnace,

$$\dot{Q}_f = \varepsilon_{fs}\,\sigma\,A_f\,(T_e^4 - T_w^4)/1000 = \dot{m}_{fg}\,\overline{cp}_{fg}\,(T_{ad} - T_{fe}) \tag{B.31}$$

where ε_{fs} [-] is the effective emissivity between flame and surface, $\sigma = 5.67 \cdot 10^{-18} W/m^2K^4$, A_f [m^2] is the flame surface area, T_{ad} [K] is the adiabatic temperature in furnace, T_e [K] is the effective furnace mean temperature, T_w [K] is the wall temperature, T_{fe} [K] is the combustion chamber exit temperature, $\dot{m}_{fg}$ [kg/s] is the flue gas mass flow and $\overline{cp}_{fg}$ [kJ/kg K] is the mean specific heat of flue gas calculated between T_{ad} and T_{fe}.

If the flame fills the furnace completely, the flame area A_f [m^2] equals the surface of combustion chamber A_w [m^2]. Otherwise, a correction factor might be used.

The effective emissivity between flame and surface is calculated according to Equation B.32,

$$\varepsilon_{fs} = \left(\frac{1}{\varepsilon_f} + \frac{1}{\varepsilon_w} - 1\right)^{-1} \tag{B.32}$$

where ε_f [-] is the flame emissivity and ε_w [-] is the surface emissivity.

As it is described in Spliethoff (2010), the emissivity of an oxidized

surface is between 0.6 and 0.8. Furnace deposits also affect the emissivity. The apparent emissivity that describes the combined deposit and substrate emissivity lies between 0.5 and 0.8 for most deposits.

The flame emissivity is calculated according to Equation B.33,

$$\varepsilon_f = \varepsilon_\infty \, (1 - exp(-k_f \, t_f)) \tag{B.33}$$

where ε_∞ is the emissivity of a very thick flame. The term t_f [m] is the thickness of the flame, or beam length, and it is calculated according to Equation B.34. Finally, k_f [m^{-1}] depends on the characteristic of the flame, varying from 0.75 for luminous flames to 0.5 for blue flames.

$$t_f = 3.6 \, V/A \tag{B.34}$$

The effective furnace mean temperature was here defined as the geometric mean of the adiabatic combustion temperature and the furnace outlet temperature, as it is stated by Equation B.35.

$$T_e = \sqrt{T_{ad} \, T_{fe}} \tag{B.35}$$

The main objective of this work in performing the modeling of bagasse fired combustion chambers was to indicate the outlet temperature, T_{fe}, for different operation loads. There was no claim to use the described model to design combustion chamber heating surface and cross-section areas (the last related to the allowable cross-sectional heat release). To do that, it would be necessary additional technical information especially based on empirical experience obtained from laboratory and field tests.

At part load operation, the evaporation heat load, $\dot{Q}_{evap}$ [kW], is reduced. In water tube steam generators the evaporation heat load is directly dictated by the radiation heat released by products of combustion to the furnace walls. If evaporation occurs exclusively in water tube walls, we have,

$$\dot{Q}_{evap} = \dot{Q}_f$$

or yet,

$$\dot{Q}_{evap} = \varepsilon_{fs} \, \sigma \, A_f \, (T_e^4 - T_w^4)$$

Now considering that wall temperature T_w is assigned to be constant as it is related to the saturation temperature of steam and that radiation heat transfer is significantly more dependent on furnace effective mean temperature variation than on the variation of ε_{fs} and A_f , we have,

$$\dot{Q}_{evap} \propto T_e^4$$

Finally, combining the previous relationship of proportionality with Equation B.35, we have,

$$\dot{Q}_{evap} \propto T_{fe}^2$$

So, defining $\dot{Q}_{evap,dp}$ and $T_{fe,dp}$ as evaporation heat transfer and furnace outlet temperature at design point, the term T_{fe} at part load was correlated to $\dot{Q}_{evap}$ according to Equation B.36.

$$T_{fe} = T_{fe,dp} \sqrt{\frac{\dot{Q}_{evap}}{\dot{Q}_{evap,dp}}} \tag{B.36}$$

B.2.2 Heat exchange in bundle of tubes

Bundle of tubes are commonly used in superheaters, economizers and air heaters in steam generators. Bundle of tubes can be aligned or scattered, as it is exposed in Figure 50. The parameters s_t, s_l and s_d [m] represent, respectively, the transverse, longitudinal and diagonal spacing of tubes.

Figure 50: Bundle of tubes.

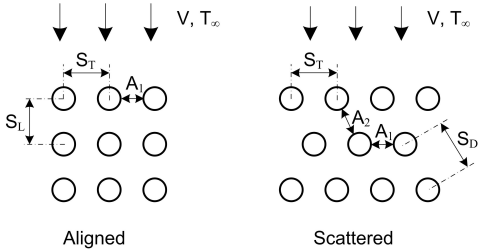

Source: (BERGMAN *et al.*, 2008).

The overall thermal resistance of heat transfer process in a bundle of clean tubes was represented by Equation B.37. In this work no fouling effects were considered.

$$\frac{1}{UA} = \frac{1}{A_{int}\, h_{conv,int}} + R_{cond} + \frac{1}{A_{ext}\, h_{conv,ext}} \tag{B.37}$$

Special attention is given in next sections in presenting correlations to

calculate internal convection in tubes, external convection in bundle of tubes and gaseous radiation - which might be significant depending on flue gas temperature. Based on previously identified UA [kW/K], the heat transferred, $\dot{Q}$ [kW], and the updated output condition of internal and external flows were calculated by the ε-NTU method (BERGMAN *et al.*, 2008). This procedure was here implemented in an iterative way as UA [kW/K] was dependent on internal and external flow parameters.

B.2.3 Internal convection in tubes

Several correlations for liquids, steam or gases are presented in literature to evaluate the internal convection heat transfer in tubes (BERGMAN *et al.*, 2008; KITTO; STULTZ, 2005). The Dittus-Boelter model represented by Equation B.38 was here used. It is recommended as an adequate approximation for fully developed turbulent flow and small to moderate temperature differences,

$$Nu_d = 0.023\, Re_d^{4/5}\, Pr^n \tag{B.38}$$

where Nu_d is the local Nusselt number, Re_d is the Reynolds number, Pr is the Prandtl number, $n = 0.4$ for fluid heating and $n = 0.3$ for fluid cooling. All properties were evaluated at fluid bulk temperature. The model was experimentally validated for the following conditions,

$$\begin{cases} 0.7 \leq Pr \leq 160 \\ Re_d \geq 10000 \\ \frac{L}{d_{int}} \geq 10 \end{cases}$$

A common approximation leading to errors lower than 15 % in Nusselt number calculation consists in considering $\overline{Nu}_d = Nu_d$ for $L/d_{int} > 60$. This approximation was here implemented. In this situation, the fluid properties were evaluated in the average of inlet and outlet bulk temperatures.

B.2.4 External convection in bundle of tubes

The external convection in bundle of tubes was evaluated according to Equation B.39 (BERGMAN *et al.*, 2008),

$$\overline{Nu}_d = C_0 \, Re_{d,max}^{m} \, Pr^{0.36} \left(\frac{Pr}{Pr_s} \right)^{1/4} \tag{B.39}$$

where $\overline{Nu}_d$ is the average Nusselt number and $Re_{d,max}$ is the Reynolds number evaluated in the maximum flow velocity developed, V_{max} [m/s]. All properties were evaluated at the average of inlet and outlet bulk temperatures of fluid with exception of Pr_s evaluated at film temperature. The model was experimentally validated for the following conditions,

$$\begin{cases} N_l \geq 20 \\ 0.7 \leq Pr \leq 500 \\ 1000 \leq Re_{d,max} \leq 2\ 10^6 \end{cases}$$

For the aligned configuration, V_{max} [m/s] occurs in plane A_1 (see Figure 50) and it was calculated according to Equation B.40.

$$V_{max} = \frac{s_t}{s_t - d_{ext}} \, V \tag{B.40}$$

For the scattered configuration, V_{max} [m/s] can occur in plane A_1, but also in plane A_2 if,

$$2 \cdot (s_d - d_{ext}) < (s_t - d_{ext})$$

and in this case V_{max} [m/s] was given by,

$$V_{max} = \frac{s_t}{2\,(s_d - d_{ext})} \, V \tag{B.41}$$

If there was less than 20 longitudinal rows ($N_l < 20$) the correction represented by Equation B.42 was used.

$$\overline{Nu}_{d,(N_l<20)} = C_1 \, \overline{Nu}_{d,(N_l \geq 20)} \tag{B.42}$$

Values for C_0, C_1 and m for the different geometrical configurations (aligned or scattered; tubes spacing) and $Re_{d,max}$ ranges are presented by Bergman *et al.* (2008)

B.2.5 Gas radiation in bundle of tubes

Gas radiation heat transfer is higher as flue gas temperature and the content of CO_2 and H_2O are improved (RICHTER; GOERNER, 2010). In this work it was performed the calculation of the radiation heat transfer coefficient h_{rad} [kW/m^2·K] as it is represented by Equation B.43,

$$h_{rad} = \frac{\dot{Q}''_{CO_2} + \dot{Q}''_{H_2O}}{T_g - T_w} \tag{B.43}$$

where $\dot{Q}''_{CO_2}$ and $\dot{Q}''_{H_2O}$ [kW/m^2] are the heat flux irradiated by CO_2 and H_2O, respectively. The terms T_g and T_w [^{o}C] are the gas and wall temperatures, respectively.

Annaratone (2008) based on several works presents Equations B.44 and B.45 to calculate irradiated heat,

$$\dot{Q}''_{CO_2} = (p_{CO_2}\, L_e)^{0.4} \left[\left(\frac{T_g}{100} \right)^{3.2} - \left(\frac{T_w}{100} \right)^{3.2} \left(\frac{T_g}{T_w} \right)^{0.65} \right] \tag{B.44}$$

$$\dot{Q}''_{H_2O} = 10^{-3}\, (46.5 - 84.9\, p_{H_2O}\, L_e)\, (p_{H_2O}\, L_e)^{0.6} \left[\left(\frac{T_g}{100} \right)^{m} - \left(\frac{T_w}{100} \right)^{m} \right] \tag{B.45}$$

with,

$$m = 2.32 + 1.37\, (p_{H_2O}\, L_e)^{1/3} \tag{B.46}$$

The effective radiation beam length, L_e [m], is dependent on geometry of problem. It was calculated according to Equation B.47 in case of flue gas radiation incident in a bundle of tubes heat exchanger.

$$L_e = 0.85 \left(\frac{4\, s_l\, s_t}{\pi} \right) \tag{B.47}$$

B.3 THERMOPHYSICAL PROPERTIES OF SUBSTANCES

B.3.1 Steam properties

Steam properties were obtained from IAPWS IF97 standard formulation for Matlab®. It provides accurate data for water and steam and mixtures of water and steam properties from 0 - 1000 bar and from 0 - 2000 ^{o}C.

B.3.2 Air and flue gas elements

The thermodynamic and transport (viscosity and thermal conductivity) properties of air and flue gas main components were obtained from Engineering Equation Solver® (EES) real fluids database. The references are summarized in Table 23.

Table 23: References of thermodynamic and transport properties of air and flue gas main components.

Substance	Thermodynamic properties	Transport properties
Nitrogen	(SPAN *et al.*, 2000)	(LEMMON; JACOBSEN, 2004)
Oxygen	(STEWART *et al.*, 1991)	(LEMMON; JACOBSEN, 2004)
Carbon dioxide	(SPAN; WAGNER, 1996)	(VESOVIC *et al.*, 1990)
Sulfur dioxide	(LEMMON; SPAN, 2006)	(YAWS, 1999)

B.3.3 Properties of gas mixtures

The properties of air and flue gas were estimated based on their components. In case of viscosity the model of Wilke (1950) based on kinetic theory approach and valid for low pressure mixtures was used (Equations B.48 and B.49),

$$\mu_m = \sum_{i=1}^{n} \frac{y_i\,\mu_i}{\sum_{j=1}^{n} y_j\,\phi_{ij}} \tag{B.48}$$

$$\phi_{ij} = \frac{[1+(\mu_i/\mu_j)^{1/2}\,(M_j/M_i)^{1/4}]^2}{[8\,(1+M_i/M_j)]^{1/2}} \tag{B.49}$$

where μ [Pa.s] is the dynamic viscosity, y represents mole fraction, the index

m represents mixture and i and j indicate the mixture components.

The thermal conductivity of low pressure gaseous mixtures was estimated in a form analogous to the relation used for mixture viscosity as it is described in Poling *et al.* (2004) (Equation B.50),

$$k_m = \sum_{i=1}^{n} \frac{y_i \, k_i}{\sum_{j=1}^{n} y_j \, A_{ij}} \tag{B.50}$$

where k [W/m ·K] is the thermal conductivity and A_{ij} is approximated to ϕ_{ij} used in case of viscosity.

The specific mass and specific heat of gaseous mixtures were estimated considering ideal gas modeling, as it is stated by Equations B.51 and B.52 (SONNTAG *et al.*, 2003),

$$\rho_m = \sum_{i=1}^{n} \rho_i \tag{B.51}$$

$$cp_m = \sum_{i=1}^{n} c_i \, cp_i \tag{B.52}$$

where ρ [kg/m^3] is the specific mass, cp [kJ/kg-K] is the specific heat and c represents mass fractions.

B.4 DYNAMIC SIMULATION OF STEAM GENERATORS

The simulation of steam generators was performed in this work at steady-state at 1-hour time resolution. In this regard, once there was the variation of any input parameter, the sugarcane bagasse mass flow rate was controlled in order to reach the required main steam production. In other words, it was considered that these components were able to absorb the fluctuations of solar field delivered heat by changing the bagasse feeding rate once it was necessary. The evaluation of the dynamic operation of steam generators might be performed in future works by tunning a dynamic simulation model with field data.

APPENDIX C – DESIGN POINT WEATHER CONDITIONS

Design point weather conditions were identified in order to calculate solar field area of proposed layouts and cooling tower capacity of cogeneration cycle. The procedure is here exemplified considering TMY data (one-hour time resolution) for the city of Campo Grande - MS obtained in Meteonorm® 7.0 data base.

C.1 SOLAR FIELD PARAMETERS

The design point direct normal solar irradiance $G_{bn,ref}$ [W/m^2] consists in a reference for solar field area calculation. It is also necessary to calculate a reference day to find the solar incidence angle in parabolic trough concentrators. This is an important step in design phase once if a very high irradiance value is selected the frequency in which solar field will be operated at full load will be very low in a year. In the other side, if a low irradiance value is selected there will be many hours in a year in which solar field will be defocused.

A normal approach implemented in projects consists in not considering irradiance values smaller than certain lower boundary (e.g. 250 W/m^2) and calculating the 95 % upper percentile to identify $G_{bn,ref}$. In this work, nevertheless, emphasis was given to the harvest period irradiance profile when operation occurs. Thus, irradiance values of each month were evaluated separately, as it can be seen in Figure 51. Design point irradiance was here calculated as the average of the 95 % percentiles identified for months from April to December leading to 953 W/m^2. Design point day was considered the spring equinox in south hemisphere (23th September).

Similar approach was implemented for design point wind velocity calculation (see Figure 52). Values of wind velocity in which $G_{bn} < 250$ W/m^2 were not considered in calculations. The average of the 95 % percentiles identified for months from April to December leaded to 9.5 m/s. High wind velocity lead to increased thermal loss of heat collection elements.

Values of ambient dry-bulb (DB) temperature in which $G_{bn} > 250$ W/m^2 comprised between 5 % and 95 % percentiles are presented in Figure 53. Regarding this parameter the average of temperature values for months from April to December was calculated leading to the value of 27.7 ^{o}C.

Figure 51: Direct normal solar irradiance monthly 95 % percentiles.

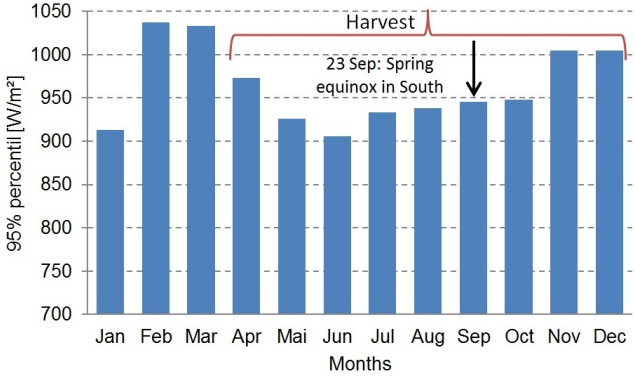

Source: data obtained from Meteonorm® 7.0: Campo Grande - MS.

Figure 52: Wind velocity monthly 95 % percentiles.

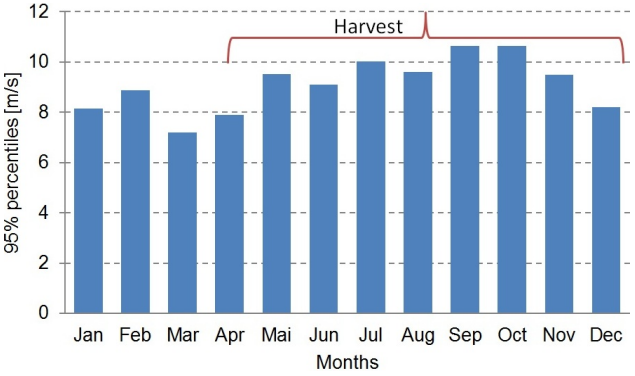

Source: data obtained from Meteonorm® 7.0: Campo Grande - MS.

C.2 COOLING TOWER PARAMETERS

Currently the cogeneration plants in the sugarcane sector are designed to operate also during off-season if biomass is available. Bagasse can be purchased and additional electricity exported to the grid. This is the case of base case plant described in Chapter 6 defined in cooperation with equipment suppliers.

In cogeneration plants with layout similar to the presented in this work (CEST operated in parallel with a BPST) the cooling tower heat load is increased considerably during off-season due to the additional mass flow rate

of exhaust steam. In this regard, this component might de designed in order proper operation is obtained during this period.

In Figure 54 the 95 % percentiles of dry-bulb and wet-bulb temperatures (DB and WB, respectively) for months of December to March are presented. Off-season period comprises of the hottest months of the year. Thus, the average of 95 % percentiles of both DB and WB were equal to 32.7 and 25.6 ^{o}C, respectively, and they were considered in cooling tower design.

Figure 53: Ambient temperature (DB) 5 to 95 % percentiles.

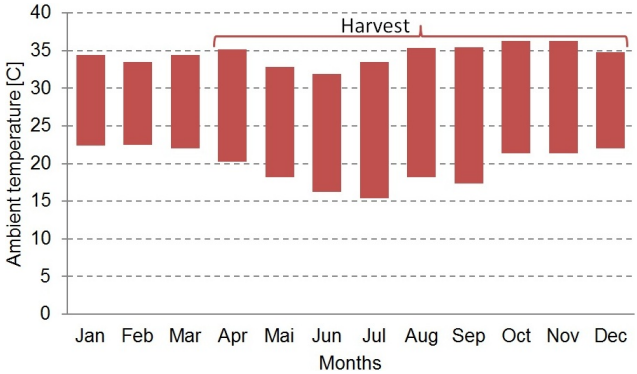

Source: data obtained from Meteonorm® 7.0: Campo Grande - MS.

Figure 54: DB and WB monthly 95 % percentiles for off-season months.

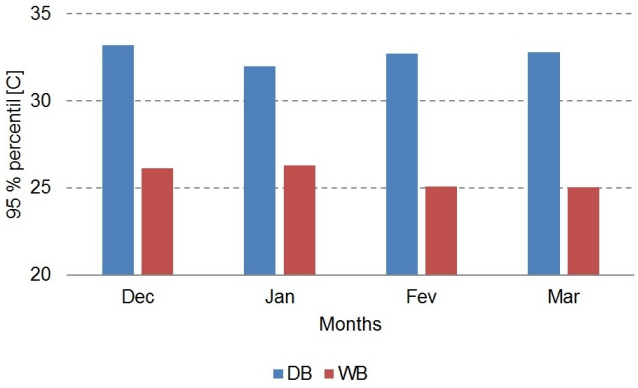

Source: data obtained from Meteonorm® 7.0: Campo Grande - MS.

APPENDIX D – SOLAR SATURATED STEAM GENERATION: AN ALTERNATIVE DESIGN

D.1 DESIGN POINT

As exposed in Section 7.3 of Chapter 7, one concern about the solar saturated steam generation layout was initially related to the reduction of economizer feedwater mass flow and the possibility of water evaporation. This would lead to hot spots in bundle of tubes and failure of heat exchanger. Thus, an alternative concept in which feedwater was diverted to the solar field after it was pre-heated in economizer was proposed and results are summarized in this chapter. Part load operation of one bagasse steam generator is presented in Figure 55 for harvest peak summer design point condition. Results for both steam generators are the same - simulation was performed for one system and replicated to the other.

Figure 55: Solar-aided (after ECO integration) bagasse steam generator simulation results at design point operation.

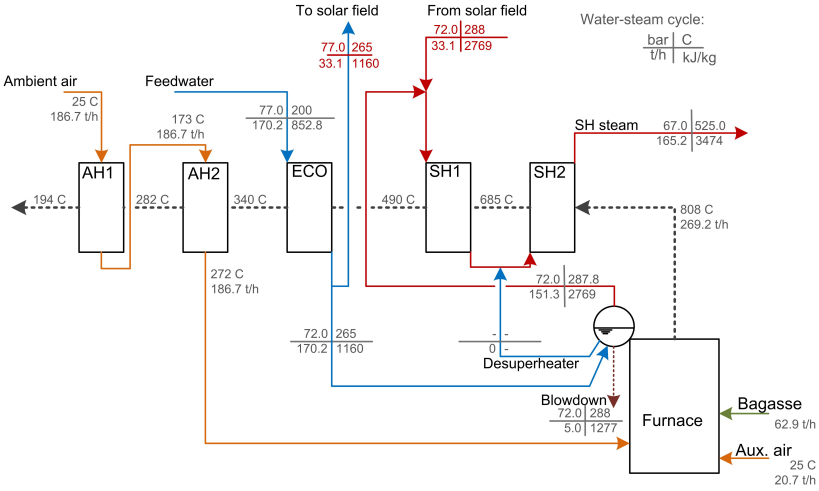

As it can be seen, 33.1 t/h of feedwater at 265 ^{o}C was diverted to the oil-water heat exchangers in order saturated steam (x=1) to be generated. In comparison with diverting feedwater before economizer, additional 18 %

steam mass flow rate was generated for the same limiting design condition in which attemperation was turned zero. Additional steam was generated as water was diverted to solar field with higher temperature. The saturated steam was introduced back in bagasse steam generators to be superheated to the final temperature of 525 ^{o}C. The water tube boiler was operated at reduced load, while economizer and superheaters were operated close to nominal full load. It was proposed the installation of 54,636 m^2 aperture area in a land area of 23 ha (Solar Multiple equal one, SM=1.00). The layout of solar field consisted of 232 LS-2 assemblies disposed in 29 loops.

The solar field simulation results based on harvest design point and the layout of oil-water heat exchanger (boiler) are presented in Figure 56. Feedwater from both bagasse steam generators at 265 ^{o}C was introduced in evaporator and saturated steam at 72 bar was generated. The thermal oil was heated in solar field until 370 ^{o}C and cooled to 298 ^{o}C in boiler. See that the average temperature of HTF was higher here in comparison with alternative design in which an economizer was also implemented in order to pre-heat feedwater diverted from cogeneration cycle.

Figure 56: Solar field (after ECO integration) simulation results at design point operation.

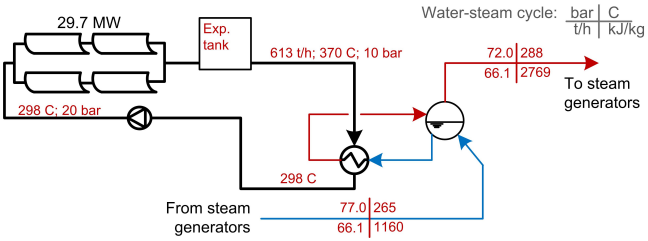

The results related to the solar field performance at design point are presented in Table 24. The number of solar collector assemblies per loop was configured to provide oil mass flow rate in loops close to 25 t/h (BURKHOLDER; KUTSCHER, 2009). The solar field delivered heat was 29.7 MW with 57.0 % thermal efficiency. It was 0.7 % lower in comparison with alternative design implemented for saturated steam generation due to higher HTF average temperature. The electric power consumption was 0.4 MW as required by pumping 613 t/h of thermal oil across solar field. As temperature difference across solar field was reduced it was necessary to increase HTF mass flow rate in order to absorb solar irradiance. This leaded to the augment of parasitic consumption. The bagasse consumption rate was reduced to 125.8 t/h (-11.7 %), keeping the same net electric power exportation of base case.

Table 24: Solar field (after ECO integration) results at design point operation.

Parameter	Unit	Value (SM=1.0)
Solar field aperture area, A_{sf}	m^2	54,636
Land area, A_{land}	ha	23
Solar field delivered heat, $\dot{Q}_{av,ref}$	MW	29.7
Solar field thermal efficiency, $\eta_{sf,ref}$	%	57.0
Oil pump parasitic consumption, $\dot{W}_{p,ref}$	MW	0.4
Oil temperature rise in loops	^{o}C/m	0.2
Oil mass flow in loops, $\dot{m}_{htf,ref}/N_{loop}$	t/h	21.2
Burned bagasse, $\dot{m}_b$	t/h	125.8 (-11.7 %)

D.2 ANNUAL ANALYSIS

The results related to the annual simulation of alternative design of solar saturated steam generation layout are presented in Table 25. The economized amount of bagasse was 11,036 t, what turned possible to generate 6,185 MWh of electricity during off-season (additional 2.7 % electricity exportation when compared to base case). Annual solar-to-electricity conversion efficiency of hybrid system was equal to 7.5 %, providing a solar LCOE of 587 U$/MWh.

Table 25: Results related to solar aided power plant (after ECO integration).

Parameter	Unit	Value (SM=1.0)
Fuel economy, EB	t	11,036
Additional electricity, AE	MWh	6,185
Solar field efficiency, η_{sf}	%	23.7
Solar-to-electricity efficiency, η_{se}	%	7.5
Capital costs, CC	10^3U$	34,229.3
Annual costs	10^3U$	424.3
Solar LCOE	U$/MWh	587.0

This alternative design of solar saturated steam generation provided slightly lower solar-to-electricity conversion efficiency due to higher solar field operating temperature. Nevertheless it was proposed as one option to prevent evaporation in economizer of bagasse unities.

APPENDIX E – SUMMARY OF INOPA PROJECT RESULTS

Distinct integration layouts of base case cogeneration cycle (Chapter 6) were simulated to identify the technical and economic feasibility of hybridization with CSP. The layouts studied are presented in Figure 14 of Chapter 3. Simulations performed are summarized in Table 26. The city of Campo Grande - MS was considered.

Table 26: Number of simulations performed for each layout.

Layouts	Technology (solar field)	Simulated SM	Number of simulations
Layout 1	Parabolic Trough (PT)	0.9 - 1.4	6
	Linear Fresnel (LF)	0.8 - 1.4	7
Layout 2	Parabolic Trough (PT)	0.9 - 1.3	5
	Linear Fresnel (LF)	0.8 - 1.4	7
Layout 3	Central Tower (CT)	0.8 - 4.0	10

SM: Solar Multiple.
Source: iNOPA project Cogeneration power plants (project ID: 57072739).

The additional electricity produced for all integrations are presented in Figure 57. In layouts 1 and 2 PT provided a slightly higher solar electricity output compared with LF. This was related to the higher solar field efficiency of PT caused mainly by the smaller incidence angles in the beginning and in the end of the days when compared with LF. Layout 2 provided higher electricity output when compared with layout 1 mainly due to the higher thermal load required to reduce evaporator thermal load of steam generators. Finally, it is clear that layout 3 provided a significantly higher solar electricity output when compared with other cases. This was not only due to the higher thermal load associated with the reduction of steam generators load to 65 % in peak DNI hours, but also due to the possibility of solar-only operation.

The duration curves related to bagasse steam generators and solar field energy outputs for base case and hybrid layouts 2 and 3 are exposed in Figure 58 to clarify the advantage of solar-only operation. In layout 2 the solar energy was exclusively used to manage part of bagasse from harvest to the off-season period - the same operation strategy was adopted for PT and LF technologies as well as in layout 1. In layout 3, in the other hand, the economized bagasse during harvest was preferentially used at night and solar-only operation was possible during sunny hours. The capacity factor of solar field was maximized by its operation regardless of the availability bagasse.

Another aspect was the required mirrors aperture area and total land area for solar field (see Figure 59). For layouts 1 and 2, the aperture area re-

Figure 57: Additional solar equivalent electricity generated.

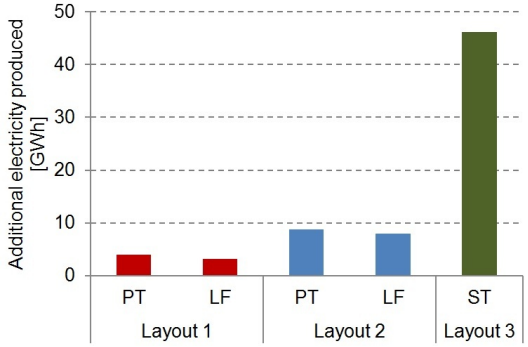

Source: iNOPA project Cogeneration power plants (project ID: 57072739).

Figure 58: Thermal energy transferred to water-steam cycle related to bagasse and solar energy inputs for base case and hybrid layouts 2 and 3 for comparison.

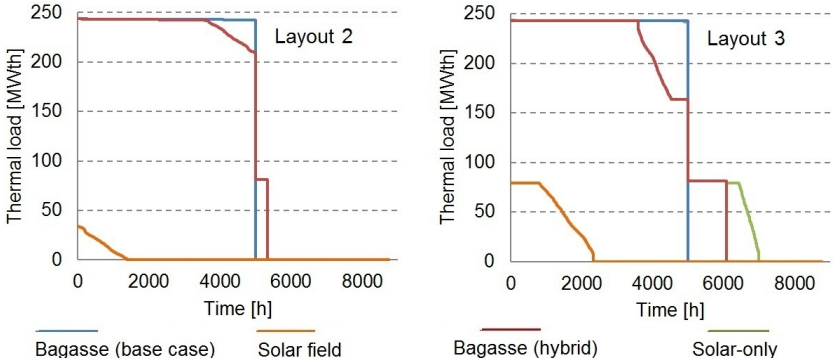

Source: iNOPA project Cogeneration power plants (project ID: 57072739).

quired by LF was higher when compared with PT due to the lower efficiency of LF when compared with PT. Regarding land area, LF showed a significant advantage in comparison with PT, requiring -54 % and -49 % land respectively for layouts 1 and 2. The compactness of LF might be of great importance to enable the implementation of CSP in areas where there is crop plantation. Finally, CT aperture and land areas were higher in comparison other evaluated scenarios due to the higher solar thermal load required by layout 3.

Regarding economic analysis, the capital and O&M costs are presented in Figure 60-a, while in Figure 60-b the LCOE results are showed. The adopted assumptions for equipment and O&M costs were based on consulta-

Figure 59: Thermal energy transferred to water-steam cycle related to bagasse and solar energy inputs for base case and hybrid layouts 2 and 3 for comparison.

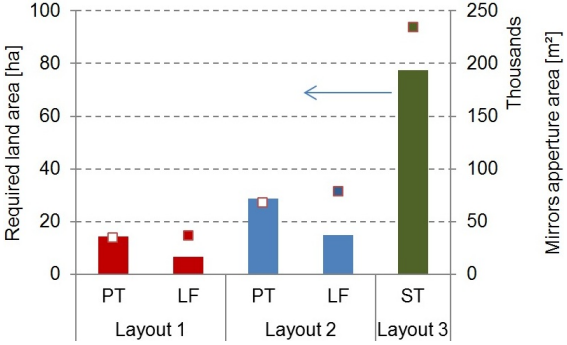

Source: iNOPA project Cogeneration power plants (project ID: 57072739).

tions with equipment suppliers and literature survey. In both layouts 1 and 2 the capital and O&M costs were lower for LF in comparison with PT technology (-14 % and -11 %, respectively, for capital cost). Observing LCOE, nevertheless, LF presented similar or even higher electricity costs in comparison with PT due to its lower efficiency. LCOE was significantly reduced in layout 3, reaching 220 U$/MWh. As exposed before, solar-only operation maximized capacity factor of solar field and this is directly linked to an improved economic performance. It is important to notice that layout 3 could also be possible with PT or LF depending on main steam parameters of plant.

Figure 60: a) Investment and O&M costs of solar hybridization; b) LCOE of additional solar equivalent electricity.

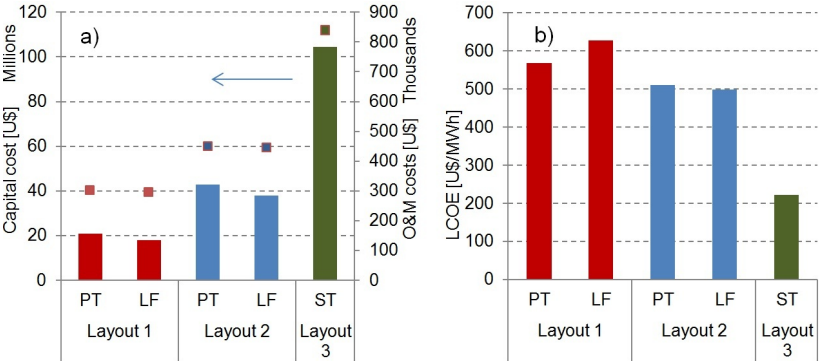

Source: iNOPA project Cogeneration power plants (project ID: 57072739).

ANNEX A – HEAT TRANSFER FLUID PROPERTIES

Heat transfer fluid considered in this work was thermal oil Therminol VP-1 by Solutia® (SOLUTIA, 2014). Maximum operation temperature is limited to 400 ^{o}C, while solidification temperature is 12 ^{o}C. The thermophysical and transport properties of Therminol VP-1 (liquid phase) are summarized below:

$$\nu = 10^{-6} \cdot exp((544.15/(T + 114.43)) - 2.60) \tag{A.1}$$

$$\mu = -0.91T + 0.78 \cdot 10^{-3}T^2 - 2.37 \cdot 10^{-6}T^3 + 1083 \tag{A.2}$$

$$T = -1.58 \cdot 10^{-10}h^2 + 0.61 \cdot 10^{-4}h + 13.37 \tag{A.3}$$

$$\rho = -0.91 \cdot T + 0.78 \cdot 10^{-3}T^2 - 2.37 \cdot 10^{-6}T^3 + 1083 \tag{A.4}$$

$$\begin{aligned} cp = {} & 0.24 \cdot 10^{-2}T + 5.96 \cdot 10^{-6} \cdot T^2 - 2.99 \cdot 10^{-8} \cdot T^3 + \\ & + 4.42 \cdot 10^{-11} \cdot T^4 + 1.50 \end{aligned} \tag{A.5}$$

$$h = -18.34 + 1.50 \cdot T + 0.12 \cdot 10^{-2} \cdot T^2 \tag{A.6}$$

$$\begin{aligned} k = {} & -8.19 \cdot 10^{-5} \cdot T - 1.92 \cdot 10^{-7} \cdot T^2 + \\ & + 2.50 \cdot 10^{-11} \cdot T^3 - 7.30 \cdot 10^{-15} \cdot T^4 + 0.14 \end{aligned} \tag{A.7}$$

where ν [m^2/s] is the kinematic viscosity; μ [Pa.s] is the dynamic viscosity; T [^{o}C] is the HTF temperature; ρ [kg/m^3] is the specific mass; cp [kJ/kg.K] is the specific heat at constant pressure; h [kJ/kg] the enthalpy and k [W/m.K] the conductivity.